ABSTRACT

Title of dissertation: PROCESSING AND STRUCTURAL CHARACTERIZATION TOWARD ALL-CELLULOSE NANOCOMPOSITES

Doug Henderson, Doctor of Philosophy, 2021

Dissertation directed by: Professor Robert Briber
Materials Science and Engineering

Cellulose is the most abundant biopolymer on the planet and is used in a variety of industry sectors including paper, coatings, medicine, and food. A deep understanding of cellulose is important for its development as an alternative polymer to those based on petroleum.

This work focuses on two cellulose systems. The first of these, cellulose nanofibers, are the basic structural elements of naturally-occurring cellulosic materials; they exhibit excellent mechanical characteristics due to high crystallinity and a dense network of hydrogen bonding. These fibers can be separated from bulk cellulose via a TEMPO oxidation reaction followed by mechanical homogenization into a suspension in water. In this work, the production of these fibers is investigated by monitoring the change in structure of cellulose as a function of TEMPO reaction time and mechanical homogenization using small angle neutron scattering, atomic force microscopy, and optical microscopy.

The second cellulose system is a molecular solution of cellulose formed using a

binary solvent mixture consisting of ionic liquid and an aprotic solvent. Cellulose is difficult dissolve due to a dense hydrogen bonding network, and ionic liquids have been shown to be an effective alternative to more hazardous and energy-intensive dissolution methods for cellulose currently used in industry. The phase behavior of these solutions has been investigated using small angle neutron scattering as a function of temperature. The process of regenerating cellulose from these solutions is also investigated, as dense gels of cellulose and ionic liquid were produced with a unique multiscale ordered structure.

The ultimate goal of this work is to combine cellulose nanofibers and molecular cellulose solutions in order to create all-cellulose nanocomposite films. These films are characterized using tensile testing, atomic force microscopy, and water uptake measurements in order to understand the interaction between cellulose nanofibers and molecular cellulose solutions, water resistance and tunability of mechanical properties.

PROCESSING AND STRUCTURAL CHARACTERIZATION TOWARD ALL-CELLULOSE NANOCOMPOSITES

by

Douglas Arthur Henderson

Dissertation submitted to the Faculty of the Graduate School of the
University of Maryland, College Park in partial fulfillment
of the requirements for the degree of
Doctor of Philosophy
2021

Advisory Committee:
Professor Robert Briber: *Advisor, Chair*
Professor Teng Li: *Dean's Representative*
Professor Howard Wang
Professor Liangbing Hu
Professor Isabel K. Lloyd

Dedication

This work is dedicated to my fiance, Mackenzie. Thank you for being my rock, and for being supportive throughout my graduate school career. I could not have done this without you.

Acknowledgments

I would first like to acknowledge the support of my advisor Dr. Robert Briber. The last few years in particular have required lots of one on one meetings to complete my research and finalize my thesis, and I will always appreciate his mentorship and time dedicated to my graduate tenure. Dr. Briber has a clear love for teaching and educating, and it showed in my time working closely with him as much as it has in his many roles serving the Clark School of Engineering.

I would also like to recognize the time, dedication, and patience from Dr. Howard Wang during his advising of my work. Dr. Wang has exceptional integrity and a vast fundamental understanding of materials science. He taught me to appreciate and believe in collaborative and incremental scientific progress, what it takes to be a good researcher, and how to hold myself to a higher standard. I will always be thankful for his guidance and his effort throughout my time working with him.

I would like to thank Dr. Xin Zhang, for his many years of being my mentor, travel companion, and lab-mate. I learned most of my technical and hands-on laboratory skills from watching and learning from Dr. Zhang over the years. We attended many conferences, workshops, and other laboratories together and he was always a joy to travel with. He is exceptionally smart and kind, and I will always be appreciative of his time and his sage advice during my graduate tenure.

I would like to thank Dr. Yimin Mao for his support during my work. He is a talented instrument scientist and a wonderfully kind and outgoing person, and

offered constant advice on anything from interpreting complex scattering data, to advice on writing, presenting, and a career. I would also like to thank Dr. Wonseok Hwang for his expertise in both small angle X-ray scattering and rheology. He put in lots of time to help me collect critical data to finish a particularly difficult project.

I would like to recognize the advising of Dr. Liangbing Hu during the early portion of my graduate work, who initially sparked my interest in cellulose research, nanofibers, and sustainable materials through the novel and engaging project ideas in his group. I also would like to acknowledge the assistance I received from other colleagues at the NIST Center for Neutron Research and for UMD affiliated labs like the Advanced Imaging Laboratory (AIMLab), X-ray Crystallography Center, and in particular Dr. Karen Gaskell at the Surface Analysis Center who assisted me countless times with atomic force microscopy. I'd also like to thank Dr. Isabel Lloyd and Dr. Peter Kofinas for their time and advice during large group meetings.

Finally, I'd like to thank my parents, Walter and Carla; my stepmom, Sandy; my brother, Brian; my friends; my fiance, Mackenzie, and her parents Mark and Jackie. All have been incredibly supportive throughout my graduate tenure, and helped me get to where I am.

Table of Contents

List of Tables

List of Figures

List of Abbreviations and Symbols

$-COOH$ protonated carboxylate group.

$-COONa$ sodium carboxylate group.

$-ONO_2$ nitrate.

D_2O deuterium oxide.

$EG_{54}DMAm_{46}$ poly[(ethylene glycol methyl ether methacrylate)-co-N,N-dimethylacrylamide].

H_2SO_4 sulfuric acid.

$LiOH$ lithium hydroxide.

$NaOH$ sodium hydroxide.

T_g glass transition temperature.

AFM atomic force microscopy.

AGU anhydroglucose unit.

AMIMCl 1-allyl-3-methylimidazolium chloride.

ATR attenuated total reflectance.

AUC alkali-urea dissolved cellulose.

CESA cellulose synthase proteins.

CHRNS center for high resolution neutron scattering.

CNC cellulose nanocrystals.

CNF cellulose nanofibers.

DMA dynamic mechanical analyzer.

DMAc dimethylacetamide.

DMAm poly(N,N-dimethylacrylamide).

DMF dimethylformamide.

DMSO dimethylsulfoxide.

DP degree of polymerization.

EMIMAc 1-ethyl-3-methylimidazolium acetate.

EMIMCl 1-ethyl-3-methylimidazolium chloride.

FTIR fourier transform infrared spectroscopy.

FWHM full-width at half maximum.

HEC hydroxyethyl cellulose.

IL ionic liquid.

MC molecular cellulose.

MCS molecular cellulose solution.

MFC microfibrillated cellulose.

NIST National Institute for Standards and Technology.

NMMO N-methylmorpholine N-oxide.

NMP N-methyl-2-pyrrolidone.

NMR nuclear magnetic resonance.

OLED organic light emitting diode.

PAA poly(acrylic acid).

PAM poly(acrylamide).

PET polyethylene terephthalate.

PVA polyvinyl acetate.

SANS small angle neutron scattering.

SAXS small angle X-ray scattering.

SEM scanning electron microscopy.

SLD scattering length density.

TEMPO (2,2,6,6-Tetramethylpiperidin-1-yl)oxyl.

TOCN TEMPO-oxidized cellulose nanofibers.

WAXS wide angle X-ray scattering.

XRD X-ray diffraction.

Chapter 1: Introduction

1.1 Cellulose

Cellulose is the most abundant biopolymer in the world and has served as an important material throughout human history. Cellulose first found use by humanity in the form of wood as an energy source, structural material, and source of clothing. More recently it has found usage as a polymeric material through regeneration and chemical modification, with applications as films, coatings, membranes, pharmaceuticals, textiles, and as a food additive. Currently, industry is heavily reliant on polymer materials produced from petroleum, which can have a negative impact on the environment due to extraction methods, subsequent refining and processing, and eventual disposal of the polymer. Understanding the properties, processing, and identifying additional applications of sustainable materials like cellulose is essential for providing cost-effective, environmentally friendly alternatives to petroleum-derived polymers in use today.

1.1.1 Polymer structure

The molecular structure of cellulose consists of two mirrored monomers called anhydroglucose unit (AGU), the repeat unit of cellulose. Each AGU has the chemical formula of $C_6H_{10}O_5$. The dimer unit containing both AGU is called cellobiose, as shown in Figure 1.1, in which each bonded AGU is rotated 180° [1]. The two mirrored AGU are bonded via a β-1,4-glycosidic bond. Each AGU contains three hydroxyl groups, two secondary hydroxyl groups on C2 and C3, and a primary hydroxyl group on C6. The degree of polymerization (DP) is defined by the number of AGU in a cellulose chain and can vary depending on the cellulose source. Wood will typically have a DP of between 9000-10000, but cellulose after pulping treatments have a DP of between 300 and 1700. Regenerated cellulose will have an even lower DP of 250-500 [2, 3].

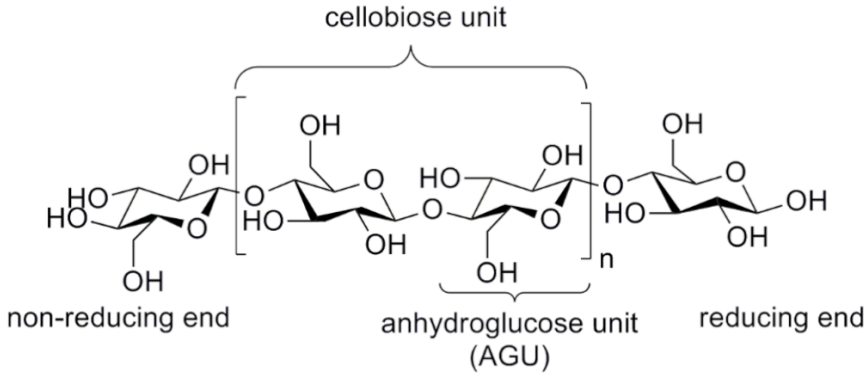

Figure 1.1: Schematic showing the monomer and dimer structure of cellulose. The dimer, cellobiose, is composed of two mirrored-facing monomers, referred to as AGU [1]. © 2015

Cellulose polymer chains are synthesized within the plant cell by cellulose synthase proteins (CESA) [4, 5]. CESA proteins are arranged into parallel arrays

called rosettes, forming a terminal complex with six-fold symmetry. The rosette contains 6 CESA protein monomers. [6] The CESA subunits are arranged into a hexagonal rosette shape resulting in roughly 36 total cellulose chains forming a single nanofiber in which chains are held together by hydrogen bonding and van der Waals forces [7]. A schematic representation of the CESA protein complex arranged in the rosette shape synthesizing cellulose is displayed in Figure 1.2 [6, 8].

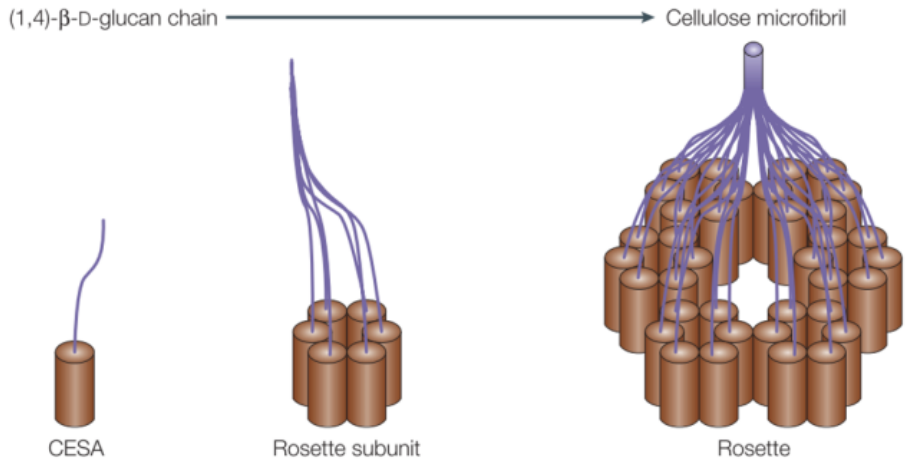

Figure 1.2: Schematic illustrating the synthesizing of cellulose in the terminal complex. CESA are arranged into hexagonal rosette units and subunits to synthesize cellulose chains that associate to form an elementary cellulose nanofiber (labelled microfibril in image) [8]. ©2006

1.1.2 Cellulose hierarchical structure

The cellulose chains make up the structural component of the plant cell wall. Hierarchical buildup and layering of cellulose nanofibers, interspersed with lignin and hemicellulose, complex polysaccharides that adds structural robustness to the stiff cellulose network within the cell wall. These complexes form layers in the plant cell wall then ultimately form the structure found in wood as shown in Figure 1.3 [9].

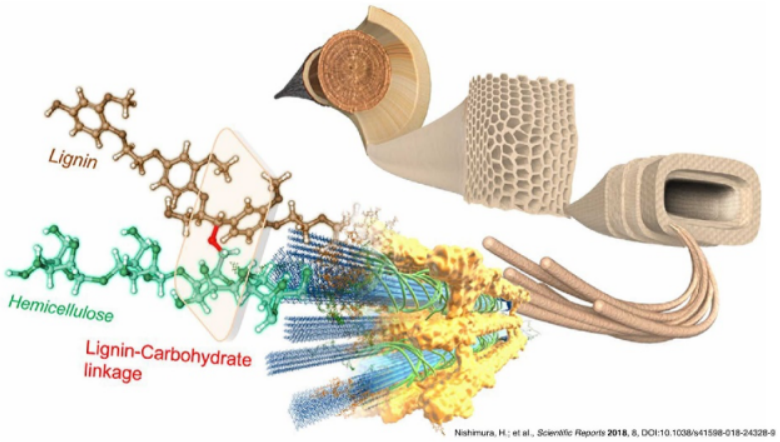

Figure 1.3: Overall schematic of the different structures and materials present in wood and plant cell walls. Cellulose is hierarchically structured to make up the structure of wood, with lignin and hemicellulose interspersed throughout to reinforce the cellulose network [9]. © 2008

The individual elementary cellulose nanofiber is synthesized in parallel with other nanofibers that ultimately entangle, and form bundles held together through hydrogen and van der Waals bonding. A schematic of the nanoscale organization of cellulose nanofibers is shown in Figure 1.4a. An individual nanofiber is made up of crystalline regions with periodic amorphous regions. Within these bundles of nanofibers, the chains in the crystalline regions are aligned while entanglement occurs in the amorphous regions between crystallites. Individual nanofibers typically have diameters around 2-4 nm while the length can be on the order of microns. Bundles of nanofibers can range between 10-25 nm in diameter [10, 11].

These bundles are then grouped together and aligned within various layers of the cell wall, ultimately forming a cellulose macrofiber which are typically 20-40 μm in diameter. The layering of different arrangements of cellulose within the cell wall is shown in Figure 1.4b [11]. The arrangement of cellulose nanofibers within each layer of the cell wall can vary based on a number of variables all depending on the type of

plant or role of the cell within the plant. The average nanofiber length, number of nanofibers per bundle, overall cellulose composition, angle of nanofiber alignment, number of layers, etc. can vary depending on the function of the plant cell [6, 12, 13].

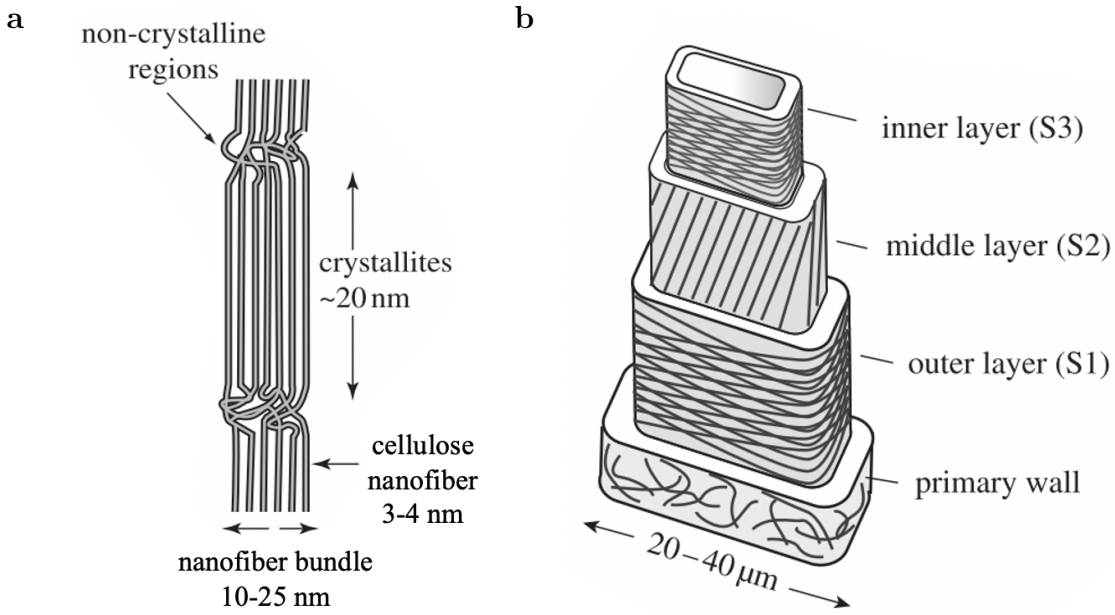

Figure 1.4: a) Schematic showing the structure and arrangement of cellulose nanofibers within bundles. b) Arrangement of nanofiber bundles within layers of the plant cell wall to form a cellulose macrofiber [11]. © 2007

1.1.3 Cellulose Crystal Structures

1.1.3.1 Cellulose I

Cellulose I is the only naturally occurring crystalline form of cellulose, manifesting in the crystalline regions of cellulose nanofibers. When cellulose is synthesized from the terminal CESA complex, the polymer chains are extruded in parallel to each other, which align the hydroxyl groups on the C6 of the AGU in the same

direction. This Cellulose I structure also has two different sub-allomorphic structures, referred to as cellulose Iα and Iβ. Depending on the cellulose source, different ratios of allomorphs Iα and Iβ will be present. Iα and Iβ can be found together within a given cellulose sample, and even along the same nanofiber. Certain algae and bacterial cellulose are shown to be more rich in Iα, while plant cellulose such as wood, cotton, and ramie fibers contain mostly Iβ [14, 15].

Iα is a triclinic unit cell containing one cellulose chain. The lattice parameters of Iα are: a = 6.7 Å, b = 6.0 Å, c = 10.4 Å, $\alpha = 118.1°$, $\beta = 114.8$, $\gamma = 80.4°$ [15]. Iβ is a monoclinic unit cell containing two cellulose chains. The lattice parameters of Iβ are: a = 7.8 Å, b = 8.4 Å, c = 10.4 Å, $\alpha = \beta = 90°$, $\gamma = 96.5°$ [15]. One notable difference between Iα and Iβ is in the offset of the aligned polymer chains, and is illustrated in Figure 1.5 when observing the (011) phase of the crystal structures. In the Iα phase the chains are offset about $\frac{1}{4}$ the length of a cellulose repeat unit in the direction of hydrogen bonding, while in Iβ the offset is still 25% of the cellulose chain length but alternates between chains. This causes every other chain to be lined up in a staggered pattern [10, 16].

A more detailed view of the cellulose I lattice structures is shown in Figure 1.6, which is viewed along the direction of the cellulose chain, or the $\overrightarrow{c}$ direction. Figure 1.6a shows the lattice structure of phase Iα. The (110) plane is the hydrogen bonding plane, while the (100) and (010) planes contain van der Waals and hydrophobic interactions. The $\overrightarrow{a}$ and $\overrightarrow{b}$ directions illustrate the distance between sheets of cellulose chains [10,15]. Figure 1.6b shows the lattice structure of phase Iβ. Hydrogen bonding between cellulose chains occurs within the (010) plane, while van der Waals

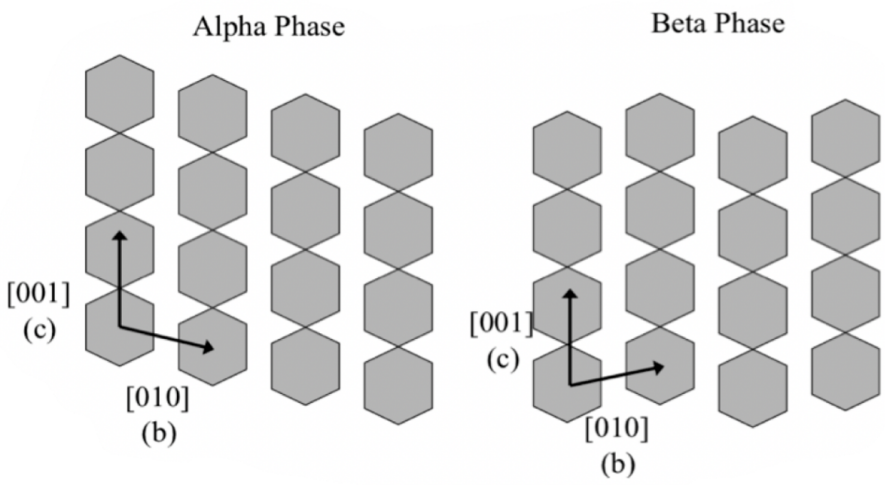

Figure 1.5: Schematic showing how the difference in the cellulose polymer offset between Iα (left) and Iβ (right) effects the resulting plane directions and lattice structures. The view for both phases is in the (011) phase [16]. © 2005

and hydrophobic interactions occur within the (100), (110), and (1$\bar{1}$0) planes. The $\overrightarrow{b}$ direction is the direction of hydrogen bonding between chains, and the $\overrightarrow{a}$ direction is the direction of cellulose sheet stacking [10, 15].

1.1.3.2 Cellulose II

In native cellulose the chains are synthesized in a parallel conformation, resulting in the two possible cellulose I crystal structures. Cellulose can be processed, dissolved, and regenerated into a different crystal structure [17], in which the chains are arranged in an antiparallel conformation. This means that the C6 hydroxyl groups are in opposite locations between adjacent cellulose chains. This structure, though not naturally occurring, is more thermodynamically stable, so cellulose dissolution and reconstitution or strong alkali treatment can result in the cellulose II structure [18]. Part of this stability is due to the antiparallel conformation, which enables additional

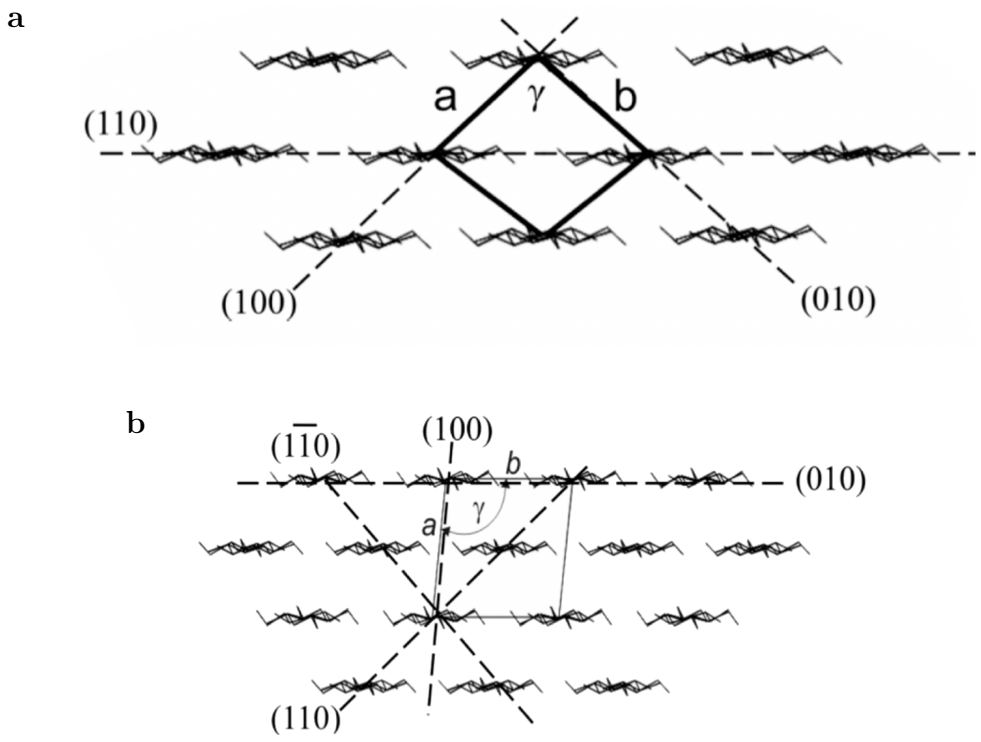

Figure 1.6: Lattice structure of native cellulose phase a) Iα and b) Iβ. The view in both schematics is perpendicular to the cellulose chain direction,
c [15]. © 2003

hydrogen bonding in the (110) plane [19, 20]. The cellulose II unit cell is monoclinic containing two cellulose chains per cell, with lattice parameters: a = 8.0 Å, b = 9.0 Å, c = 10.4 Å, $\alpha = \beta = 90°$, and $\gamma = 117.1°$ [10, 21]. The overall lattice structure of cellulose II is shown in Figure 1.7a. This regenerated form of cellulose is found in fibers such as rayon, lyocell, or viscose [22].

1.1.3.3 Cellulose III

The cellulose III crystal structure can be obtained from either native cellulose I or cellulose II by treating with an ammonia or amine solution. This structure

is softer and more plastic than cellulose I or II and has also found applications in the textile industry [23, 24]. Cellulose III has similar intersheet hydrogen bonding interactions to cellulose II, however its chains are still aligned in parallel as found in native cellulose I. Cellulose III has a monoclinic unit cell containing one cellulose chain, with lattice parameters: a = 4.5 Å, b = 7.9 Å, c = 10.4 Å, $\alpha = \beta = 90°$, and $\gamma = 105.1°$ [10, 23, 24]. A schematic detailing the lattice structure of cellulose III is shown in Figure 1.7b.

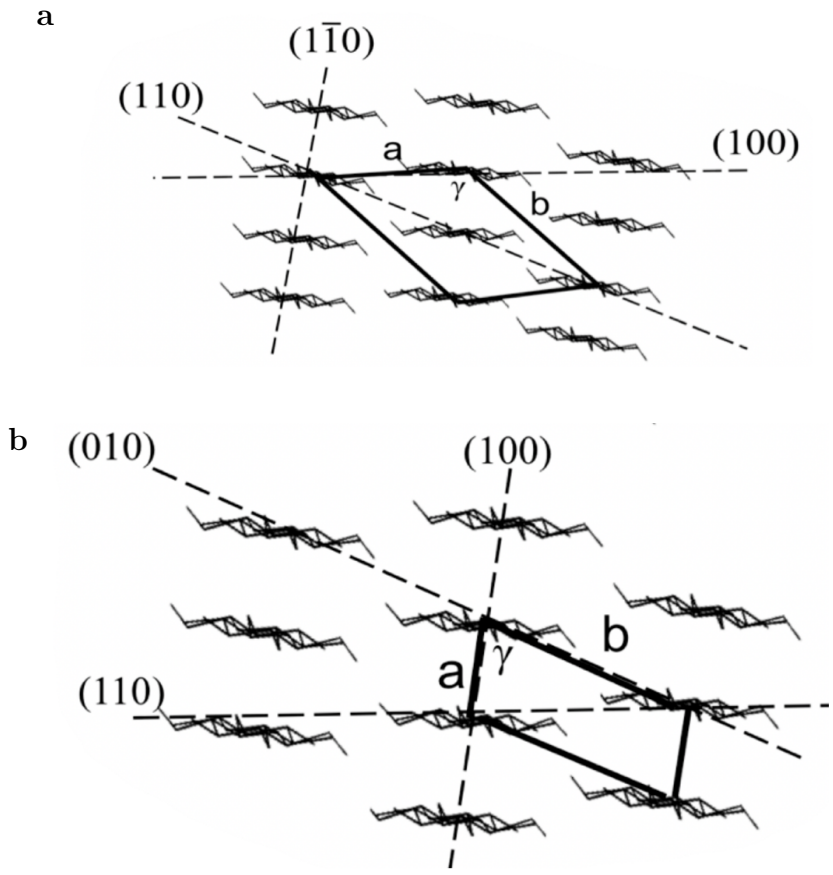

Figure 1.7: Lattice structures of cellulose a) II and b) III [22]. © 2011

1.1.3.4 Cellulose IV

Cellulose IV is a crystal structure of cellulose that can only be obtained once native cellulose I has been converted to the cellulose II or III structure [10,25] through treatment with glycerol [19]. Cellulose IV has a tetragonal unit cell containing two cellulose polymers per unit cell, with lattice parameters: a =8.0 Å, b = 8.1 Å, c = 10.4 Å, and all angles α, β, and $\gamma = 90°$.

1.1.3.5 Amorphous

When cellulose is highly disordered and does not exhibit any defined crystal structures, it is considered amorphous. Amorphous cellulose exists in native cellulose between the crystallites containing the cellulose I structure. Amorphous cellulose also tends to be less dense, less stiff, and more reactive than crystalline cellulose [26].

1.1.4 Hydrogen Bonding

The hierarchical cellulose structure, from nanofiber bundles in the cell wall to chains forming into crystal structures, is held together by a complex network of hydrogen bonding [12]. Cellulose chains exhibit three different hydrogen bonds, the first being interchain, or between chains, and the second being intrachain, or within a single chain. In native cellulose the intrachain hydrogen bonds occur between O3H – O5 and O2H – O6, and the interchain bond occurs between O6H – O3 [10,15,27]. The hydrogen bonding network is illustrated in Figure 1.8. Interchain hydrogen bonds establish bonds between cellulose chains and adds to the strength and resilience of

the cellulose. It also makes cellulose difficult to dissolve [28]. Intrachain hydrogen bonds help maintain stiffness within individual cellulose chains.

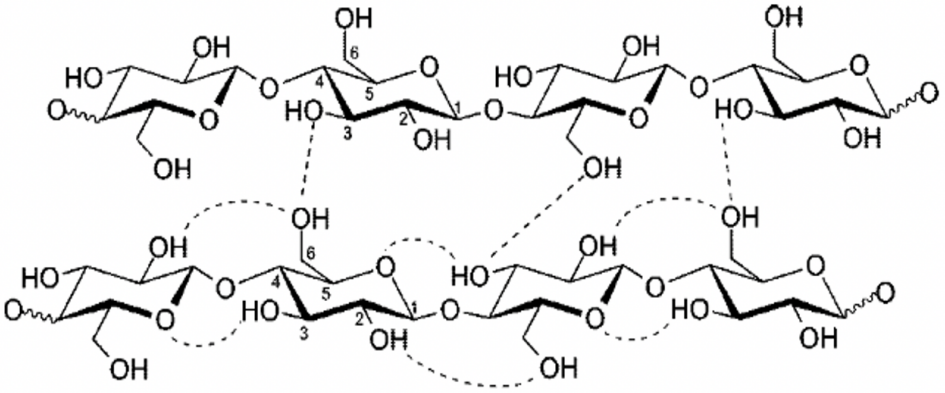

Figure 1.8: Inter- and intrachain hydrogen bonding network present between cellulose chains [28]. © 2009

1.2 Instrumentation

1.2.1 Optical Microscopy

Optical microscopy is a technique useful for observing and quantifying larger scale objects in the micron to millimeter size range. Light can be employed and manipulated in an optical microscopy to enable different techniques that have different applications in characterization. A schematic example of an optical microscope is shown in Figure 1.9. For bright field images, the sample is placed onto a stage in the center of the setup, directly below the objective lens. Light is applied from underneath the sample stage, illuminating the sample for imaging from a camera set above the lens setup.

One additional method of imaging with an optical microscopy employs cross polarizers, the setup for which is also shown in Figure 1.9. Light provided from a

source under the sample passes through a polarizer, after which the light vibrates along only one plane. This light will pass through the sample, interacting with birefringent material which splits the polarized light causing it to vibrate along multiple planes. The light then passes through an additional polarizer oriented at 90 ° to the first, called an analyzer. This eliminates any light oriented along the plane that was allowed to pass through the first polarizer, which eliminates all light that did not interact with birefringent material, generating contrast in particular materials and parts of a sample. Typical birefringent materials include liquid crystals, polymers under deformation, certain crystalline materials, and anisotropically ordered materials.

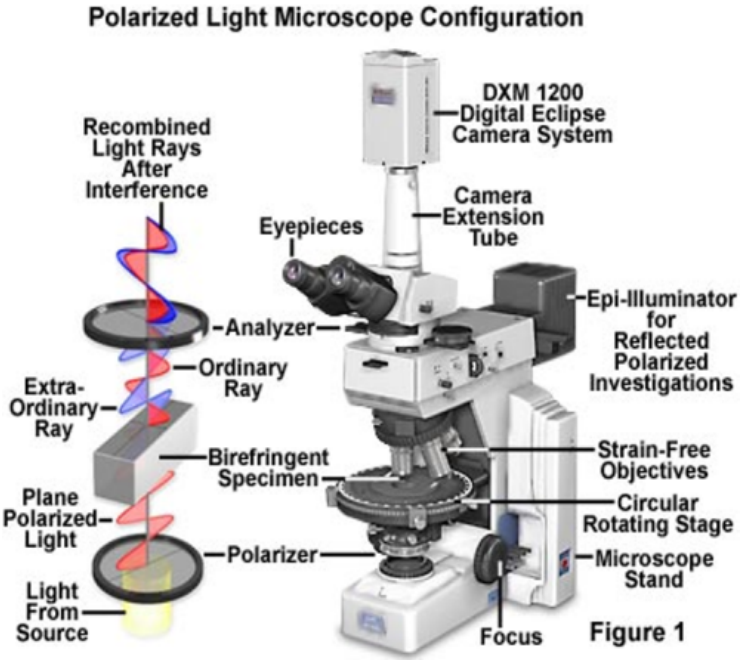

Figure 1.9: Experimental setup for an optical microscope with cross polarization capabilities [29]. © 2015

Cellulose fibers exhibit birefringence due to the higher index of refraction along the cellulose chains versus perpendicular to them. Therefore, alignment of nanofiber

bundles within different layers of the cell wall appear as birefringent, becoming more visible. As a result, when using cross-polarized optical microscopy to observe TEMPO oxidized cellulose, the fibers can be seen with greater contrast, making their changes in morphology, particularly upon swelling and disintegration, more visible. Optical microscopy in this work was conducted using an Olympus Accura Zoom XB70 microscope.

1.2.2 Small angle X-ray and neutron scattering

Small angle scattering is a technique that can investigate the structure of materials by probing variations in density or electron density at the nanometer scale. This is a useful technique for studying cellulose nanomaterials and its phase behavior in solutions. X-rays and neutrons are used for small angle scattering. Some of the basic theory for SAXS and SANS scattering will be described, along with the advantages of each technique. Brief explanations will also be given for methods of data reduction and analysis and understanding scattering data in the context of this work.

1.2.2.1 Basics of elastic scattering

In a scattering experiment, the probe (i.e. neutrons, x-rays, or photons) will interact with the molecules in a sample, resulting in a change in the momentum vector, k, or the energy of the probe. X-rays will interact with electrons while neutrons will interact with atomic nuclei in the sample, which leads to differences

in contrast. This event is illustrated by the schematic in Figure 1.10 [30], and the change in momentum results in a value called the scattering vector as given by the following equation:

$$\left|\vec{k_s} - \vec{k_l}\right| = \vec{Q} = \frac{4\pi}{\lambda} sin(\theta) \tag{1.1}$$

Where λ is the wavelength of the scattering probe. If this change in momentum results in no change in energy, it is referred to as elastic scattering, which is the type of scattering employed in this work. The scattering vector, Q, can yield important structural information for a sample based on Bragg's Law, given in Equation 1.2, for calculating the interplanar spacing, or d-spacing, in a lattice [30].

$$n\lambda = 2dsin(\theta) \tag{1.2}$$

Relating these two equations yields a relation between the scattering vector, Q, and a given distance in a sample [31]:

$$d = \frac{2\pi}{Q} \tag{1.3}$$

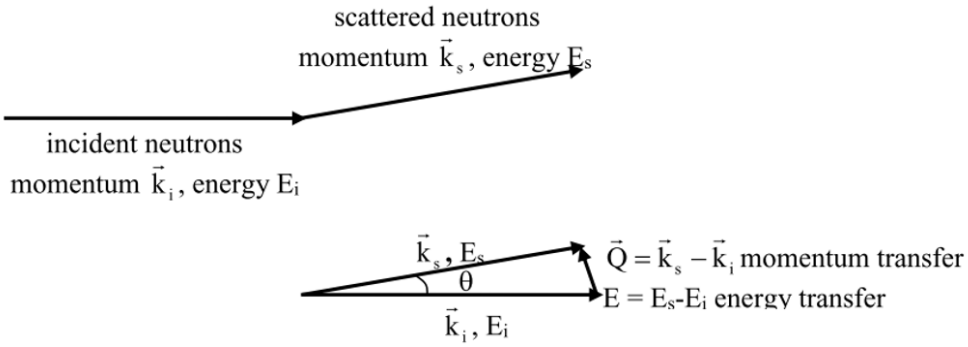

Figure 1.10: Momentum transfer that occurs during a scattering event, relating to the scattering vector, Q [30].

1.2.2.2 Experimental setup

For small angle scattering experiments, X-ray and neutrons are first generated from a variety of sources. For many laboratory X-ray sources, such as the CuKa source from the Xenocs Xeuss instrument employed in this work, are produced from running a high voltage between two electrodes. The elements used in the source electrodes produce x-rays with different ranges of energies, which can affect the range of scattering angles available for measurement. An additional type of X-ray source is called a synchrotron, which is a circular particle accelerator used to accelerate photons to relativistic speeds and high energies. For experiments that require high flux, for example measuring materials that do not scatter strongly, a synchrotron source is useful as a single measurement only takes seconds, versus minutes or hours at a smaller-scale laboratory source. Neutron sources are usually either produced from continuously operating fission reactors, or from spallation sources. Continuous reactors typically generate neutrons based on the fission reaction of U-235, which yields 2-3 neutrons at energies of about 2 MeV. Generated neutrons are directed into beam guides where they are prepared for measurement. In spallation sources, high energy hydrogen ions are produced by a linear accelerator, deposited into a synchrotron and accelerated to incredibly high speeds. These ions then collide with a high atomic number target, producing 10-30 neutrons per ion collision. This design allows for a high flux of neutrons that can be generated in pulses, which allows for time-resolved measurements [30].

There are four basic steps to a small angle scattering experiment, shown

in Figure 1.11: monochromation, collimation, scattering, and detection. During monochromation, the beam is narrowed only to allow neutrons of a certain range of energies. This is typically done with a velocity selector and ensures the wavelength of neutrons or x-rays in the beam are consistent. Collimation removes neutrons or x-rays not parallel with the beam. This can be accomplished by placing an aperture after monochromation and a second aperture before the sample, as is shown in Figure 1.11. Collimation ensures the measurement of the scattering angle is accurate, and the distance between apertures can be adjusted to determine the level of accuracy desired. B. More precise monochromation and collimation will improve the wavelength and Q resolution, but will decrease the flux of the beam. Neutron beams will typically have lower flux than X-ray beams, so depending on the sample and the facility broadening the beam resolution is sometimes needed to complete a measurement in a timely manner. Scattering is performed as the neutron beam interacts with the sample. Scattered neutrons are typically detected by a 2-dimensional area detector, which is placed behind the sample as shown in Figure 1.11. Area detectors are 2D arrays of individual detectors each representing a pixel on a digital image of the area detector. Neutron or X-ray counts are measured over the course of a measurement, and a 2D image of the detector is constructed according to the relative intensities for each pixel. An example of this image is shown in Figure 1.11 [30].

The area detector can be placed at different distances from the sample, resulting in a different measurable range of scattering angle, Q. This raw 2D scattering pattern of the scattered beam can be averaged with respect to Q, resulting in the variation in scattering intensity, I(Q). Measurements will typically be conducted at a variety

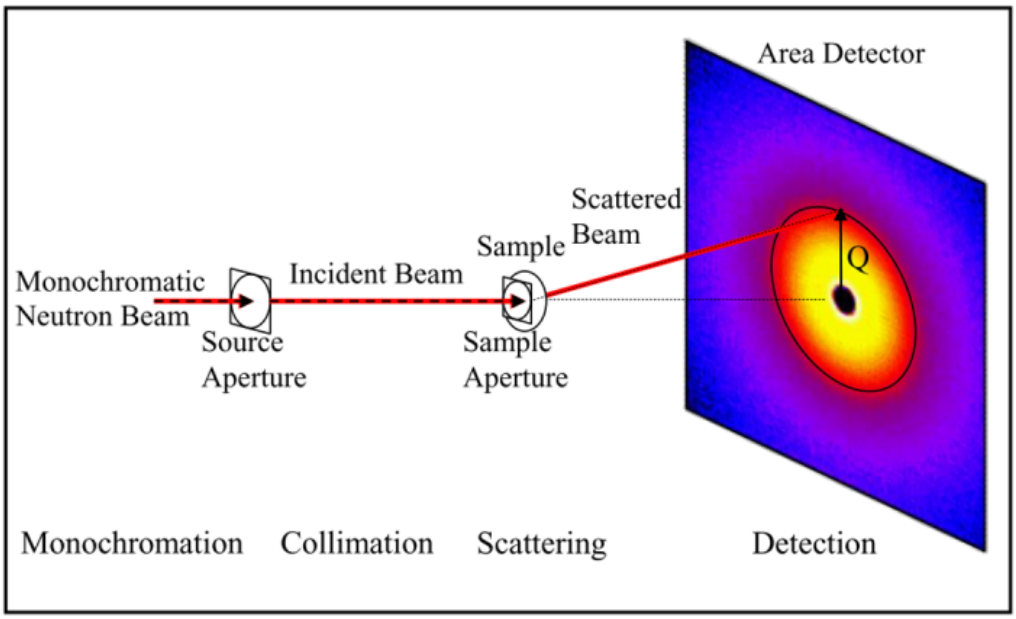

Figure 1.11: Experimental setup for a small angle neutron scattering measurement. An example raw 2D scattering pattern is shown on the area detector [30].

of sample-to-detector distances in order to measure different size scales and a full range of scattering angle. At short distances a high scattering angle (usually up to ~0.5 $Å^{-1}$) and therefore shorter length scales, on the order of nanometers, are measured. At longer distances a low scattering angle (down to ~0.001 $Å^{-1}$) and longer length scales, on the order of hundreds of nanometers, are measured. The pattern can be circularly averaged to create a plot of the scattering intensity, I(Q) as a function of Q. Through data analysis, the relationship between I(Q) and Q can determine important properties or structure of a sample [30].

1.2.2.3 Scattering contrast

The likelihood of interaction between the scattering probe and the component can be described by the scattering cross section, which is a general approximation

of how large an atom appears to the incident beam. Differences in scattering cross sections for elements as a function of atomic number using both neutrons and X-rays is shown in Figure 1.12 [30].

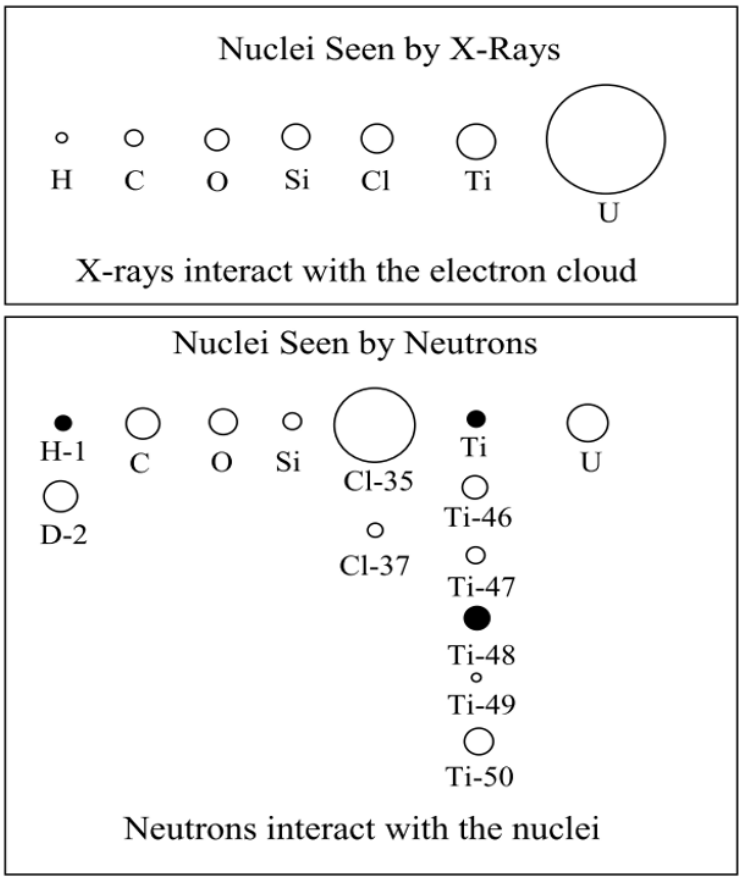

Figure 1.12: Differences in scattering cross sectionof different elements and isotopes between small angle x-ray and neutron scattering [30].

The contrast factor, $\Delta\rho^2$, is the difference between scattering length densities within a given sample. The scattering length varies based on the scattering probe (neutrons or X-rays) and is dependent on the elements present in a sample. For example, X-rays and electrons interact with the electron cloud of an atom, while neutrons interact with the nuclei of an atom. The equation for calculating contrast factor, $\Delta\rho^2$, based on the scattering lengths is Equation 1.4, where b is scattering

length, v is the molecular volume, ρ is scattering length density (SLD), and A and B represent different components of the sample, for example, particles and solvent [30]:

$$\Delta\rho^2 = (\rho_A - \rho_B)^2 = \left(\frac{b_A}{v_A} - \frac{b_B}{v_B}\right)^2 \tag{1.4}$$

In X-ray scattering, the size of an electron cloud generally increases with the number of electrons, or the atomic number of an atom. Thus, metals and other heavy atoms will scatter x-rays more strongly than lighter atoms like hydrogen, oxygen, carbon, nitrogen, etc. Alternatively, neutrons scatter based on the isotopic nature of an element, illustrated in the difference between scattering cross section of hydrogen and deuterium with neutrons shown in Figure 1.12. This difference in contrast can be useful for measurements with SANS, and allow the scattering from different structures within the system to be highlighted using a technique referred to as contrast matching.

An example of contrast matching is shown in Figure 1.13. Having components in a system with a greater difference in SLDs creates greater contrast, meaning the scattering associated with that system becomes more intense. In a multi-component system, it can be difficult to decouple the scattering associated with each component, but contrast matching can emphasize a single component. The large difference in SLD of Hydrogen and Deuterium is crucial for this technique. The SLD of many materials, such as polymers or solvents, will fall between that of Hydrogen and Deuterium, which means a precise mixture of hydrogenated or deuterated can exactly match the SLD of a variety of samples.

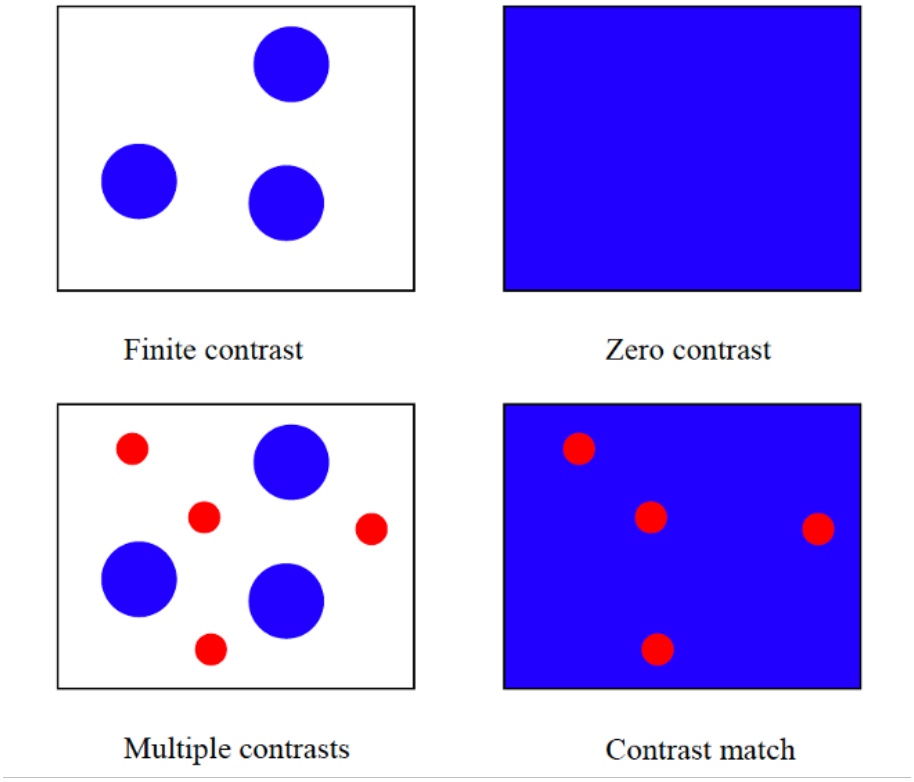

Figure 1.13: Examples of different types of contrast: "finite contrast" shows a two-component system with differing SLDs; "zero contrast" shows a system where each component has the same SLD; multiple contrasts shows a 3 component system, each with different SLDs; "contrast matching" shows a 3 component system where two of the SLDs are equal, emphasizing the third component [30].

1.2.2.4 Data analysis and interpretation

While interpreting scattering data can vary based on the experiment, a general case of the equation for scattering intensity is helpful for a basic understanding of scattering data. Equation 1.5 models the overall macroscopic scattering cross section, or absolute scattering intensity, for a system of globular inhomogeneities or objects in a matrix or solvent.

$$I(Q) = \phi \Delta \rho^2 P(Q) S(Q) \tag{1.5}$$

Where Φ is the volume fraction of the scattered object or particle, $\Delta\rho$ is the contrast factor, P(Q) is the form factor, and S(Q) is the structure factor [30,31]. The form factor is representative of intra-particle interactions and takes into account the spatial extent and shape of the scattering object or particle [32]. Generally, the form factor is given by the Fourier transform of the density distribution of a scattering object. The structure factor represents the inter-particle scattering and accounts for interactions between particles in a sample.

Small angle scattering data can be interpreted in many ways, but a common place to start is to look at exponential dependence of intensity on the scattering angle, Q, in the scattering data, as shown in Figure 1.14 [30]. Identifying regions of exponential Q dependence on intensity can discern the shape or dimensionality of a particle, or the behavior of a polymer chain. Additionally, the particle size can be approximated from the corresponding Q range of the slope.

Identifying a plateau in scattering data can reveal a radius of gyration, R_g, through the Guinier approximation. In a given range of data qRg < 1, the Guinier approximation is valid, and can be estimated by the following equation [30]:

$$I(Q) \approx exp\left(-\frac{Q^2 R_g^2}{3}\right) \tag{1.6}$$

An example scattering function of a cylindrical model is plotted in Figure 1.15. In the plateau region at low Q, the size scale corresponds to the large R_g^2 of the overall particle. At intermediate Q, the size scale corresponds to the 1-dimensional aspect of the cylinder, the radius. Beyond this region at high Q, the decay corresponds

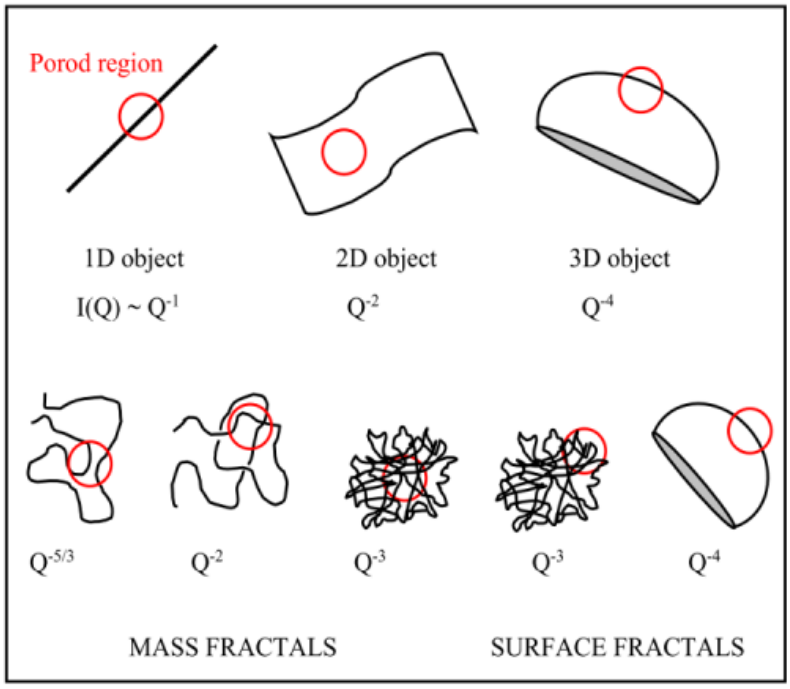

Figure 1.14: Examples of how the expo nential behavior of the scattering intensity can identify the dimensionality of a particle, or the behavior of a polymer chain [30].

to the surface fractal typical of Porod scattering, as shown previously in Figure 1.14 [30]. Obtaining data with a plateau requires a sufficiently low concentration, as with increasing concentration, inter-particle interactions can begin to dominate the scattering at larger length scales, resulting in the low Q plateau no longer being visible.

One other common feature in scattering data is a peak. A peak, or a local maximum if it is broad, results from constructive interference from inter-particle scattering and is manifested in the structure factor. A broad peak can be a sign of a standardized interparticle distance in a colloidal suspension, or at much smaller length scales a sharp peak can indicate the presence of precise crystalline ordering. Measuring crystalline peaks can be accomplished using WAXS, which is employed in this work. WAXS is the same technique as X-ray diffraction (XRD), measuring the

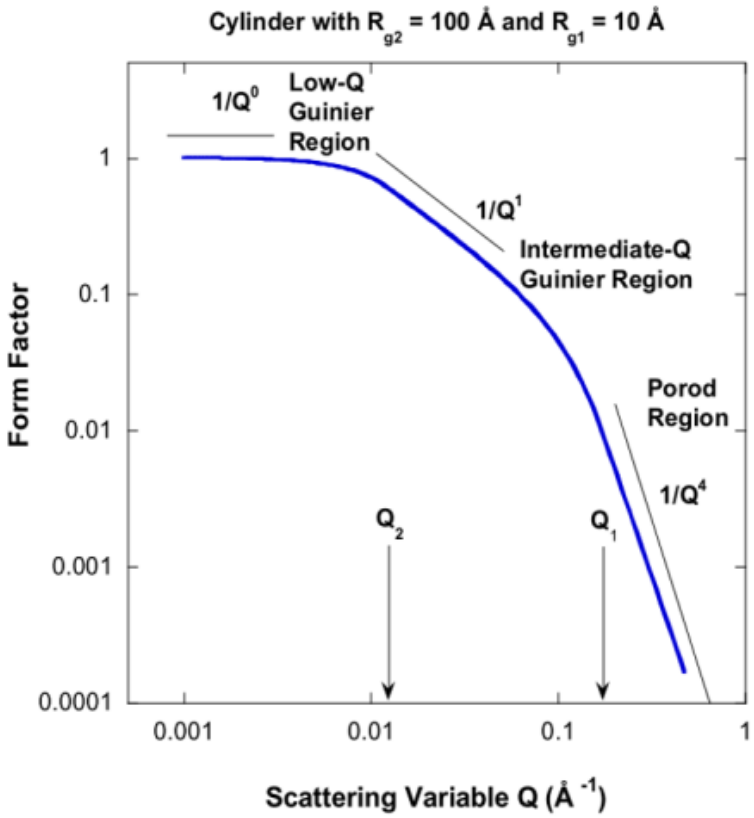

Figure 1.15: Example scattering curve of a cylinder, showing the two guinier regions associated with the R_{g2} of the overall cylindrical particle, and R_{g1} associated with the particle radius [30].

same general Q range, but is experimentally conducted like small angle scattering at very small sample-to-detector distances. Based on Bragg's law as previously discussed, the peaks in scattering intensity will correspond to the spacing of a crystal lattice based on the relation of $d = 2\pi/Q$.

1.2.2.5 Facilities

SANS in this work was conducted at the Center for High Resolution Neutron Research at the National Institute for Standards and Technology on the NG-B 30 meter neutron beamline [33]. SAXS and WAXS were conducted at the University of

Maryland X-ray Crystallography Center, using the Xenocs Xeuss instrument.

1.2.3 Fourier transform infrared spectroscopy

Infrared radiation spectroscopy involves the passing of infrared radiation through a sample. A portion of the radiation is absorbed by the sample depending on the molecular content and interaction within the sample. This can be used to identify materials, used as quality control of a sample, and used to identify the relative amounts of components in a mixture. FTIR allows for a fast scan of a sample at all infrared frequencies at the same time. To accomplish this, an interferometer is used to split the IR beam in two, modifying the optical path of one beam, then recombining them to form an optical interference pattern called an interferogram. The resulting beam exiting the interferometer is infrared radiation that is oscillating in intensity. After the infrared radiation beam interacts with the sample, an interferogram is obtained that is converted to a single line absorbance spectrum through Fourier deconvolution. A typical experimental setup for FTIR is shown in Figure 1.16 [34].

As infrared radiation passes through a sample, certain wavelengths are absorbed by the sample depending on its chemical structure. Absorption only occurs when the vibrations of a molecule caused by the incident beam result in a change in a dipole moment, or a change in vibrational energy level. Each quality and type of vibration for a given molecule corresponds to the energy and frequency associated with a given wavenumber of the incident infrared radiation beam. As particular wavenumbers of infrared radiation are absorbed by the sample, the resulting beam

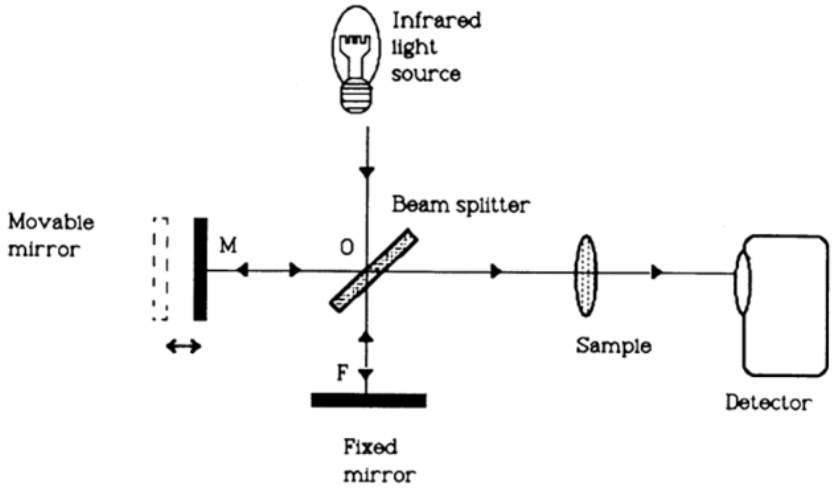

Figure 1.16: Schematic showing the experimental setup of an FTIR device, including the infrared radiation source, interferometer setup with the beam splitter, fixed mirror, and movable mirror, the sample, and the infrared radiation detector [34]. © 1991

hitting the detector will include a lower intensity of those wavenumbers, resulting in a change in measured intensity (presented as absorbance or transmission). An FTIR spectrum is compiled by plotting the measured intensity for each wavenumber in the infrared radiation spectrum with wavenumbers from about 4000 to 400 cm-1 [35]. Calculating the transmission or absorbance from the measured intensity can be done using equations 1.7 and 1.8 respectively, where %T is percent transmission, A is absorbance, Is is the incident beam intensity, and I is the resulting beam intensity after passing through the sample.

$$\%T = 100 \times \left(\frac{I_s}{I}\right) \tag{1.7}$$

$$A = log\left(\frac{I_s}{I}\right) \tag{1.8}$$

FTIR is a useful technique for understanding polymers. It can be used to

identify functional groups, measure changes in composition or relative concentration of groups or components within the sample or used to measure structural properties like crystallinity, level of oxidation, or particle contamination. For this work, FTIR was employed to track the removal of EMIMAc from a concentrated cellulose and ionic liquid gel by identifying the changes in absorbance of a particular peak associated with EMIMAc at a wavenumber of 1640 cm-1.

A typical FTIR measurement can be done in transmission mode, in which the infrared radiation beam passes through a sample. However, for some samples, such as the cellulose and EMIMAc gels measured in this work, the thickness is large enough that the beam cannot pass through the sample effectively. In this case the attenuated total reflectance (ATR) tool is used to conduct a measurement in reflective mode. In this case the sample is pressed against a flat crystal surface, usually diamond, through which the infrared radiation beam is internally reflected. This is a surface technique, so it only measures a limited region of the sample, but it allows for the measurement of thicker samples non-destructively.

1.2.4 Rheology

Rheology is a technique that can measure the mechanical behavior of softer materials, such as fluids or soft gels. For thick viscous fluids and gels, often a sample is measured using two parallel plates. A rotational force is applied to the upper plate resulting in a mechanical response, which can yield information about the mechanical properties of a sample. For less viscous samples, concentric cylinders

or conical geometries are employed, but for fluids and soft gel-like solids, aligned parallel plates can be used, as shown in Figure 1.17.

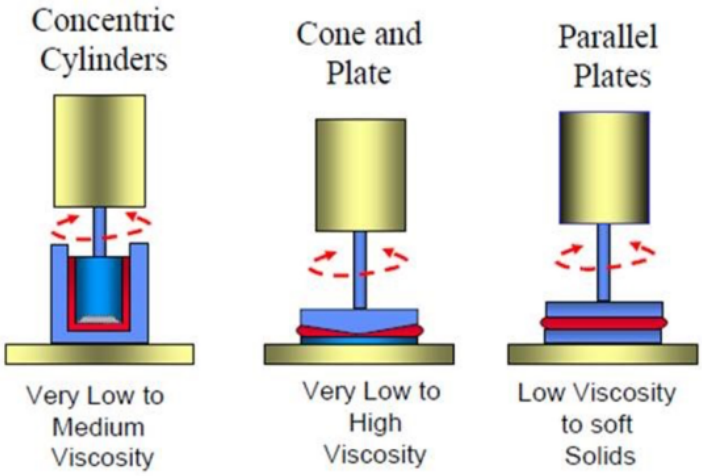

Figure 1.17: Example geometries and experimental setups used in rheology experiments [36].

With parallel plates, as was used in this work, the upper plate is rotated, causing a shear stress in the sample (see Equation 1.9).

$$\tau = \gamma G \tag{1.9}$$

Where τ is the shear stress, γ is the shear strain, and G is the shear modulus of the sample.

In this work, rheology was used to measure the point at which a gel transforms into a viscous fluid. To accomplish this, the gel is first measured using a simple strain ramp test, in order to identify the limits of the linear elastic region, or the area of strain before the gel begins to yield or plastically deform. A value of strain is taken within that region and an oscillatory test of that strain is conducted as a

function of temperature. This involves inducing an oscillatory strain on the sample that is high enough to measure its mechanical response, but low enough that the gel does not yield.

The induced strain is given by a sinusoidal equation as a function of the frequency, ω, and time, t. The response of the sample is measured through the change in the phase lag of the frequency curve. This response is quantified by the storage modulus, G', which measures the elastic component, and the loss modulus, G", which measures viscous component of the response. The strain, storage modulus, and loss modulus are given by Equations 1.10-1.12, and in accordance with Figure 1.18.

$$\gamma(t) = \omega\gamma_0 sin\left(\omega t + \frac{\pi}{2}\right) \tag{1.10}$$

$$G' = \frac{\tau_0}{\gamma_0} cos(\delta) \tag{1.11}$$

$$G'' = \frac{\tau_0}{\gamma_0} sin(\delta) \tag{1.12}$$

As the sinusoidal mechanical input is applied to the sample, the response is measured through the time delay in the sample response time through the phase angle, δ, which measures the time between the sine curves of the input and sample response, as illustrated in Figure 1.18. The ratio of the loss modulus to the storage modulus results in a value called the phase lag, or $\tan(\delta)$, which is a measure of the internal friction within the sample.

$$tan(\delta) = \frac{G''}{G'} \tag{1.13}$$

If $\tan(\delta) > 1$ the viscosity is dominating the mechanical response indicating the

behavior of a viscous fluid, while if $\tan(\delta) < 1$ the modulus is dominating the response indicating the behavior of a solid gel. The point at which $\tan(\delta) = 1$ is referred to as the gel point and is the point at which a gel transitions between an elastic solid or a viscous fluid. In this work, rheology is used to measure the existence of a gel point in a soft gel of cellulose and ionic liquid, and the temperature at which it occurs.

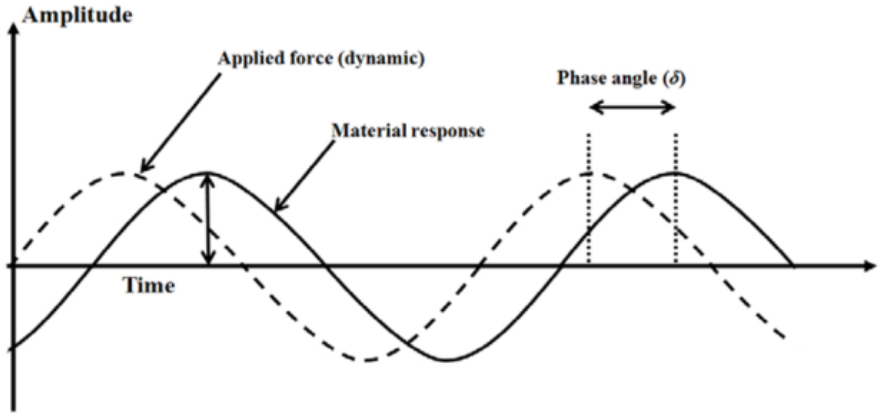

Figure 1.18: Plot of the applied amplitude of the rheometer over time showing the sinusoidal input during a frequency sweep and the phase lag of the material response [36].

1.2.5 Atomic force microscopy

AFM is a technique that is ideal for measuring surface topography of a sample, as it tends to have high contrast in the Z direction from the surface of the sample. AFM relies on atomic level surface forces exerted on a tip immediately close to or in contact with the surface of a sample. Typically, there are two modes for standard AFM measurement, contact mode and tapping mode, which are employed depending on the material being imaged and the desired resolution. The tip of an AFM is supported on the end of a small cantilever. Subtle interatomic forces exerted on the

tip by the sample surface result in slight deflections in the cantilever as the tip is moved across the surface, allowing the topography to be mapped for an area of the sample anywhere from 100 nm to 10's of microns in width. Contact mode can be damaging, particularly for soft samples or substrates since the lateral motion across the sample can create large forces, so this is typically reserved for very hard samples.

An example of the interatomic forces that govern the deflection of the cantilever can be described in the plot shown in Figure 1.19. The repulsive region indicates that the tip is close enough to the sample that it is being pushed away by interatomic forces, while the attractive regime causes the cantilever to bend toward the sample. Contact mode is conducted region A in Figure 1.19 in the repulsive regime, in which the tip directly exerts forces onto the sample surface during scanning. The distance between the tip and sample is kept constant by a feedback circuit that adjusts positioning to account for changes in sample height during scanning [37].

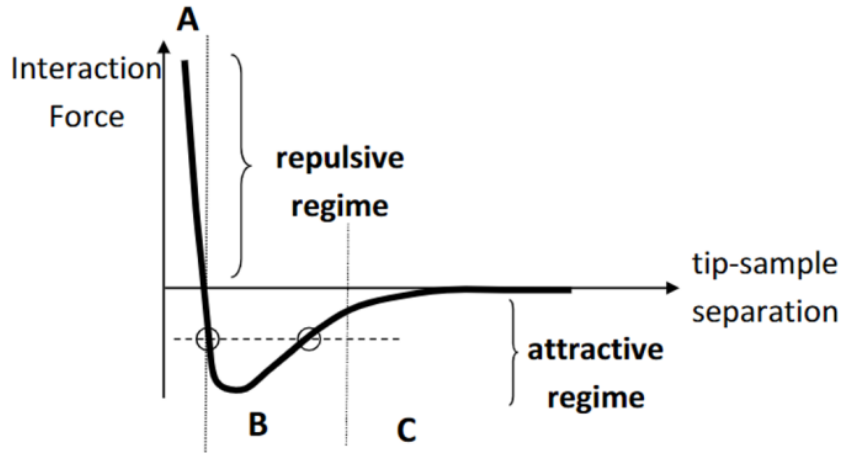

Figure 1.19: The atomic force plotted against separation distance that governs the cantilever response in an AFM [37].

Non-contact mode, or tapping mode, is conducted in region C in the plot, in which minor deflections of the cantilever result from attractive forces exerted

by the sample surface. In tapping mode, the cantilever is intentionally vibrated at or near its resonant frequency. A feedback controller is employed to maintain a constant oscillatory amplitude, and the height of the sample under the tip is indirectly measured from the feedback inputs required to maintain the oscillations. Since tapping mode is non-destructive and more suitable for soft materials such as polymers, it is the method employed for this work.

An example of an experimental AFM setup for tapping mode imaging is shown in Figure 1.20. A laser is aimed at the top of the cantilever and reflected into a photodiode, which detects any changes in the height of the cantilever. The function generator drives the cantilever with a fixed frequency and an amplitude that is maintained at a constant setpoint, as determined by the lock-in amplifier. The inputs that are used to maintain the oscillatory amplitude are representative of the height of the sample at a given lateral position across the sample surface. As scans are run a two-dimensional topographical map of the sample surface is created to produce an image [38].

In this work, AFM is used to characterize the dimensions of individual CNF produced from the TEMPO oxidation and mechanical homogenization process, and to image thin films of all-cellulose composite mixtures. Samples are prepared by thoroughly diluting a solution or suspension of material, then applying to an incredibly smooth substrate, such as a freshly cleaved mica disc or a silicon wafer that has been cleaned using a UV/ozone process. The solvent is removed by drying at ambient conditions, spinning, or in a vacuum oven. Any further solvent, in this case ionic liquid, is removed by thoroughly washing [39].

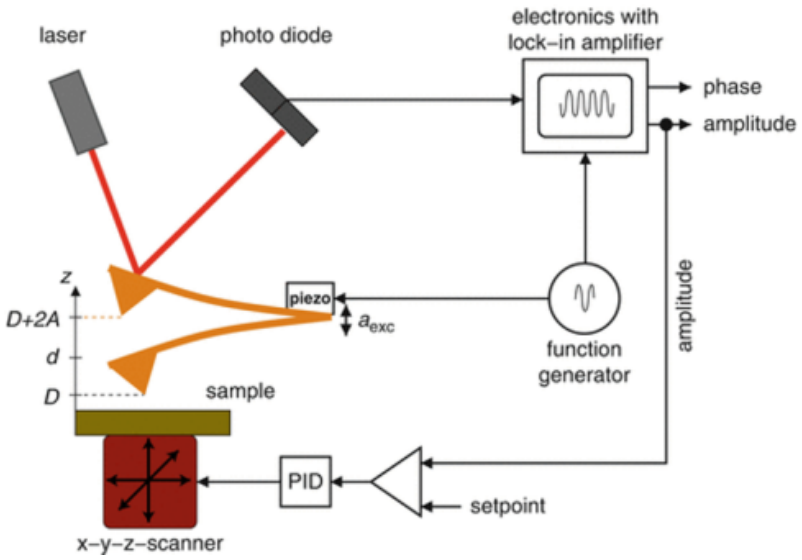

Figure 1.20: Experimental setup for an AFM measurement [38]. © 2012

1.2.6 Hazemeter- UV/Vis spectrometer

Measurements of light transmission and haze are commonly measured optical properties of materials. Transparency is a crucial measurement for polymer samples due to the ubiquity of transparent polymers commonly found in everyday life. Haziness measures the ratio of light scattered by the sample versus the light that is transmitted through the sample. Haze can be a beneficial property for materials such as coverings for solar cell, where increased haze can maximize light scattering across the surface, or a disadvantage when desiring full optical transparency, like in flexible electronics or packaging.

A UV/Vis spectrometer that is fit with a 150 mm integrating sphere can provide accurate transmittance measurements of high scattering samples, as it is able to measure with less loss of light using internal reflection within the sphere. The experimental setup for a transmittance measurement using an integrated sphere

is shown in Figure 1.21a. Measurement light is passed through a sample that is placed immediately at the aperture opening of the integrated sphere, so both the transmitted and the scattered light that pass through the sample are able to be measured.

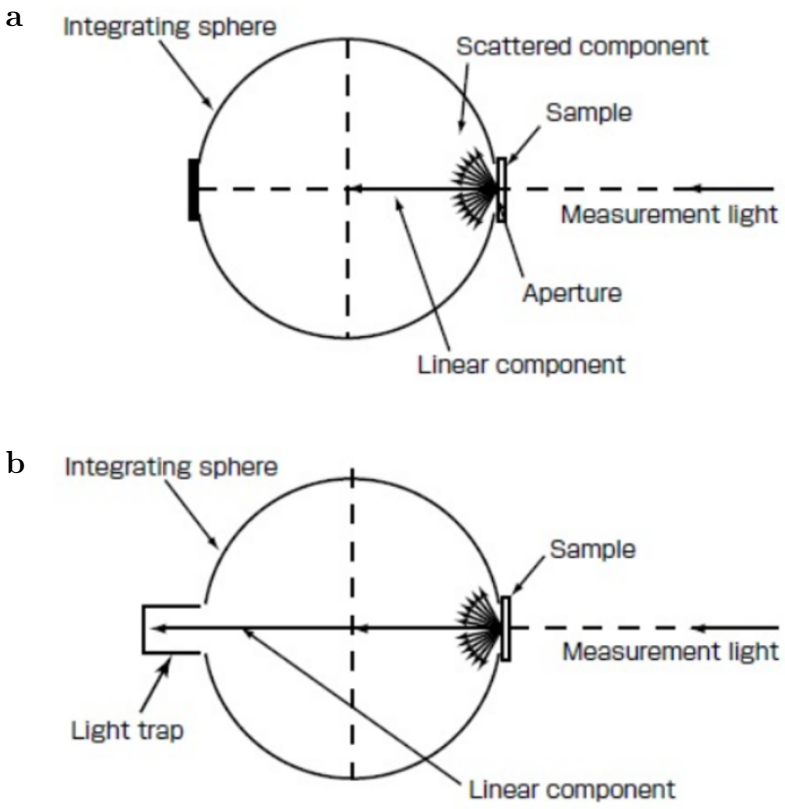

Figure 1.21: Experimental setup using an integrated sphere to measure a) standard transmittance and b) diffuse transmittance for measuring the percent haze in a sample [40].

For haze measurements, the standard surface located at the back of the sphere is replaced with a light trap that captures all simply transmitted light, so the only light measured by the integrating sphere is light that has scattered from the sample, referred to as diffuse transmittance. A schematic detailing the setup of a diffuse transmittance measurement is shown in Figure 1.21b. To calculate the haze of a

sample, you divide the diffuse transmittance value by the standard transmittance as shown in equation 1.14, essentially calculating the amount of light that is scattered out of all the light that is transmitted through the sample without being absorbed or reflected [40].

$$Haze\% = \frac{T_{diffuse}}{T} \tag{1.14}$$

1.2.7 Tensile testing

One of the most fundamental relationships in materials science is between stress and strain. Strain, ϵ, is the deformation response of a material under a given load, given by Equation 1.15, where L is the length of the tested material. Stress, σ, is measure by dividing the force of a load by the cross-sectional area of a material, given by Equation 1.16, where F is the applied tensile load and A is the cross-sectional area. Young's modulus, E, is a measure of stiffness of the material, and is measured by the change in stress and strain in the linear-elastic deformation phase, given by Equation 1.17.

$$\epsilon = \frac{\Delta L}{L} \tag{1.15}$$

$$\sigma = \frac{F}{A} \tag{1.16}$$

$$E = \frac{d\sigma}{d\epsilon} \tag{1.17}$$

This elastic relationship can be observed in the example stress-strain plot in Figure 1.22.

The initial region of the curve is defined by the Young's modulus, E, being the

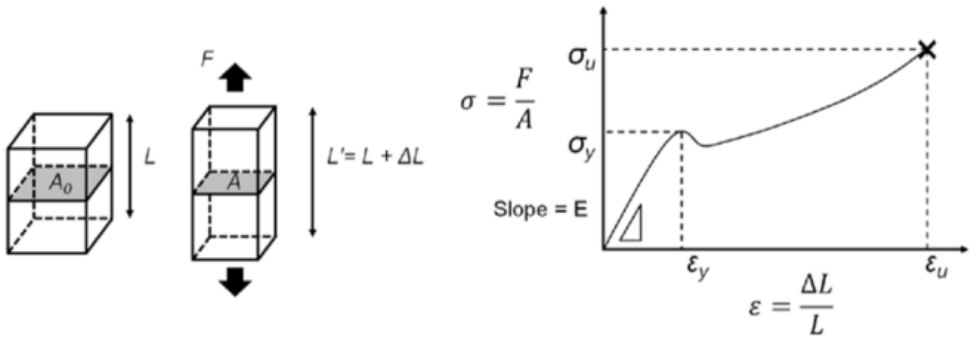

Figure 1.22: Example stress vs. strain curve and a schematic of material response to an applied tensile load [41].

slope of the linear elastic region. This deformation being elastic indicates that the material will return to its initial shape after the applied load. The point at which the material begins plastically deforming is referred to as the yield point, where σ_y is the yield stress and ϵ_y is the yield strain. This yield point typically occurs shortly after the linear elastic curve and can be calculated by using a 0.2% strain offset and extrapolating the slope to the point at which it intersects the stress-strain curve.

After the yield point, the material begins to plastically deform, or deform in a permanent and unrecoverable manner. Plastic deformation continues until the sample fails, which is indicated by the ultimate stress and strain, σ_u and ϵ_u respectively. In this work, tensile testing is conducted using a dynamic mechanical analyzer (DMA), specifically the TA Q800 with the tensile film testing attachment. The experimental setup is shown in Figure 1.23. The top clamp is fixed to the instrument, while the bottom clamp is left floating. During tensile testing, the applied force pulls downward on the floating bottom clamp, applying the load to the film. Sample preparation of cellulose films for tensile testing is described in Chapter 4 of this document.

Figure 1.23: Experimental setup of a dynamic mechanical analyzer with attached film tension clamp [41].

1.2.8 Scanning electron microscopy

SEM is a technique commonly used in the field of materials science to identify nanoscale structures in a sample with high-resolution and high magnification imaging [42]. In particular, SEM has been a powerful tool for the field of polymer science and engineering, both in establishing a link between synthesis or processing and polymer microstructure, and in understanding the relationship between mechanical properties and fracture or deformation microstructure [43–46]. For this work, the Hitachi SU-70 provided by the University of Maryland Advanced Imaging and Microscopy Laboratory (AIMLab) was used to image samples.

Figure 1.24 shows a schematic detailing the major components of a typical

SEM configuration. At the top of the column in the image is the electron gun. This both produces electrons to form the beam, and accelerates them to an energy level typically between 0.1 and 30 keV [42, 43]. In the Hitachi SU-70 SEM in the UMD AIMLab, a field emission gun is used. The diameter of the electron beam is focused, aligned, and condensed, at multiple stages using electromagnetically controlled lenses and apertures, which allows the beam to focus on very small spots on the sample. The column and sample chamber are typically held under very high vacuum so air does not scatter electrons from the beam. The electron beam passes through the sample, and images are produced from electron detectors based on different types of sample-electron interactions [43, 47]. For this work, images shown were gathered using transmitted electrons only.

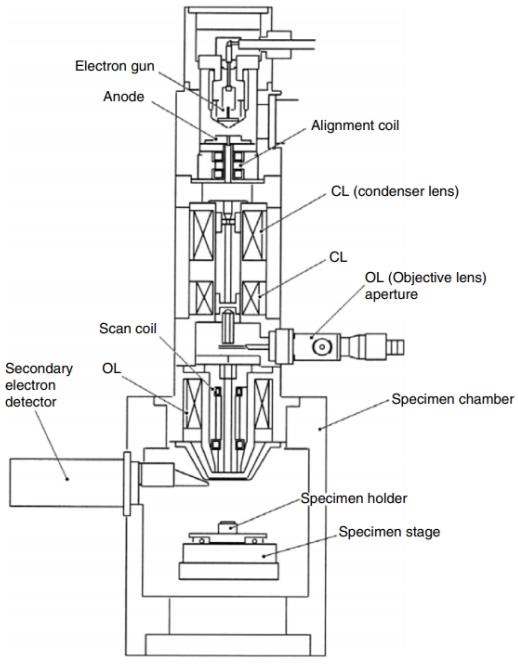

Figure 1.24: Schematic of a JSM-5410 scanning electron microscope [43]. © 2007

Polymers, like cellulose, present some difficulties when being imaged in SEM,

so there are techniques and preparations that must be followed to obtain the highest quality images. First, contrast in SEM is often governed by atomic number (i.e. number of electrons) of elements in a sample. Most polymers consist of low atomic number materials- in the case of cellulose, carbon, hydrogen, and oxygen- so it can be difficult to obtain sufficient contrast for identifying features at the nanoscale [45–47]. Additionally, cellulose is a non-conductive material, which results in a charging effect due to electron irradiation from the beam [48]. There are two solutions that can ameliorate the problems listed above. First is depositing a thin coating of a conductive material such as carbon, gold, silver, or tungsten onto the surface [46]. For this work, a carbon coating was used.

The second solution is to measure samples at a low acceleration voltage, typically between 0.1-0.7 keV. For this work, samples were imaged using 0.7 keV. At higher voltages, if the beam remains on the cellulose sample for more than a few seconds, deterioration in the form of curling, bubbling, or contrast darkening begins to occur, so a good technique is to focus on an area away from the intended image sight, then once the beam is aligned and focused properly, move to the feature and record an image quickly, before beam damage begins. Using a lower voltage means the contrast will be less sharp, so a balance is required between image quality versus risk of beam damage.

This work used SEM to examine the fracture surface of cellulose films after tensile testing. Samples were prepared for measurement using an SEM sample holder with a loading surface oriented parallel to the beam. Fractured film samples were adhered to the loading surface using carbon tape, with the fracture surface pointing

upward. These samples were then carbon coated, and loaded into the SEM for imaging. The fracture surfaces were examined together with the tensile testing results in order to identify the mechanism for mechanical failure in each film [47].

Chapter 2: Time-dependence of the TEMPO-oxidation of cellulose

2.1 Introduction

CNF are the most abundant natural nanomaterial in the world. They are produced by a TEMPO oxidation pretreatment followed by mechanical homogenization. Understanding how the structure of cellulose changes during this pretreatment can provide insight into how CNF is produced. This chapter initially provides a background and history of cellulose nanomaterials, including mechanical and chemical treatments and the different morphologies and fiber dimensions that result from each method of production. The research described in this chapter discusses the changes in structure of cellulose during the TEMPO oxidation process. The time dependence is studied by removing aliquots of fibers at various times during the reaction. The large-scale cellulose macrofibers experience swelling during the reaction, which is characterized by optical microscopy and fit to a log-normal distribution. SANS was also used to characterize the change in structure within the cellulose macrofibers at the nanoscale. The data was fit to a correlation length function model, indicating a separation between CNF at the nanoscale.

2.2 Background

2.2.1 Obtaining nanoscale fibrillated of cellulose

Nanofiber material with diameters at the nanoscale possess a high overall surface area to volume ratio, which can result in remarkably different mechanical, optical, electrical, or thermal properties than would be observed in the original bulk material [49]. Within the field of nanotechnology, research on nanofibers has been growing in recent years with applications in catalysis, electro-optical films, fiber-reinforced nanocomposites, microelectronics, gas-barrier films, cosmetics, flame-resistant materials, and more [50].

The most elementary motif within the hierarchical structure of cellulose are semi-crystalline nanofibers roughly 3-5 nm in diameter. These nanofibers are arranged in bundles that are roughly 12-16 nm in diameter. These bundles are then embedded within the overall matrix of the cell wall. To maximize the mechanical properties of cellulose based materials, a significant amount of research has gone into breaking down cellulose to its most elementary state, that of nanoscale fibers with high surface area to volume ratios. Before cellulose pretreatments were employed, the methods used to break down cellulose were solely mechanical, for example, high pressure homogenization, grinding, cryo-crushing, or ultrasonic and enzymatic methods [51]. However, because of the hierarchically organized layers of cellulose nanofibers held together with hydrogen and van der Waals bonding, these methods result in fiber diameters between 15-100 nm. This indicates that while mechanical methods can

break down the hierarchical structure of cellulose, it cannot break apart the bundles of nanofibers to the most elementary nanofiber structure [51, 52]. These purely mechanical processes for obtaining nanofibers are energy intensive and inefficient due to the tight network of hydrogen bonding between nanofibers within these bundles. Therefore, additional processing is required to break cellulose down to elementary nanofibers and obtain maximized surface area to volume ratio [52].

Chemistry-assisted surface modification of cellulose has been employed to work in tandem with mechanical methods, improve fibrillation efficiency, and fully separate cellulose nanofibers in the process. Typically charged functional groups are introduced on the surface of individual nanofibers to create a coulombic repulsion between them, encouraging full separation of the elementary nanofibers in the resulting suspensions. One method is acid hydrolysis using sulfuric acid (H_2SO_4), which helps break down amorphous regions between cellulose crystallites (see Figure 1.4a). After ultrasonic homogenization, this process yields cellulose nanocrystals, with dimensions of about 5-10 nm in diameter and 50-200 nm long. Cellulose nanocrystals (CNC) are different from CNF in that they do not contain the amorphous regions present between cellulose crystallites. Additionally, CNCs have larger diameters than CNF, which have diameters of roughly 2-4 nm. CNCs are currently being studied for applications as nanocomposite fillers and its ability to form liquid crystal suspensions, which can produce films with interesting optical properties [53]. While the high degree of crystallinity and one-dimensional structure make CNCs an ideal candidate for nanocomposite applications, fully separated cellulose nanofibers have a much higher aspect ratio and further increase the surface area to volume ratio, having greater

potential for improved mechanical properties in nanocomposites.

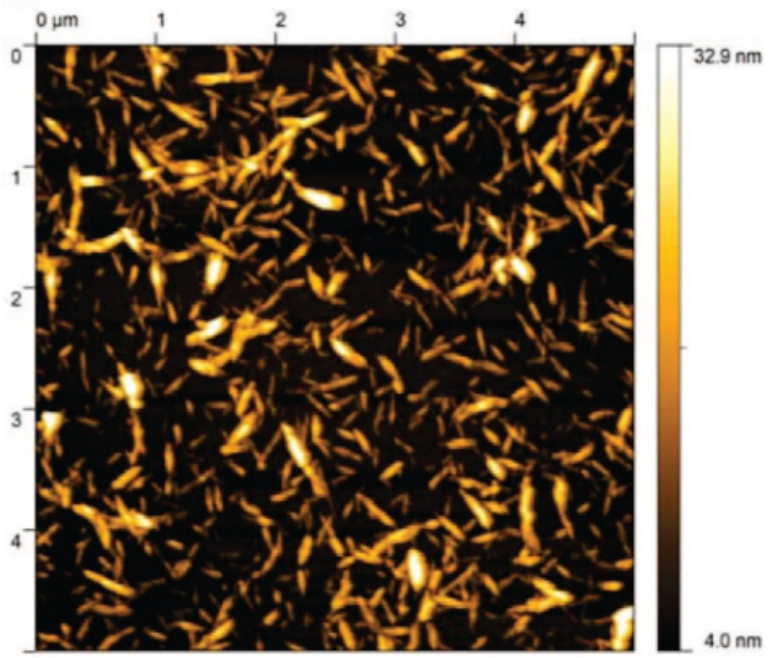

Figure 2.1: AFM images of cellulose nanocrystal particles dried onto mica surface [54]. © 2008

An AFM image of CNCs is shown in Figure 2.1, showing a wide array of diameters and relatively low aspect ratios [54]. In addition to the relatively low aspect ratios, another disadvantage is that yields of nanocrystals produced from the acid hydrolysis with H_2SO_4 are low, typically around 30-50% [55].

Using a mild enzymatic hydrolysis in combination with mechanical homogenization can produce higher aspect ratio fibers with diameters as low as 5 nm and lengths as long as tens of microns, as shown in the AFM images in Figure 2.2 [56, 57]. However, the images also show that while some 5 nm nanofibers exist, the bulk of the sample is dominated by larger fiber bundles as the nanofibers have been slightly fibrillated, but not fully separated to where individual nanofibers are visible. These mechanically homogenized cellulose fibers will be referred to as mi-

crofibrillated cellulose (MFC). Applications for MFC are as thickeners, components of filters, or as additives to paper products to improve the surface finish or mechanical properties [50].

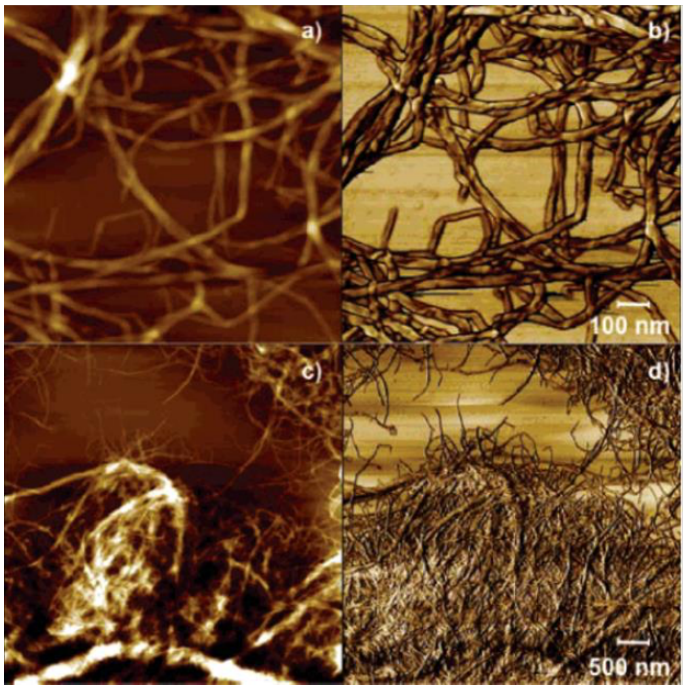

Figure 2.2: Height (a and c) and phase (b and d) images of microfibrillated cellulose produced from a mild enzymatic hydrolysis and mechanical homogenization, dried onto a mica surface. Images a and b are 1 x 1 μm and images c and d are 5 x 5 μm [56]. © 2007

Recently, a method of extracting individual elementary fibers has been achieved, yielding fibers of 2-4 nm in diameter and up to a few microns long through TEMPO mediated oxidation, followed by mechanical homogenization [58]. This homogenization can be accomplished through microfluidization, ultrasonication, or even stirring over a longer time period. The result is a very high yield of TEMPO oxidized cellulose nanofibers with a narrow dispersity of diameters of 2-4 nm and lengths of up to a few microns [58]. After homogenization, the suspensions can be purified by centrifuging to remove larger particles, resulting in yields over 90% by weight. While

diameters are consistent, apart from slight variations based on the original cellulose source, lengths can vary based on conditions such as degree of oxidation or source of cellulose [59].

2.2.2 TEMPO-mediated oxidation process

TEMPO is a water-soluble, widely-available, and stable hydroxyl radical, and has been used for efficient and selective conversion chemistry of hydroxyl groups to aldehydes, ketones, and carboxyl groups under mild conditions. TEMPO has been used in the oxidation of polysaccharides such as starch, amylodextrin and pullulan for selective conversion of the C6 primary hydroxyl to carboxylate groups present on the surface of nanofibers [60,61]. For this process, NaBr and TEMPO were dissolved into polysaccharide solutions in water at pH of 10-11, and NaClO is added as the primary oxidant to begin the reaction. When this same reaction is conducted with cellulose, a similar result is achieved. Figure 2.3 shows the TEMPO/NaBr/NaClO-mediated oxidation of cellulose, resulting in the selective oxidation of the C6 hydroxyl group to a charged sodium carboxylate group. During the reaction, NaOH is continuously added to maintain a pH of about 10-11 [62]. After oxidation, the original semicrystalline structure of the elementary cellulose nanofibers is maintained as the cellulose is not dissolved but separated.

The results of the TEMPO oxidation process can vary depending on the type of cellulose used. According to work done by Okita et. al., the size of the crystals present in elementary cellulose nanofibers (which can vary depending on the cellulose

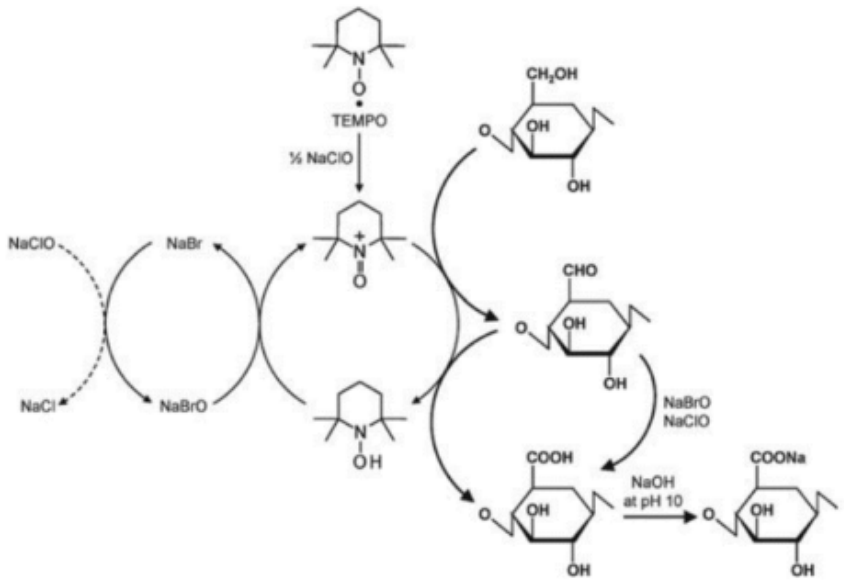

Figure 2.3: Selective oxidation of C6 hydroxyl groups of cellulose to carboxylate groups through TEMPO/NaBr/NaClO oxidation at pH 10-11 [62]. © 2010

source) can affect the carboxylate content of the cellulose [61]. Figure 2.4 shows the relationship between the elementary nanofiber (here labeled microfibril) width and the total carboxylate and aldehyde content after the reaction. The calculated carboxylate and aldehyde content of the cellulose, based on the amount of exposed hydroxyl groups on the surface of cellulose nanofibers, decreases with increasing crystallite size, as with smaller crystals, i.e. smaller nanofiber widths [61].

Additionally, the experimental results of maximum carboxylate and aldehyde content show a similar relationship with crystallite size, supporting the notion that only C6 hydroxyl groups present on the surface of the nanofibers are oxidized. The cross-sectional structure is based on well-established structures for cellulose I and is simplified to be represented by a rectangular cross section [63].

Once the TEMPO oxidation process is completed, the cellulose still retains its overall fiber macrostructure, and mechanical homogenization is necessary for separa-

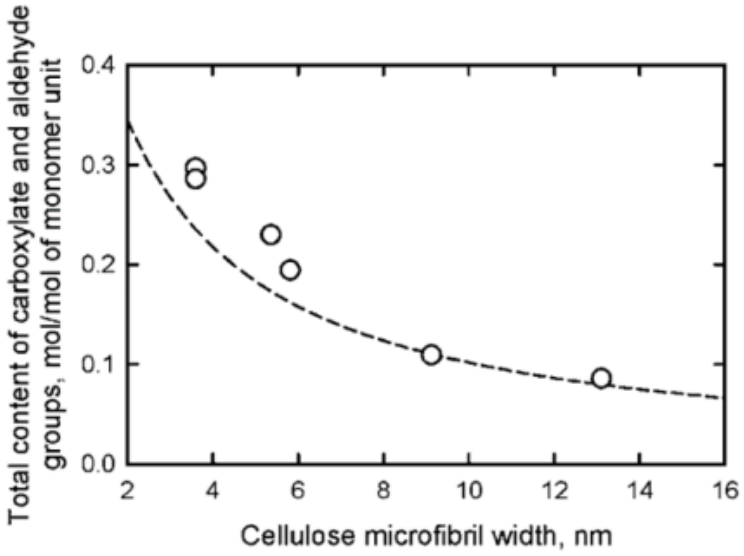

Figure 2.4: The calculated potential carboxylate and aldehyde content based on the available C6 hydroxyl groups on the surface of cellulose nanofibers (dotted line), and the experimentally obtained carboxylate and aldehyde content after the oxidation process (points) plotted against cellulose microfibril (i.e. nanofiber) width [61]. © 2010

tion of nanofibers. Different mechanical methods can be employed for this process, including ultrasonic homogenization, a high pressure microfluidizer, or a household blender, resulting in a transparent and viscous cellulose nanofiber dispersion in water. The TEMPO oxidation and mechanical homogenization treatments have, for the first time, produced wood cellulose fibers that have been successfully broken down to their individual elementary cellulose nanofibers. These nanofibers will have diameters of roughly 3-4 nm, and lengths of up to a few microns. Additionally, yields of over 90% were recorded using this process. Cellulose nanofibers prepared from TEMPO oxidation and subsequent mechanical homogenization will be referred to as CNF for the purpose of this work.

Compared to MFC and nanocrystalline cellulose, CNF shown in the AFM image in Figure 2.5 have overall smaller and more uniform diameters. Lengths are

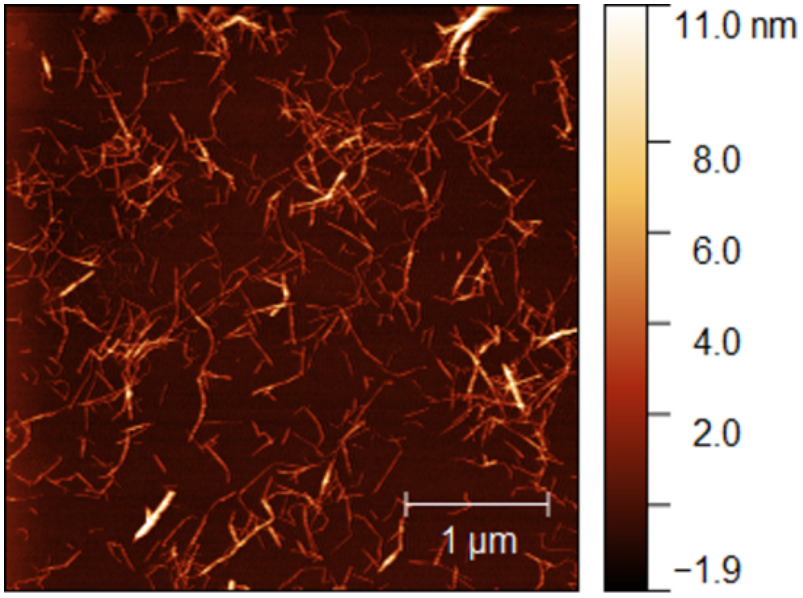

Figure 2.5: AFM image of separated, TEMPO oxidized, and mechanically homogenized cellulose nanofibers.

longer than nanocrystalline cellulose, as the amorphous regions within the elementary nanofiber are still present. In MFC, since there is no chemical pretreatment the nanofibers are often partially fibrillated off larger scale fibers and can also still be attached, whereas CNF particles are fully separated.

2.2.3 Properties of TEMPO oxidized cellulose nanofibers

Self-standing films can be produced from suspensions of TEMPO oxidized and homogenized cellulose nanofibers by filtering and thoroughly drying them. The resulting films, referred to as nanopaper in this work, have mechanical properties much stronger than that of normal paper, and conventional laminate polymers such as polyvinyl acetate (PVA) or cellophane. Figure 2.6 shows a comparison of the elastic modulus and tensile strength of TOCN, PVA, cellophane, paper, and PVA composites containing 20% CNF. The mechanical properties of CNF are shown to

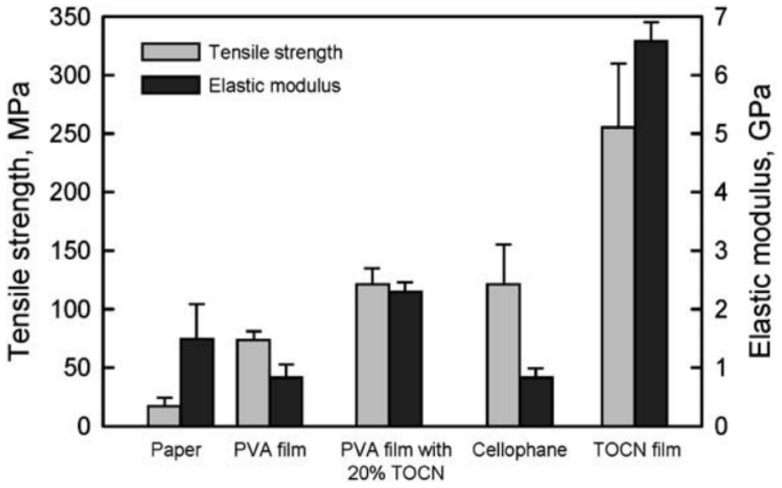

Figure 2.6: Tensile strength and elastic modulus comparison of TEMPO-oxidized cellulose nanofibers (TOCN), paper, and other laminate polymer films [52]. © 2011

be far superior to the other materials. The inherent stiffness and crystallinity of the elementary nanofibers provide a high elastic modulus. When compared to traditional paper, the overall surface-area to volume ratio of the CNF films is dramatically increased, allowing for greater stiffness and strength due to greater entanglement of nanofibers and increased hydrogen bonding sites [64]. Additionally, the high tensile strength of CNF films is due to a mechanism of breaking and reforming of hydrogen bonds during film deformation, as proposed by Zhu et. al. [65]. Figure 2.7a shows overlapping cellulose chains held together by hydrogen bonding. During deformation the hydrogen bonds break, but as the chains continue to move past each other additional hydrogen bonds can re-form. This allows the films to maintain a relatively large stiffness despite having already yielded plastically, as shown in Figure 2.7b. This mechanism results in a higher toughness as well as a higher stiffness and strength [65]. Conventionally as the stiffness and strength of a material increase, it becomes more brittle and more susceptible to a sudden crack-induced

failure, and decreased toughness. As a result, materials that are able to demonstrate high toughness and high stiffness and strength are often sought after in material selection [66].

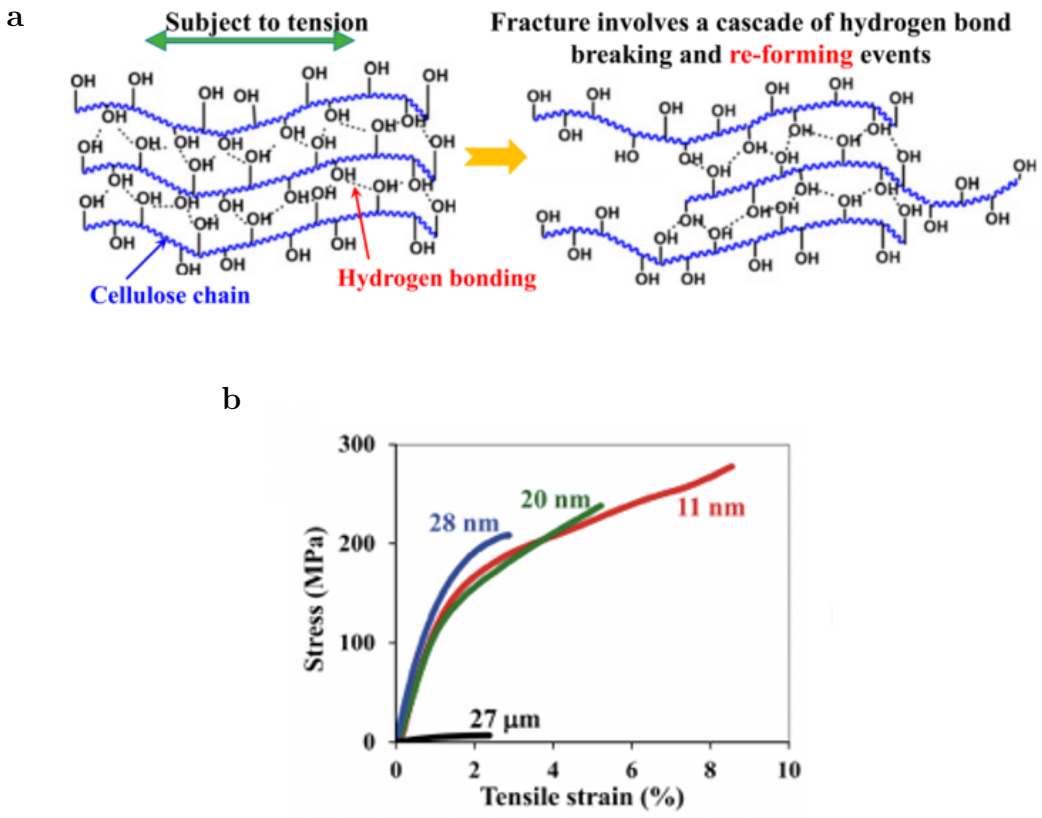

Figure 2.7: a) Proposed mechanism for breaking and reforming of hydrogen bonds between cellulose chains during deformation. b) Mechanical testing results of nanofibrillated cellulose films showing high toughness due to elongated plastic deformation region. Mechanical behavior varies depending on the average diameter of the fibers present in each film [65]. © 2015

CNF nanopaper also has interesting optical properties. Due to the gaps between nanofibers being smaller than the wavelength of visible light, nanopaper films are optically transparent [64]. Figure 2.8a shows the transparency of nanopaper, as text can clearly be read through the film. Haze refers to the scattering of visible

light that occurs in the film. Figure 2.8b shows an example of haze, as the initial size beam of light can be observed on the near side of the film, but after passing through the film scattering has caused the beam to broaden. The nanopaper film observed in Figure 2.8b has had MFC included in order to maximize haze for solar cell applications. The light transmission of CNF nanopaper films can be as high as 90-93%, which is greater than conventional transparent polymer films such as polyethylene terephthalate (PET), having a light transmission of about 92%. A comparison of the light transmission values can be observed in Figure 2.8c, indicating that CNF has transparency high enough to be used in transparent polymer film applications [67, 68].

One promising application for CNF nanopaper is as a transparent polymer substrate. Transparent and flexible electronic devices have been printed onto CNF nanopaper, such as transistors, antennae, sensors, organic light emitting diode (OLED) and solar cells. The relatively low surface roughness makes it better suited for device printing than conventional paper, and having a sustainable material that is not derived from petroleum for flexible electronic devices is important given the current global dependence on fossil fuels [68,69]. CNF films also have excellent oxygen barrier properties, and can therefore be useful in packaging and food containment materials [70]. CNF also is a promising candidate for composite reinforcement due to its one-dimensional shape and high stiffness and strength.

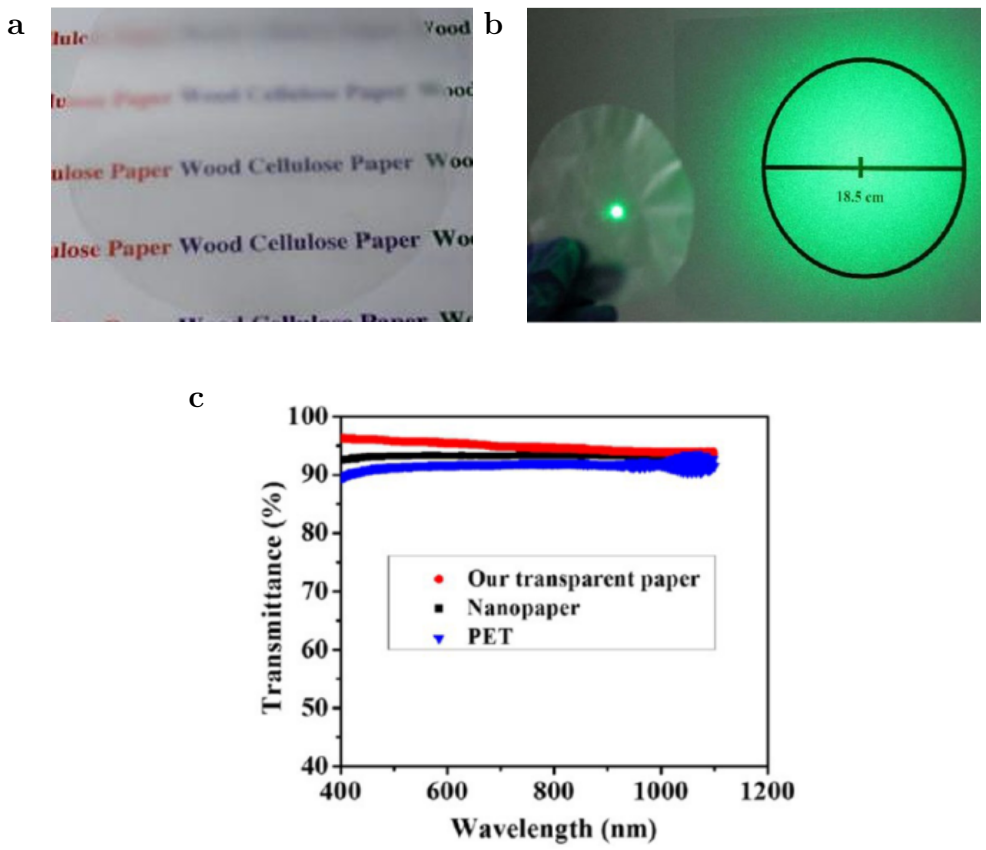

Figure 2.8: Photograph showing optical (a) transparency and (b) haze properties or transparent paper from dried CNF [66, 67]. © 2014

2.3 Experimental methods

2.3.1 Oxidation process

In this experiment cellulose was treated with the TEMPO oxidation reaction. Aliquots were removed from the reaction at different times for characterization. The process was adapted from previously reported protocols developed by Hu et. al. [71–74]. For the reaction, southern yellow pine bleached cellulose wood pulp with a moisture content of about 85% was used. A photograph of the cellulose

pulp is shown in Figure 2.9. Sodium hypochlorite solution, sodium bromide, sodium hydroxide, sodium carbonate, and sodium bicarbonate were all purchased from Sigma-Aldrich. Initially, 35 g of moist cellulose pulp (∼5 g dry) is mixed into DI water at 1% cellulose by mass, then TEMPO and NaBr are added and dissolved at concentrations of 0.1 and 1 mmol/g of cellulose, respectively. The reaction began by adding 35 mL of sodium hypochlorite solution (at 10-15% available chlorine), dropwise, into the solution. The pH of the solution was monitored with a pH meter and was initially raised to 10.5 with a 3 M solution of sodium hydroxide ($NaOH$), then maintained at 10.5 through the remainder of the reaction. The reaction lasted for 120 min, and products were collected throughout to be used for preparing CNF and for SANS study. A photograph showing the TEMPO oxidation reaction in progress is shown in Figure 2.9. At the start of the reaction, the pulp is not broken down and clumps can be observed, but the mixture becomes more homogeneous throughout the reaction as the oxidation occurs.

To characterize the fibers as a function of reaction time, aliquots of approximately 10 mL were removed from the reaction at intervals of 5, 15, 30, 60, and 120 minutes. After removal, the aliquots were immediately quenched with ten-fold volume of deionized water applied to halt the reaction. Aliquots were washed and filtered three times using a Buchner funnel with applied vacuum in order to fully remove the reactive agents. The collected cellulose was weighed to estimate remaining water content, then redispersed in water and diluted to concentrations of about 1% by mass. Cellulose concentrations were verified using oven drying.

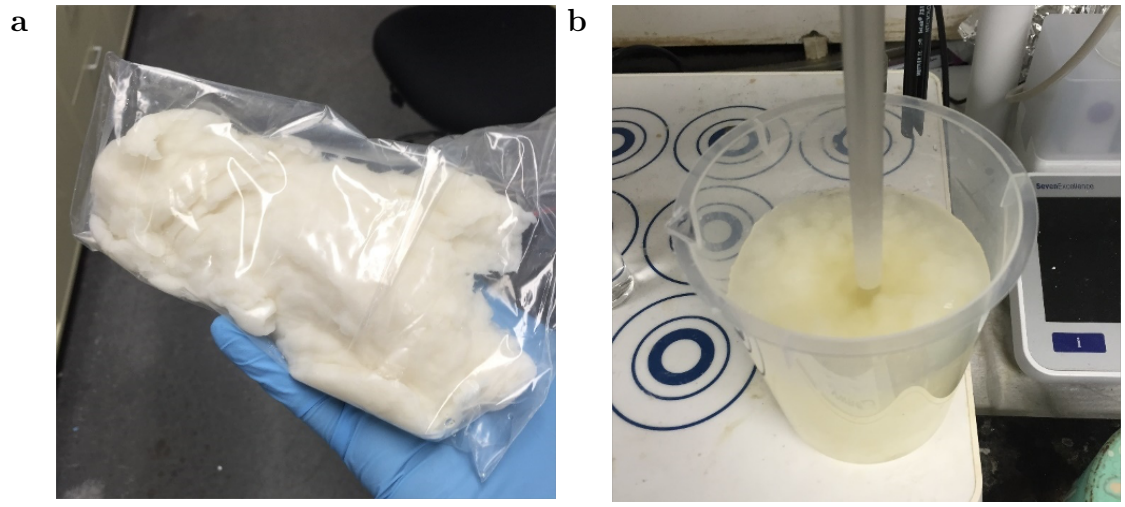

Figure 2.9: a) Bleached cellulose pulp at roughly 85% moisture content. This is the raw cellulose material used in the TEMPO oxidation reaction. a) TEMPO oxidation reaction underway. The pulp begins to break down and disintegrate throughout the reaction.

2.3.2 Optical microscopy

Optical microscopy was performed to examine the morphology of the samples using an Olympus Accura Zoom XB70 microscope. Samples were prepared by placing wet fiber aliquots of varying reaction times between a glass slide and cover slip. The fibers seen in optical microscopy are the macroscale cellulose fibers, i.e. the cellulose fibers that are observable in conventional paper. Diameters of each large-scale fiber seen in optical images were measured using ImageJ, and the resulting distributions were fit to a log-normal distribution function to estimate the center and width of the distribution [75].

2.3.3 Small-angle neutron scattering

To prepare the cellulose fibers for SANS characterization, the water in each aliquot was solvent exchanged with deuterium oxide (D_2O) by centrifuging and exchanging the supernatant for pure D_2O until the water (H_2O) content of the liquid was less than 1%. The fibers were then redispersed into D_2O at concentrations of 1% by mass using magnetic stirring and sonication. SANS measurements were conducted at the center for high resolution neutron scattering (CHRNS) on the NGB 30 m SANS instrument [33]. The samples were loaded into titanium SANS cells with quartz windows and a 1 mm path length. Each sample was measured at 1.33, 4.00, and 13.17 meter detector distances and a neutron wavelength of 6.0 Å. An MgF_2 lens configuration was also employed at 13 meters measurement at a wavelength of 8.4 Å, this focuses the neutron beam and minimizes the beam spot size to measure a lower Q range [76]. The overall Q range for the measurement was 0.001 to 0.5 $Å^{-1}$, allowing for probing at size scales from nanometers to hundreds of nanometers. The wavelength spread, $\Delta\lambda/\lambda$, was 14.8%.

2.3.4 Mechanical homogenization

CNF was produced from the TEMPO-oxidized fibers by homogenization using a NanoDeBEE microfluidizer from BEE International at a pressure of 30 kpsi. 120-minute TEMPO oxidized cellulose is prepared at a concentration of about 0.7 vol% (1 wt%) cellulose and then passed through the microfluidizer 1 to 4 times.

2.3.5 Atomic force microscopy

1 cm mica disks were freshly cleaved with a razor blade. Suspensions of each CNF sample were diluted 10,000 times with water, then a drop was placed on the freshly cleaved mica and allowed to dry at ambient conditions. Micrographs were obtained using an AFM -DI Nanoscope III multimode in the University of Maryland Surface Analysis Center. Diameter was measured using Gwyddion and measuring height profiles across individual fibers. Lengths were measured using ImageJ. Both lengths and diameters were organized into histograms and fit to a log-normal distribution. Roughly 300 fibers were measured for each sample set.

2.4 Results and discussion

2.4.1 Optical microscopy

The macrofiber samples from aliquots taken throughout the TEMPO oxidation reaction were imaged with an optical microscope as shown in Figure 2.10. Micrographs in Figure 2.10a and 2.10b were obtained using bright field, and micrographs in Figure 2.10c and 2.10d were obtained with cross-polarizers. At lower oxidation times, the fibers maintain their overall structure, with some swelling observed. At 120 min oxidation time, the macrofibers have swollen in diameter, and the overall structure of the fiber starts to break down. The fiber interface becomes less visible, and smaller scale fibers can be observed in the cross polarized images expanding outward.

The macrofiber widths were measured using ImageJ by manually measuring

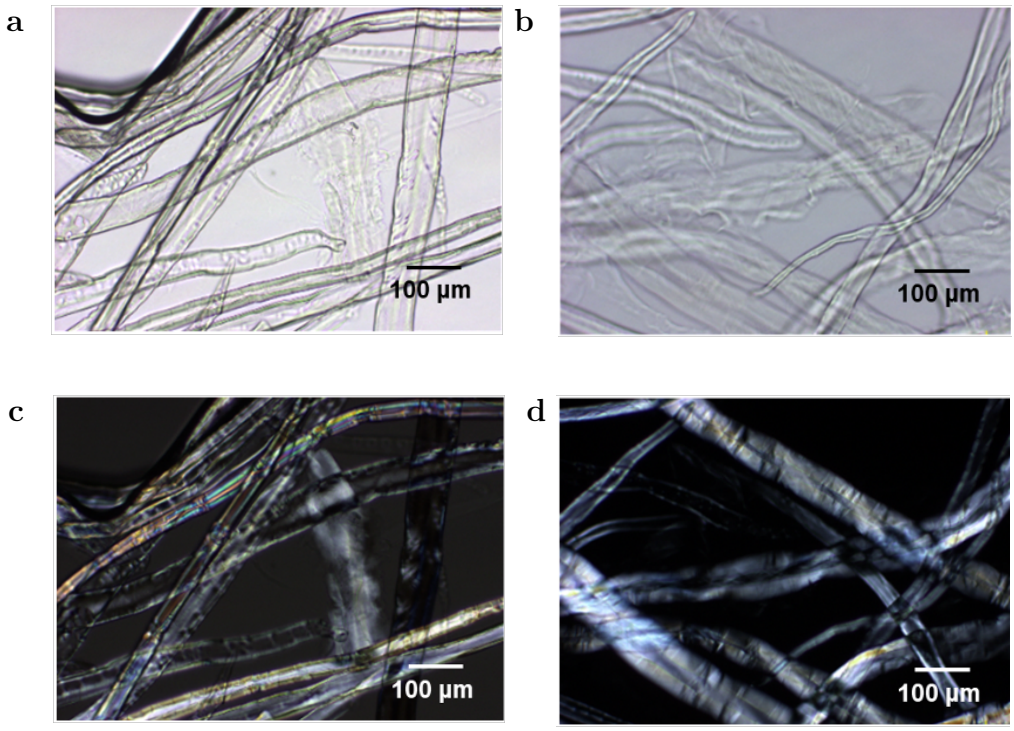

Figure 2.10: Optical microscopy micrographs taken of 5 (a,c) and 120 min (b,d) fiber aliquot samples in bright field (a,b) and using cross polarizers (c,d). throughout the TEMPO oxidation reaction. The left-hand column are bright field images, and the right-hand column is cross-polarized images taken of the 5- and 120-minute aliquot samples.

the cross section of each fiber. Results were obtained from a 1.4 mm by 1.8 mm micrograph for each sample. A virtual grid was overlaid onto aliquot micrographs, with each macrofiber cross section measured in each square of the grid to account for variations in width along each macrofiber length. At least 180 width measurements were obtained to estimate macrofiber diameter for each sample. The fiber diameter measurements were plotted in histograms, shown in Figure 2.11, with bins set by Equation 2.1, where σ is the standard deviation and N is the number of measurements.

$$\#\ of\ bins = 3.5 \times \sigma \times N^{\frac{1}{3}} \tag{2.1}$$

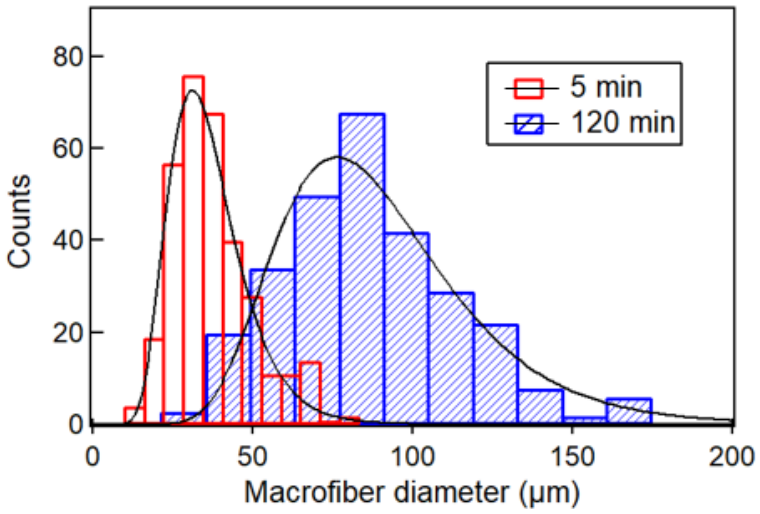

Figure 2.11: Log-normal distribution function fit to the macrofiber diameter histograms for 5- and 120-minute fiber samples. A best fit line for a log normal distribution is plotted for the histogram data.

The plot presented shows diameters for the 5 and 120 minute oxidized samples. The 5-minute sample histogram is centered on a diameter of about 30 μm, while the 120-minute sample histogram is broader and centered on a diameter of about 75 μm. The distributions were fit to a lognormal equation with the probability density function:

$$PDF = \frac{1}{x\sigma\sqrt{2\pi}} e^{-\frac{(ln(x)-\mu)^2}{2\sigma^2}} \tag{2.2}$$

The parameters μ and σ are used to define the location and shape of the natural logarithm of the distribution, they do not directly correspond to real diameter values. The mean diameter of a given log-normal distribution is given by the following equation:

$$Mean\ Diameter = \mu_M = e^{\mu+\frac{1}{2}\sigma^2} \tag{2.3}$$

The standard deviation of the distribution, used to describe how the distribution deviates from the mean diameter, is given by the following equation:

$$Standard\,deviation = \sigma_{SD} = \sqrt{(e^{2\mu+\sigma^2})(e^{\sigma^2}-1)} \tag{2.4}$$

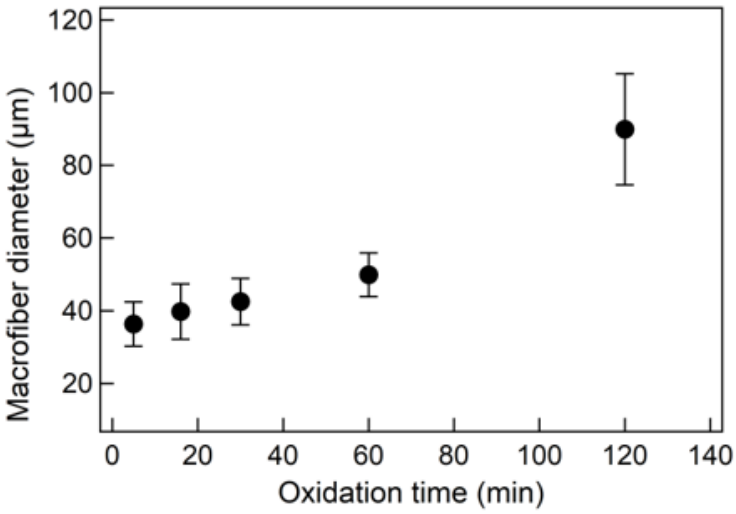

Figure 2.12: Mean diameter large-scale fibers of each aliquot sample from the TEMPO reaction plotted against reaction time. Diameters are measured from optical microscope images.

Figure 2.12 shows the mean diameter compiled from the aliquot samples of varying reaction time, with the error bars showing the standard deviation of the distributions. The mean diameter increases with reaction time, as was observed in optical microscopy. Additionally the standard deviation of these distributions increases dramatically at 120 minutes of reaction time, indicating that the macrofibers do not swell uniformly resulting in a larger variation in macrofiber diameter. This increase in diameter can be attributed to the effects of the TEMPO oxidation reaction. The surface level hydroxyl groups responsible for hydrogen bonding between

individual cellulose nanofibers have been converted to anionically charged sodium carboxylate groups. The anionic charge creates a repulsion that separates the individual nanofibers within the nanofiber bundles that make up the layers of the plant cell wall, resulting in swelling that is visible at the macroscale. The jump in diameter between 60 and 120 minutes indicates that the diameter does not necessarily increase linearly with time.

2.4.2 Small angle neutron scattering

SANS data of all 5 D_2O exchanged aliquots taken from the TEMPO oxidation reaction were obtained. The circular average of each corrected data file plotted against the scattering vector, Q, are plotted in Figure 2.13.

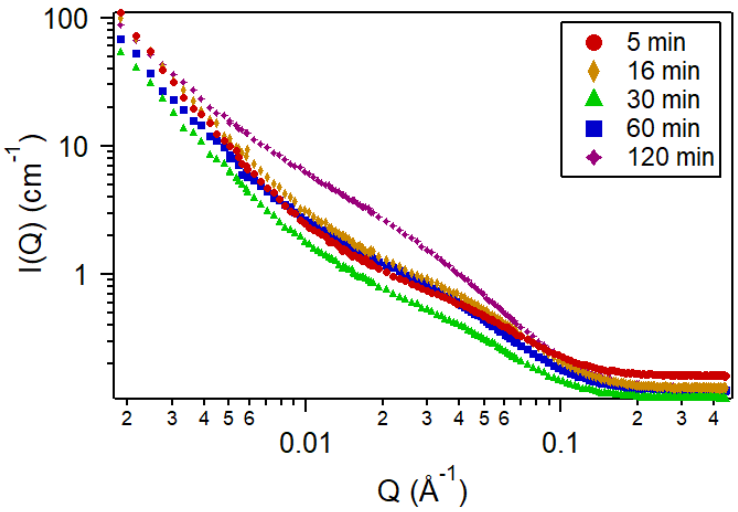

Figure 2.13: Reduced SANS data of each aliquot sample.

The scattering data for the cellulose fiber sample was reduced using SANS macros from the CHRNS through Igor, software [77] and the scattering data was modeled using the fitting software SASView. The data was modeled with a three-term

function of the form as shown in Figure 2.14:

$$I(Q) = \frac{A}{Q^n} + \frac{C}{1 + (Q\xi)^m} + B \tag{2.5}$$

Where A is the Porod prefactor, n is the Porod exponent, C is the Lorentzian prefactor, m is the Lorentzian exponent, ξ is the correlation length, and B is incoherent background. The three terms in this function represent three contributions to overall scattering, and are shown in Figure 2.14. The first term corresponds to intensity at low-Q, representing large aggregate structures. The second term corresponds to mid-Q scattering, representing the presence of nanometer scale structures. The third term is for incoherent background, which depends mostly on the hydrogen content in the sample [78]. SANS data is reported in Figure 2.13. From 5 minutes to 120 minutes, there is a distinct evolution in the mid-Q scattering between 0.01 Å^{-1} > Q > 0.04 Å^{-1}, while high- and low-Q scattering remains relatively constant.

The scattering background is subtracted by fitting a constant to the high-q region, accounting for the incoherent backgound portion of the fit function (shown in orange) in Figure 2.14. Due to the large size of macrofibers the samples may not have been homogeneous when loaded into SANS cells resulting in slightly different overall ratios of cellulose to D_2O in each sample. To account for this, after background subtraction SANS curves were normalized at the high-Q region. Since intensity will scale with overall volume fraction, this normalizes each sample based on varying cellulose content.

After normalization, a clear trend in the evolution of the mid-q region, roughly

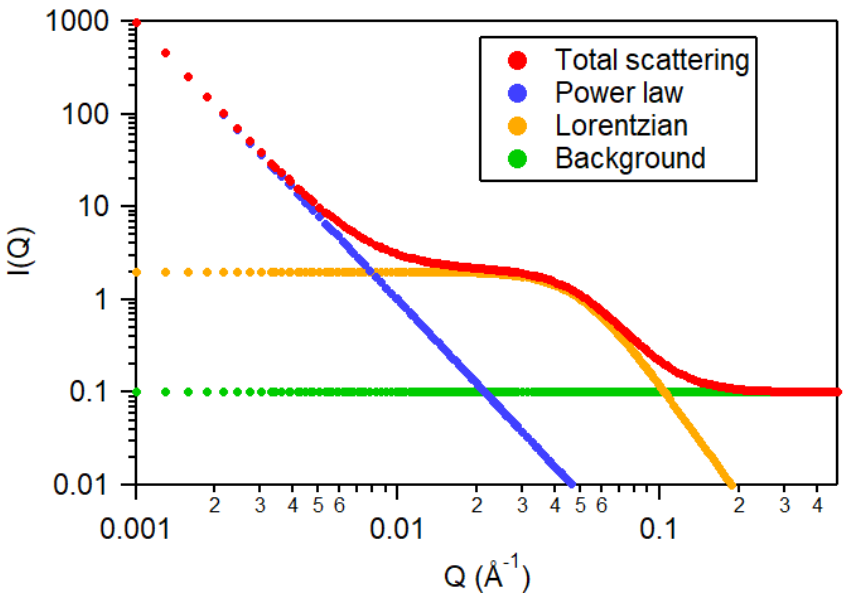

Figure 2.14: Plot showing the different components of the correlation length fitting function used for fitting the obtained SANS data.

0.01 $Å^{-1}$ < Q < 0.04 $Å^{-1}$, can be observed in the inset shown in Figure 2.15a. The intensity of the mid-q region increases with oxidation time, with the most significant increase being between 60 and 120 minutes. The intensity of the high-Q region remains the same for all samples, with the same power law dependence. The low-Q regions show a slight decrease in intensity with increased reaction time. The fitting parameters for each measured sample are displayed in Table 2.1.

The Lorentzian exponent, m, was fixed during the fitting, the background was measured separately prior to fitting and subtracted off, the remaining parameters were left unfixed. The power law exponent, n, shows a slight decrease with oxidation time, while both the Lorentzian scale and correlation length increase.

The correlation length is related to the distance between individual nanofibers within overall macrofibers. As reaction time increases, hydroxyl groups at the surface of the nanofibers are oxidized and become charged, creating electrostatic repulsion

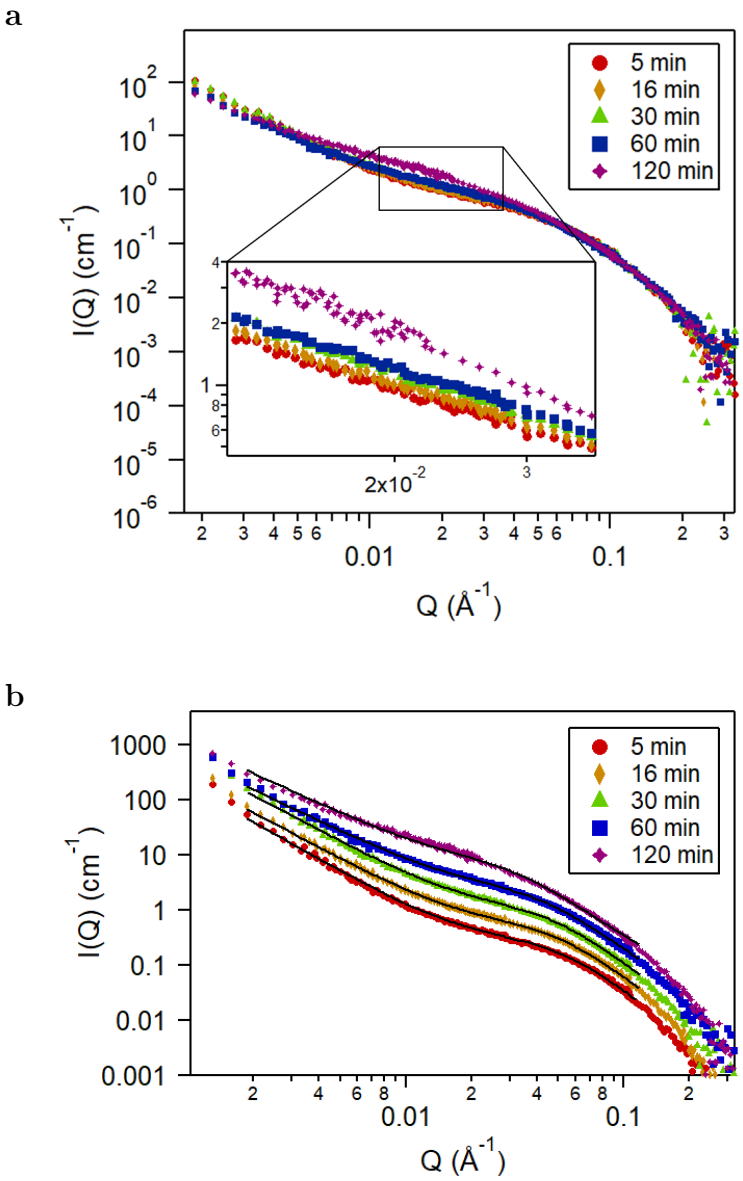

Figure 2.15: a) SANS spectra that have been normalized with incoherent backgrounds subtracted. Included is an inset showing mid-q evolution with increasing oxidation time. Curves shown shifted with fit curves of correlation length fitting. b) The same data have been plotted with an offset, so each curve is visible, along with lines obtained from fitting each data to the correlation length function.

between fibers. As this surface charge builds up, the distance between fibers begins to increase. The correlation length corresponds to a mesh size for the network of nanofibers within the macrofibers. A similar interpretation is given in Penttila et. al.,

Time (min)	5 min	15 min	30 min	60 min	120 min
A ($\times 10^{-5}$)	6.6	11.9	13.6	31.2	55.0
n	2.25	2.12	2.12	1.93	1.87
C	0.50	0.53	0.59	0.64	1.09
Length, ξ (Å)	18.83	19.67	20.94	22.88	29.68
m	3.3	3.3	3.3	3.3	3.3

Table 2.1: Fit parameters resulting from the correlation length fitting. A is the porod scale factor, n is the porod exponent, C is the Lorentzian scale factor, ξ is the correlation length, m is the Lorentzian exponent, and χ^2 is the estimate for goodness of fit.

in which the mesh size in cellulose nanofiber networks was shown to decrease during enzymatic hydrolysis, where the mesh size was again attributed to the correlation length [79]. This length does not, however, indicate a specific object size or distance, but the length is on the order of the diameter of individual nanofibers, and the increase indicates an increasing mesh size.

The χ^2 parameter is a measure of the goodness of fit, and is relatively constant until the 120 minute sample, when it increases dramatically. This is likely due to the variability in macrofiber size observed in optical microscopy. Just as swelling of the macrofibers leads to more variability in size and to a broader diameter distribution, the interfiber distances at 120 minutes are more variable, resulting in a broader shoulder in the scattering data that does not fit the correlation length equation as successfully. The Lorentzian slope, m, is fixed during fitting, and denotes the decay of the of the scattering at intermediate Q. The power law scale, A, increases slightly with oxidation time, where the power law exponent, n, decreases slightly. It is difficult to interpret variability of these parameters as there are only a few points

to fit this part of the data, as the power law scattering extends to much lower Q that is out of range of the instrument. The power law scattering is due to relatively large scattering objects, potentially the overall structure of larger scale cellulose fibers or nanofiber bundles. While the individual nanofibers have begun to separate due to the anionic charge groups introduced during the TEMPO oxidation reaction, the overall structure of the large-scale fibers is still present, and mechanical homogenization is required to fully separate the nanofibers.

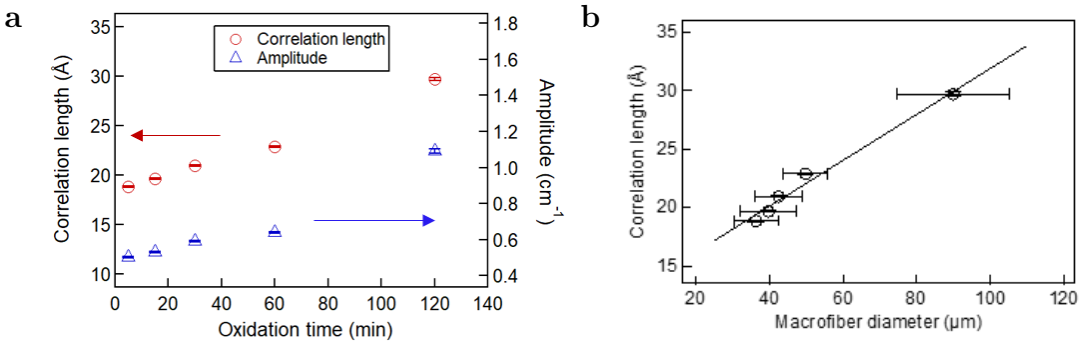

Figure 2.16: a) Correlation length and Lorentzian scalar values obtained from SANS plotted against oxidation reaction time. b) The large-scale macrofiber diameter obtained from optical microscopy plotted against the correlation length. A linear fit line is plotted with this data as well.

The correlation length is an indicator of the increase in interfibrillar distance within each sample. Using optical microscopy data, it has been shown that at large scales, this correlation length increase indicates swelling in the cellulose macrofibers. In Figure 2.16, the correlation length from SANS has been plotted against the macrofiber peak diameter from optical microscopy. There is a linear correlation of the two measurements consistent with the interpretation that the separation of the nanofibers with TEMPO oxidation leads to swelling of the macrofibers.

2.4.3 Mechanical Homogenization- AFM

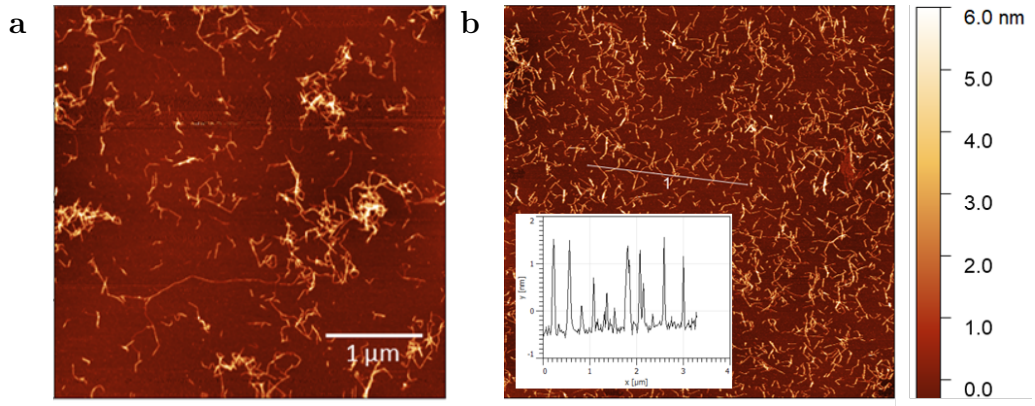

Figure 2.17: AFM images taken of diluted nanofiber samples from 1 pass (a) and 4 passes (b) through the microfluidizer. A line profile was drawn in figure b to illustrate the uniformity of nanofiber height in the 4 pass image. Most nanofiber heights fall between 1 and 2 nm.

CNF was prepared by homogenizing the 120-minute TEMPO-oxidized cellulose at different levels. Images were obtained of each sample displaying isolated fibers on a flat mica surface. AFM images of 1 and 4 pass CNF suspensions are shown in Figure 2.17a and 2.17b, respectively. In both samples, the heights of the CNF appear consistent, as evidenced by the line profile displayed in Figure 2.17b. Figure 2.18a shows nanofiber lengths of both 1 and 4 pass CNF, displaying considerable variability in the fiber lengths. Figure 2.18b shows diameters of both 1 and 4 pass CNF, with histograms appearing very similar.

Diameters of the nanofibers were estimated by measuring height using line profiles as shown in Figure 2.17b. For each sample, more than 300 nanofiber heights were measured to estimate the diameter, and the resulting data were plotted as histograms shown in Figures 2.18a and 2.18b. Histograms were fit to a lognormal

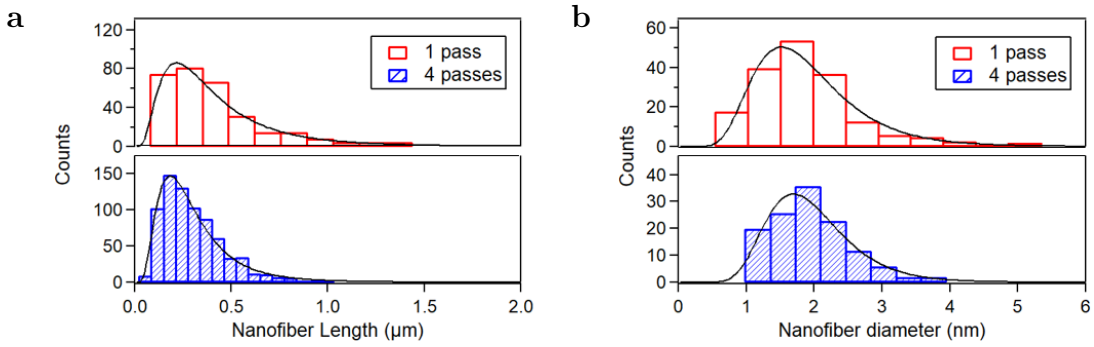

Figure 2.18: Histograms and corresponding log-normal fits for 1 and 4 pass length (a) and diameter (b) distributions. The length distribution of the 1 pass fibers have slightly longer lengths and a broader distribution than the 4 pass fibers. The diameter distributions appear almost identical.

distribution function, with mean and standard deviation calculated as determined by Equations 2.2, 2.3, 2.4 respectively, with the lognormal fitting plotted alongside the histograms. In Figure 2.18a, the length histogram of the 1 pass sample is broader and centered around a larger length than the 4-pass sample. In Figure 2.18b, the diameter histogram of the 1 pass data is comparably broad to the 4-pass data, and each histogram is centered at a similar diameter.

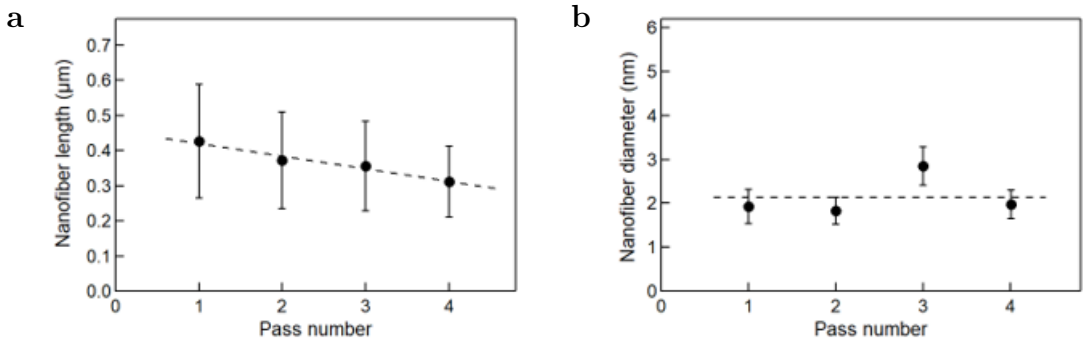

Figure 2.19: Mean nanofiber length (a) and diameter (b) as a function of the number of microfluidizer passes, with a line of best fit. Figure a illustrates the overall decrease in fiber length and distribution broadness with increased mechanical homogenization. Figure b shows how the diameter remains constant with increasing homogenization steps.

The mean and standard deviation for length and diameter of each sample are plotted in Figures 2.19a and 2.19b, respectively. The dotted line in Figure 2.19b is a line showing the average diameter of all samples, equaling a diameter of about 2.1 nm, with a small range of error. Length values shown in Figure 2.19a decrease with number of passes, with a dotted line of best fit shown between points. CNF prepared with 1 pass had a mean length of 428 $\pm$ 160 nm, while 4 passes had a mean length of 311 $\pm$ 100 nm.

With increased mechanical homogenization, the diameters do not decrease. The nanofiber length decreases with increased homogenization, and the length distributions also become narrower. This indicates that the forces generated from the high-pressure homogenization, reaching pressures of 30 kpsi, are sufficient to sever the length of the nanofibers, but not breaking the cellulose crystallite structure that makes up the nanofiber cross section. When incorporating the CNF into all-cellulose composites, a narrower distribution can lead to better quantification of the mechanical reinforcement effects within the composite, therefore CNF with 4 passes of homogenization were used to produce all cellulose composites.

2.5 Summary

The structural evolution of cellulose throughout the TEMPO oxidation process was investigated. A typical oxidation reaction takes 120 minutes, so the cellulose structure was investigated throughout the length of the reaction. Using optical microscopy, swelling of large-scale cellulose macrofibers was observed, from roughly

36 μm at 5 min to 89 μm at 120 min. The internal nanostructure of the cellulose macrofibers was probed using SANS, in which a scattering correlation was observed corresponding to the elementary interfiber distance that increased from 19 Å at 5 min to 30 Å at 120 min. While this correlation does not directly correspond to a physical length scale within the cellulose, the increasing correlation length indicates a qualitative increase in interfiber distance. There is a linear correlation between macrofiber diameters, indicating that the increase in interfiber distance at the nanoscale is a possible mechanism for the macro-scale swelling observed using optical microscopy, as illustrated in the schematic shown in Figure 2.20.

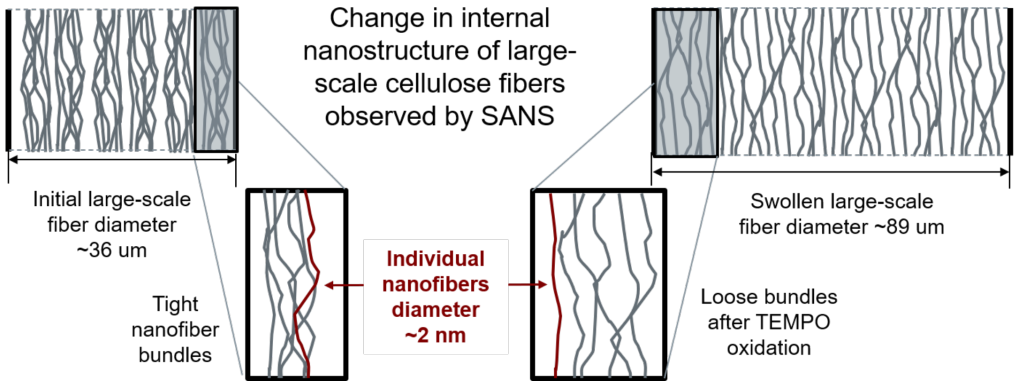

Figure 2.20: Schematic illustrating the hierarchical structure present within large-scale cellulose fibers. Cellulose nanofibers are aligned into bundles, which are arranged within the cell wall within the large-scale fibers. During the TEMPO-oxidation reaction, repulsive charges cause separation between nanofibers, resulting in swelling in the large-scale macrofibers.

Considerable work has gone into studying the mechanical fibrillation of cellulose nanofibers. With the advent of the TEMPO oxidation reaction as a chemical pretreatment, CNF can be obtained with minimal mechanical fibrillation, resulting in fully separated elementary nanofibers. While the structure of the CNF has previously been characterized, this work has investigated the intermediate chemical pretreatment

process of the cellulose before mechanical fibrillation, and how this process affects the overall cellulose structure. While the carboxylation of cellulose has been shown to allow for full separation of CNF after mechanical pretreatment, this work shows that it also results in a physical change in the swelling of cellulose macrofibers due to a change in interfiber distance at the nanoscale, providing new insight on how the separation of CNF is understood.

Chapter 3: Molecular cellulose solutions

3.1 Introduction

This chapter discusses the dissolution of cellulose with a binary solvent of ionic liquid and polar aprotic solvent, referred to here as a MCS. The background material will discuss previously employed methods of dissolving cellulose, which can mostly be separated into 3 categories: chemical modification or derivatization, aqueous or protic systems, or non-aqueous and non-derivatizing direct solvent dissolution. Additional methods of processing cellulose will also be discussed including the Lyocell method, mercerization, and an alkali-urea system. A summary of ionic liquid processing of cellulose will be discussed as well, to inform the work on MCS.

MCS is a fully dissolved solution of cellulose, achieved with minimal heating and no apparent aggregation. The research conducted regarding MCS will start with phase behavior and overall scattering behavior as a function of temperature. Neat cellulose films can be produced from MCS by first evaporating the cosolvent, dimethylsulfoxide (DMSO), resulting in a dense gel of cellulose and ionic liquid. The ionic liquid can be removed through a multi-step soaking process using acetone and ethanol. The structure of these gels was studied by small- and wide-angle x-ray scattering and rheology, revealing a unique structure present in the films that is

dependent on ionic liquid composition. The evolution of this structure was studied throughout the ionic liquid removal process as well. A model has been proposed to describe and understand this structure.

3.2 Background

3.2.1 Dissolving cellulose

Cellulose is the most abundant naturally occurring polymer on earth and has been a material in use throughout human history in applications such as paper and fabrics. However, cellulose also has a significant history in the field of polymer science. The first man-made fibers were of Chardonnet silk, introduced in the late 19th century. This silk was the first type of rayon, a manufactured textile product derived from cellulose that has been regenerated into a fiber. This type of fiber is referred to as semi-synthetic, as the long-chain polymer structure of cellulose is provided by plants naturally and is only partially degraded in the fabrication process. These rayon, or Chardonnet silk, fibers were developed as an alternative to conventional silks, and by the early 20th century became a significant facet of the textile market [80].

The first rayon fibers were discovered by treating cellulose with sulfuric and nitric acid to produce a cellulose derivative called cellulose nitrate in 1846. The introduction of the nitrate ($-ONO_2$) groups allowed separation between adjacent cellulose chains, allowing solubility in common solvents and reducing crystallinity. Cellulose nitrate could then be regenerated into cellulose by extruding thin fibers,

allowing the solvent to evaporate, and removing the nitrate groups with a hydrolysis and sodium hydrodisulfide treatment. This same process used to produce cellulose nitrate was employed to fabricate the first man-made polymers, such as celluloid which was commonly used in early film production [81].

An additional method of preparing rayon cellulose fibers was developed called the cuprammonium process, which became preferred to the Chardonnet method due to its lower cost. This process involved dissolving cellulose in an ammonium-based copper(II) hydroxide solution. The solution is extruded through thin spinnerets or nozzles, and into a dilute sulfuric acid solution in which the cellulose is regenerated, then washed with acetic acid.

A third type of rayon fibers are known as viscose fibers. This process employs a derivative of cellulose called cellulose xanthate, produced from a reaction between carbon disulfide and alkaline cellulose. The cellulose is then regenerated in a dilute sodium hydroxide solution. This process has been optimized and industrialized to be cheaper and more efficient than cuprammonium when manufactured at a large scale, and currently the viscose method accounts for most of the total rayon production in the world. Due to the many mechanical steps employed throughout production, significant versatility in properties of the final product can be achieved, however this means the process must be very carefully controlled in order to obtain reproduceable fibers [80].

Rayon fiber production found extensive use in the textile industry and was originally implemented at a large scale in the United States, but has been less frequently used in recent years as a result of the hazardous nature of the process.

The process uses a large amount of water, and production is energy intensive. The reactants used can all be considered toxic and can be hazardous for workers. The waste products and emissions from this reaction are harmful to the environment, such as sulfur, carbon disulfide and hydrogen disulfide. While the process can be described as sustainable, since the raw cellulose material is derived from plants instead of from petroleum like synthetic textile materials [80], the chemical modification and processing of cellulose are still hazardous to the environment, so it is difficult to rationalize cuprammonium or viscose rayon as a sustainable textile material. In fact, rayon can no longer be manufactured in the US due to producers not being able to meet air and water-quality regulations [82, 83]. Currently, viscose rayon is primarily produced in China, where environmental regulations are laxer [84].

The hazardous nature of the cupramonnium and viscose rayon production has resulted in a demand for a more environmentally friendly manufacturing pathway for sustainable cellulose-derived fibers. One such method called the Lyocell process employs the solvent N-methylmorpholine N-oxide (NMMO) and water, which can directly dissolve cellulose without any prior treatment or derivatization of cellulose, such as cellulose xanthate or cellulose nitrate that are employed in rayon production. Since this is a direct-dissolution process, there are far fewer steps than a derivatized cellulose process like the production of viscose. Cellulose pulp is dissolved, then the solution is spun, washed, dried, and dyed. The NMMO is recyclable throughout this process, which is not the case for all reactants in the viscose process. (Rosenau, 2001) NMMO also exhibits low toxicity, is biodegradable, has a high recovery rate at >99%. NMMO is currently employed at an industrial scale in the US to produce

regenerated cellulose fibers for textile applications [85].

NMMO can disrupt the hydrogen bonding within cellulose, first dissolving the amorphous regions and forming complexes with the hydroxyl groups, then gradually breaking down crystalline regions [83]. Additionally, the crystal structure of cellulose during the Lyocell process has been shown to change from cellulose I to cellulose II, which can improve the ability of the cellulose to be dyed, an advantage in textile processing [22].

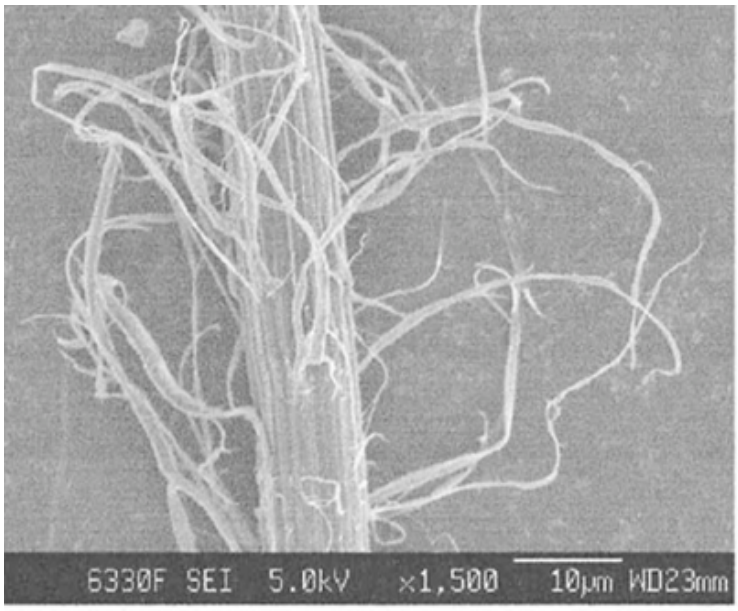

Figure 3.1: SEM Image showing fibrillation of a Lyocell fiber [86]. © 2003

However, NMMO is more likely to form hydrogen bonds with water instead of cellulose. Certain hydrates of NMMO require high temperatures for cellulose dissolution that would cause degradation, so the amount of water needs to be carefully controlled. NMMO also requires an antioxidant stabilizer to prevent explosion during transport and storage. Additionally, Lyocell fibers tend to fibrillate depending on how carefully the spinning process is controlled, which can negatively affect the

resulting mechanical properties and structural integrity. This fibrillation is shown in Figure 3.1 [83, 85, 87, 88].

The transition of the crystal structure from cellulose I to cellulose II is desirable in many cellulose applications in textiles for aesthetic reasons. One common method of converting cellulose I to cellulose II is a process known as mercerization, in which cellulose is subjected to strong alkali conditions. Mercerized fibers have a noticeably improved luster and are more water absorbent so they can absorb more dye than unmercerized fibers. However, mercerization does not fully dissolve cellulose, it merely results in the transition to cellulose II. Chains within nanofibers change conformation from parallel to antiparallel packing, but the overall nanofiber structure remains intact [18].

A similar solvent system has been shown to rapidly and directly dissolve cellulose by using an alkali (including both $NaOH$ and lithium hydroxide ($LiOH$)) and urea-based solvent. Typically processes for dissolving cellulose require long time scales, however this solvent will dissolve cellulose within 2 minutes. Interestingly, this solvent will only dissolve cellulose at low temperatures. The mechanism for this solvent system relies on the formation of clusters of $NaOH$, urea, and water. The $NaOH$ and urea form "hydrate" clusters with water molecules. As the temperature decreases, the formation of solvent clusters increases. The low-temperature rapid dissolution of cellulose in this system is an entropy driven process, in which cellulose chain rearrangement is driven by entropy competition between conformational entropy of cellulose and translational entropy of alkali and urea hydrates. The alkali clusters break apart cellulose chain packing by disrupting intra and intermolecular hydrogen

bonds. The urea hydrates play a role by forming an inclusion complex around the cellulose chains and alkali-hydrates, this keeps the chain complexes separated and prevents cellulose aggregation, allowing for full dissolution [89, 90].

3.2.2 Cellulose dissolution in ionic liquids

The excessive use of volatile solvents is damaging to the environment through large volume production, disposal, or ozone depletion potential, and can present health hazards to workers frequently exposed to evaporating solvents. As a result, considerable effort has gone into defining parameters for green solvents, such as production from renewable sources, improved biodegradability, or low volatility. Recently, ionic liquids (ILs) have shown promise as a green solvent, in particular due to their low volatility, in many applications in chemical synthesis, catalysis and solvation [91]. IL also have good thermal and chemical stability, can be recyclable in certain applications, and have a low melting temperature (below 100 °C), making them an ideal candidate for a green chemical solvent [92].

There are particular ILs that are ideal for dissolving cellulose, depending on the anion and cation chosen. It is widely accepted that anions that are good hydrogen bond acceptors, such as acetate, formate, or chloride, are effective at dissolving cellulose [93]. It is estimated that the higher the hydrogen bond basicity and dipolarity, the greater the ability to dissolve cellulose [94]. The role played by the anion during dissolution of cellulose is penetrating the overall crystalline and hierarchical cellulose structure and disrupting interchain hydrogen bonding [95].

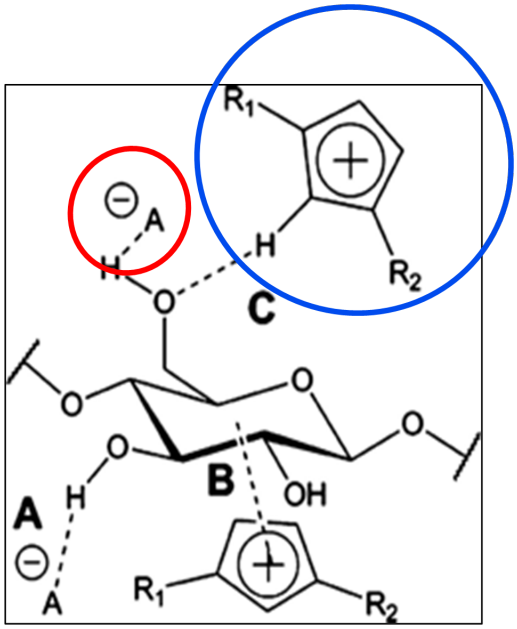

Figure 3.2: EMIMAc interacting with cellulose repeat unit. Acetate anion, circled in red, bonding with the hydrogen atom of the hydroxyl group. Imidazolium cation, circled in blue, bonding with the oxygen atom on the hydroxyl group [96]. © 2015

The role of the cation in the IL is not as clear and has been the subject of much debate in the literature. ILs that are capable of dissolving cellulose have been shown to contain one of the following cations when paired with an anion with a strong hydrogen bond basicity: imidazolium, pyridinium, ammonium, and phosphonium. Of these, imidazolium and pyridinium have been most effective. In understanding the role of the cation, an ionic liquid 1-ethyl-3-methylimidazolium chloride (EMIMCl) was studied, having an imidazolium cation and a chloride anion. It was shown by nuclear magnetic resonance (NMR) measurements that no specific interaction existed between the cation and the cellulose, and the dissolution appeared to be purely the result of the anion interactions. However, when the ionic liquid EMIMAc, having an acetate instead of chloride anion, was studied, NMR data revealed an interaction between the oxygen of the cellulose hydroxyl groups and the acidic protons in the

imidazolium cation. This could be due to a weaker interaction between the anion and cation within EMIMAc, allowing the cation to interact with the cellulose as well [97]. Figure 3.2 shows an example of the proposed interaction between the anion and cation of EMIMAc and a cellobiose molecule, resulting in cellulose dissolution [96].

Zavrel et. al. reports the dissolution of cellulose in EMIMAc within 20 minutes as shown using in situ optical microscopy (shown in Figure 3.3). The experiment had 1% by weight of Avicel microcrystalline cellulose powder dissolved in EMIMAc at about 30 °C while images were taken. By roughly 20 minutes the large powder particles can no longer be observed, and the cellulose appears to be mostly dissolved without added agitation [98].

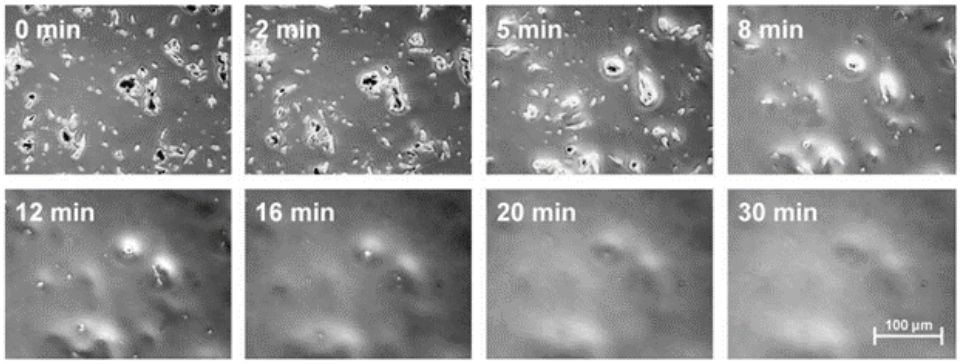

Figure 3.3: *In situ* optical microscopy images of microcrystalline cellulose powder dissolving in EMIMAc [98]. © 2009

Once the cellulose is dissolved, regenerating cellulose from solution is a crucial step in evaluating the efficacy of ionic liquids as a solvent. To regenerate cellulose from ionic liquid solutions, a nonsolvent, or coagulant such as water, acetone, ethanol, methanol, acetonitrile, etc. is used. The resulting morphology and microstructure of the cellulose will vary depending on the regeneration solvent used and the method of regeneration. For example, rapid and immediate mixing of the solution with

a nonsolvent causes cellulose to flocculate, resulting in large powder-like particles. Extrusion into a nonsolvent bath can result in thin fibers or rods, casting onto a flat surface and washing with nonsolvent will result in a film, and aerogels can be prepared by washing and drying under supercritical conditions [99].

After dissolving and reconstituting, the resulting cellulose tends to have a lower degree of crystallinity than the starting cellulose material, and the regenerated cellulose also changes from a cellulose I structure to cellulose II, similar to other cellulose processing such as mercerization.

3.3 Molecular cellulose solutions with aprotic solvents

While ILs have been shown to be effective and green solvents for dissolving cellulose, they still face a number of obstacles. ILs are highly viscous, which results in thick solutions that can require excessive mechanical agitation and higher temperatures to effectively break down cellulose, particularly when dissolving at higher concentrations. ILs are also expensive, and while they have been shown to be partially recyclable, more work is needed to limit the amount of IL used in cellulose dissolution [100]. Additionally, while EMIMAc can effectively break down cellulose, aggregation is still present in solution. Light scattering studies indicate that aggregates with a radius of gyration up to 150 nm are still present in solutions of cellulose in EMIMAc, a size much larger than a single cellulose macromolecule [101].

In work done by Rein et al., a binary solvent mixture using IL and various polar aprotic cosolvents was studied, claiming to create a true molecular solution

of cellulose [100]. This system, particularly with dimethylformamide (DMF) and DMSO as cosolvents, was shown to effectively dissolve cellulose, with no remaining aggregates. Figure 3.4 shows SANS data obtained by Rein et al. of a 4 wt% cellulose solution with a 9:1 DMF to EMIMAc ratio solvent. In this data the lack of excess scattering at low Q indicates no significant aggregation of cellulose in the solution [100].

Adding a cosolvent to cellulose and ionic liquid solutions can reduce the viscosity, speed up the dissolution process, and more effectively dissolve cellulose. This work details the investigation of the phase behavior of this cellulose solution, including its dependence on composition and temperature, the structure within the solutions investigated by SANS, and the effect that water has on the solution. Understanding the compositional limits of this ternary solution system can expand the knowledge of the structure and thermodynamics of true molecular level solutions.

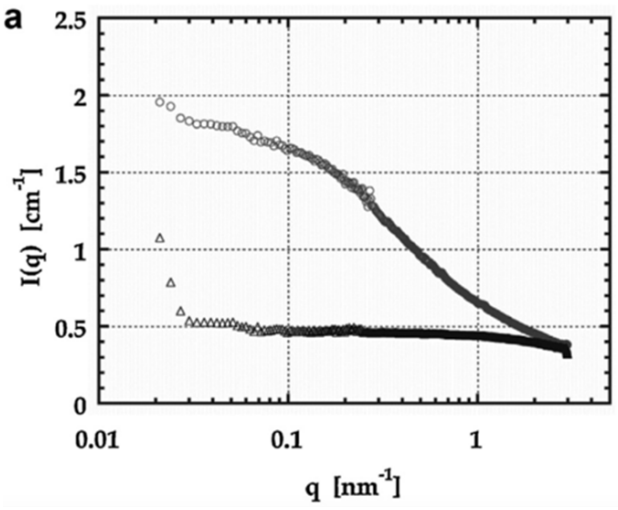

Figure 3.4: SANS data for 4 wt% solution of cellulose in a 9:1 DMF to EMIMAc binary solvent mixture. Circles- scattering from the solution; triangles- scattering just from the 9:1 DMF to EMIMAc binary solvent mixture. [100] © 2014

Understanding the behavior of this and similar solutions is crucial for its potential use for cellulose dissolution and regeneration. In this work, cellulose solutions in EMIMAc and DMSO or DMF have been studied using SANS to observe the presence or absence of aggregates in solution in order to understand chain conformation and phase diagram behavior.

3.3.1 Experimental methods

Avicel PH101 cellulose powder is purified cellulose with a degree of polymerization of the average number of AGU, DP $\approx$ 250, and was purchased from Sigma Aldrich. EMIMAc (95% purity) was also purchased from Sigma Aldrich and was stored in a dry glove box to minimize moisture content along with the Avicel cellulose. DMSO was stored containing molecular sieves to remove water, then was filtered before use. Deuterated DMSO (dDMSO) was stored in sealed glass vials in a dry glovebox before use and was purchased from Cambridge Isotopes. Solutions were prepared over a wide range of cellulose, dDMSO, and EMIMAc compositions by weighing out a mass of cellulose, then stirring with a specified mass of dDMSO and sealing in a vial. To avoid exposure to moisture, as all components are hygroscopic, EMIMAc is added with a syringe through a seal in the top of the vial. The mixture undergoes mechanical agitation and heating to 90 °C until the cellulose dissolves and the solution becomes transparent. Samples that dissolved would become clear within a few minutes. Some solutions were prepared to intentionally include water (D_2O for SANS measurements), in order to investigate the effect of moisture on the solvation

capabilities of the system. In this case, set amounts of D_2O were added to dDMSO, and this mixture was added to the cellulose before being mixed with EMIMAc.

3.3.1.1 Small angle neutron scattering

SANS measurements were carried out at the National Institute for Standards and Technology (NIST) Center for Neutron Research (NCNR) at the NIST, Gaithersburg, Maryland. Typical SANS spectra were obtained with a neutron wavelength, $\lambda \approx 6$ Å , and a wavelength spread of $\Delta\lambda/\lambda \approx 0.12$. The instrument configurations of 13, 4, and 1 m sample-to-detector distance were used to collect scattering data spanning a Q range between 0.003 $Å^{-1}$ to 0.5 $Å^{-1}$ [33]. Data reduction was conducted using Igor Pro 6 and the NCNR Reduction Macros [77].

3.3.2 Results and discussion

3.3.2.1 Phase diagrams

Solutions were prepared at a wide range of concentrations to determine the phase behavior and compositional limits of this system. Based on the behavior of the scattering in the mid- to low-Q regime, particularly between 0.01 $Å^{-1} < Q < 0.1$ $Å^{-1}$, a determination was made based as to whether the sample was fully dissolved. For dissolved samples, the scattering in the given Q range was mostly flat, with the intensity only slightly larger than the incoherent background and is typically between 0.3 $cm^{-1} < I(Q) < 0.8$ cm^{-1}. Undissolved or aggregated samples displayed significantly higher intensities within the given Q range, and showed a prominent

shoulder indicating monostructure formation and/or aggregates. SANS data from the samples tended to exhibit one of three behaviors, which were used to construct a phase diagram: (1) the solution is fully dissolved at room temperature (roughly 20 °C), labeled in green on the phase diagram; (2) the solution is aggregated at room temperature but dissolved upon heating to 100 °C, then upon cooling a full or partial reaggregation is observed, labelled in orange; (3) the solution is not dissolved at room temperature and remains undissolved upon heating, labelled in red. Solutions containing added D_2O are labelled with a solid circle symbol, while solutions with no added D_2O are labelled with hollow circles.

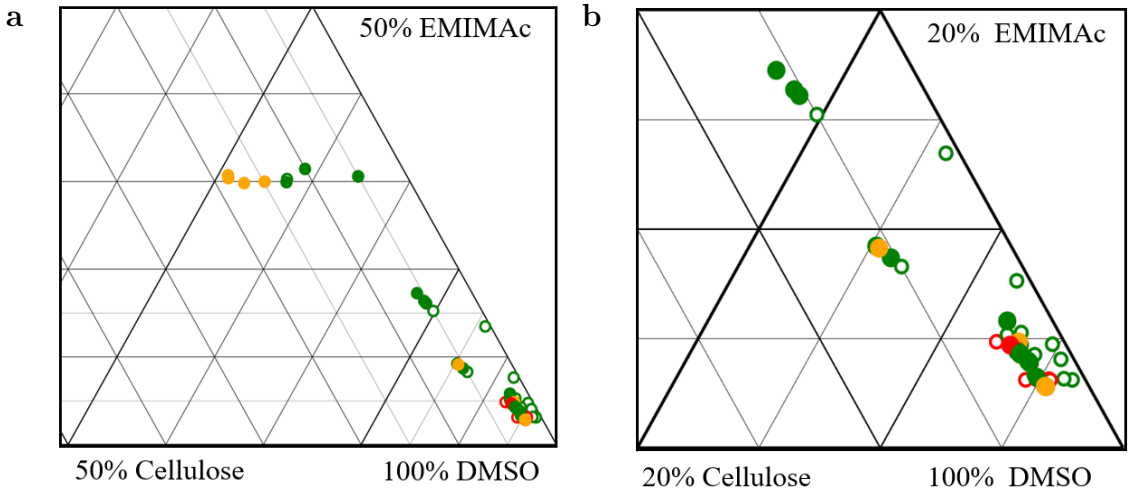

Figure 3.5: Ternary phase diagram showing the relative compositions of EMIMAc, cellulose, and DMSO. a) Shows the lower right corner of the overall diagram, containing the DMSO-rich region within 50% cellulose and EMIMAc. b) Shows a smaller section for ease of visualization within 20% cellulose and EMIMAc in the solvent-rich region. Red samples do not dissolve at all. Orange samples dissolve at high temperature and reaggregate upon cooling. Green samples remain dissolved upon cooling.

Two ternary phase diagrams were constructed to visualize the phase behavior of the system with and without the effect of water. Since there are 4 components in

the system (Cellulose, EMIMAc, dDMSO, and D_2O) the relative compositions of 3 components will be displayed on each diagram. The first diagram for example, shown in figure 3.5a, shows the relative compositions of cellulose, EMIMAc, and DMSO. In this case the position on the diagram is calculated based on the relative molar amounts of these three components, and the composition of water is not included. For example, if a solution contained equal parts of all four components, cellulose, EMIMAc, D_2O, and dDMSO (i.e., 25% of each), this diagram would display the solution compositions with D_2O removed, so each of cellulose, EMIMAc, and dDMSO would be displayed at 33%. Essentially, the phase diagrams shown in Figures 3.5 and 3.6 is a single face on a pyramid shaped quaternary phase diagram including all four components.

Since EMIMAc is the primary cellulose solvent, the most significant comparison will be between cellulose and EMIMAc compositions. While the lowest EMIMAc to cellulose ratio achieved for dissolution in the literature is roughly 3:1, [99, 102] in this work a ratio as low as 1.66:1 was achieved. Therefore using DMSO as a cosolvent can dramatically reduce the amount of EMIMAc necessary for dissolving cellulose. The DMSO concentration in the solutions is important for determining its flexibility as a cosolvent. DMSO shows that even at high rates of dilution the solution will remain dissolved at the same ratios of cellulose to EMIMAc, whereas for other investigated cosolvents, such as DMF, dilution is only possible up to a point at which the solvent is about 5 mol% in DMF [103]. At higher cellulose concentrations, however a higher ratio is typically required. For example at about 15 mol% cellulose, a ratio of about 2:1 is not sufficient to dissolve cellulose, so cellulose concentration plays a role as

well.

The same set of samples were plotted on a phase diagram displaying the relative compositions of cellulose, EMIMAc, and D_2O, shown in Figure 3.6. The hollow circle symbols, indicating samples containing no added water, are displayed purely along the cellulose-EMIMAc axis, which helps to visualize the ratio between these two components. In this diagram EMIMAc to cellulose ratio is still a significant determining factor, despite a significant D_2O composition.

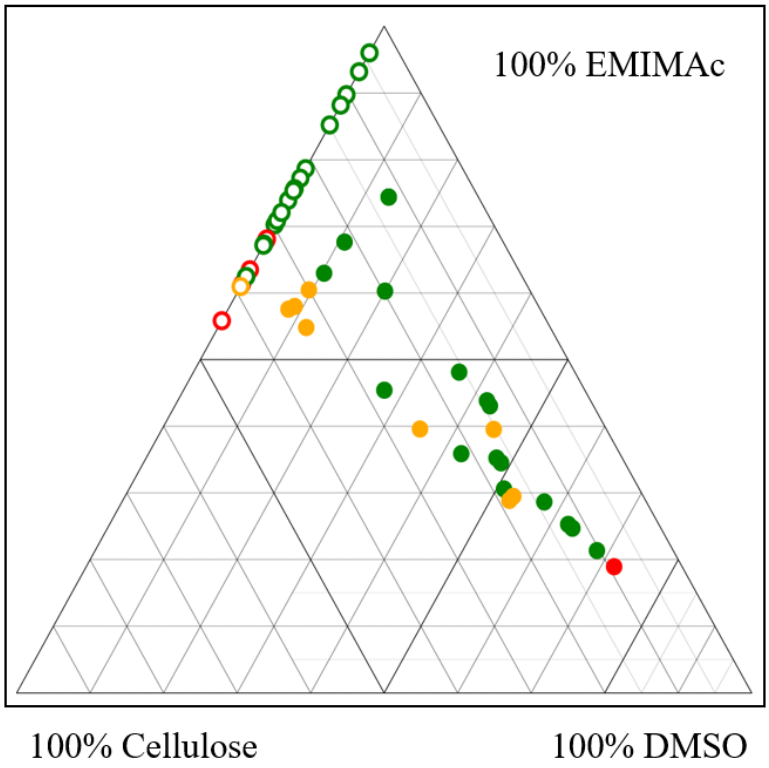

Figure 3.6: Ternary phase diagram featuring the relative compositions of cellulose, EMIMAc, and D_2O.

Water was initially anticipated to play a key role in determining whether cellulose would be soluble in the blend of EMIMAc and DMSO. In work done by Kuzmina et. al. the effect of water on cellulose solubility in ionic liquids (with no

cosolvent) was investigated. As previously mentioned, aggregates of cellulose are still present when dissolved in only ionic liquid. With the introduction of water, upon increasing the water content the size of these aggregates was shown to increase, though it was not known if this was due to aggregate swelling in water or the efficacy of ionic liquid as a solvent diminishing due to the presence of water [101]. However, the data shown in the phase diagram in figure 3.6 indicates that introducing water into the solution does not necessarily diminish, as the EMIMAc to cellulose ratio necessarily for dissolution is maintained with increasing water content.

This does not necessarily mean that water has no effect on the components of this solvent system. The dissolution process is pathway dependent, if water is introduced with cellulose instead of with DMSO, the cellulose will not dissolve properly, if at all. The cellulose can become kinetically trapped in a low energy aggregated state due to the presence of water, making it difficult to dissolve and requiring excessive ionic liquid, heating, and mixing. Previous work has also shown that using water as a cosolvent in a cellulose and ionic liquid solution without DMSO results in a very limited solubility window, so water can inhibit the efficacy of EMIMAc as a cellulose solvent [104]. However, because water is added at the same time as DMSO, and DMSO has also been shown to interact with water at the molecular level [105], it is reasonable to assume that this lessens the interaction between water and EMIMAc, which can allow cellulose to be dissolved despite relatively high water content. Additionally, samples containing water exhibit a much higher viscosity than those with a similar cellulose concentration, ultimately leading to a gel-like behavior. It is likely that water can cause bridging or local aggregation of

cellulose molecular chains, which can explain the increase in viscosity in the solutions. Despite the fact that the inclusion of water does not appear to inhibit EMIMAc as a cellulose solvent, this gelation and overall higher viscosity can make these solutions more difficult to dissolve, requiring more stirring and heating.

3.3.2.2 Small angle neutron scattering results

The SANS spectra of each sample were used as a form of cloud point measurement to evaluate the state of solvation. Spectra of samples that were fully dissolved displayed curves with flat scattering in the mid- to low-Q regions of low relative intensities between 0.3 cm^{-1} < I(Q) < 0.8 cm^{-1}, some with small upturns at very low Q likely due to dust or contamination. Spectra featuring aggregated or undissolved samples feature curves with significantly higher intensities and a shoulder in the mid-Q region.

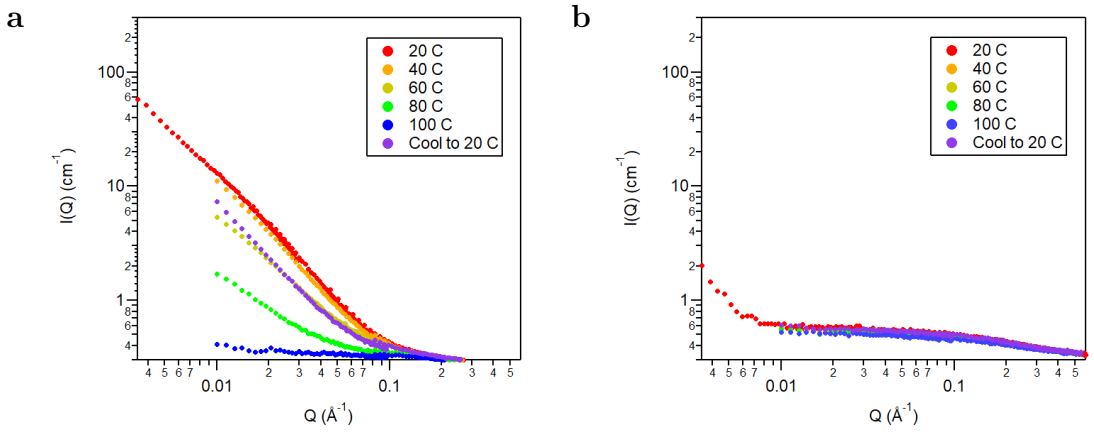

Figure 3.7: SANS spectra with variable temperature of two MCS solution samples. a) Solution with an EMIMAc to cellulose ratio of roughly 1.67:1. This sample is aggregated at room temperature but dissolves at high temperature. b) Solution well within the solubility region having an EMIMAc to cellulose ratio of roughly 3:1 and being fully dissolved at room temperature.

Figure 3.7a shows a sample that is aggregated at room temperature with an EMIMAc to cellulose ratio of about 1.7:1. At room temperature, there is a prominent shoulder observed in the mid-Q region with relatively high intensity, indicating aggregation in the sample. Upon heating the intensity starts decreasing beginning between 40 and 60 °C, then becomes flat scattering between 80 and 100 °C, indicating that the cellulose aggregates have fully dissolved. When the sample is cooled back down to 20 °C, the intensity increases, almost returning to its initial high intensity after one hour of equilibration time. Figure 3.7b shows a fully dissolved sample at room temperature, which upon heating exhibits near identical scattering behavior, showing minimal scattering at low-Q. The scattering behavior of the sample shown in Figure 3.7b is remarkably similar to the flat scattering observed in the 100 °C scattering shown in Figure 3.7a, indicating that both are representations of solution scattering for MCS.

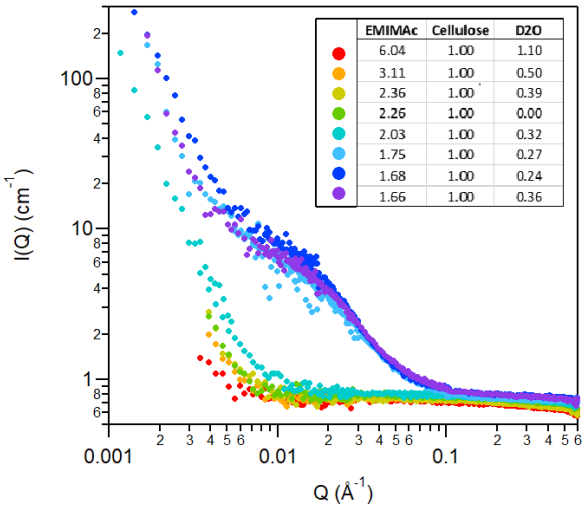

Figure 3.8: SANS spectra of a sample series plotted with decreasing ratios of EMIMAc to cellulose. The relative amounts of D_2O are also variable but are not plotted in that order.

One series of samples was run varying the ratio of EMIMAc:Cellulose:D_2O, and is shown in Figure 3.8. The scattering curves are shown for varying EMIMAc:Cellulose ratio, starting at 2.03:1, and a slight change in intensity can be observed. Between 2.03 and 1.75, the samples become aggregated, displaying high low-Q intensity and a similar nanostructure present in the mid-Q region observed previously in Figure 3.8. The D_2O content, however, does not appear to affect the solubility of the solutions, because water content decreases as the samples begin to show aggregation. Figure 3.9 shows the aggregated samples, having EMIMAc to cellulose ratios of 2.03 (red), 1.68 (blue), and 1.66:1 (green), from Figure 3.8 heated and then cooled back to room temperature. For each of the two most aggregated samples (blue and green), the aggregation fully dissolves upon heating to 100 °C, then reforms at a slightly lower intensity upon cooling to room temperature. The observation that the aggregation reforms upon cooling indicates a lack of solubility for the samples at about a 1.7:1 EMIMAc to cellulose ratio. Since they can dissolve at high temperature but reaggregate upon cooling, this indicates a region of partial solubility that is limited by temperature.

The sample with EMIMAc to cellulose ratio of 2.03:1 shows a slight decrease in intensity upon heating, then after cooling the intensity does not increase again, indicating full dissolution. Additionally, in the two aggregated samples, the water content is 50% higher in the sample containing 1.66:1 EMIMAc to cellulose than in the 1.68:1 sample, but the scattering behavior is roughly the same at all temperatures. Therefore, this significant change in water content does not appear to have an impact on whether aggregation does or does not reform upon cooling after being fully

dissolved.

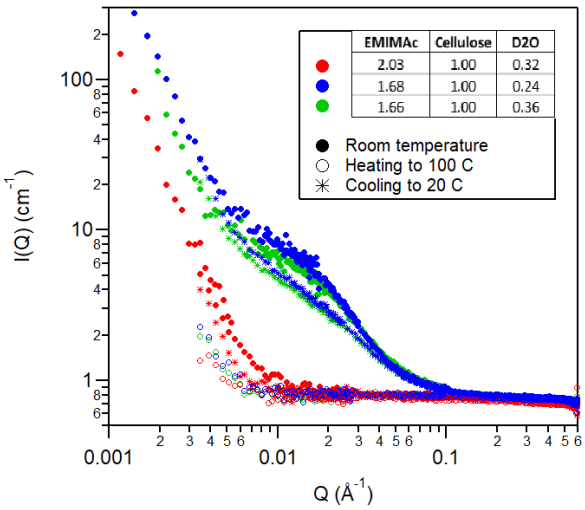

Figure 3.9: SANS spectra of 3 samples, two of which (blue and green) have aggregated at room temperature, one (red) is fully dissolved. Plot also shows spectra from heating each sample to 100 °C, and cooling to room temperature.

In Figures 3.8 and 3.9, a slight decrease in intensity is observed after heat cycling the aggregated samples with an EMIMAc to cellulose ratio of 1.68 and 1.66:1, which could either indicate an irreversible change in the sample after heat cycling or could indicate that the samples require longer than one hour to fully equilibrate and recover the original aggregated structure. Figure 3.10a shows a heat cycle of a sample labelled orange on the previously shown phase diagrams, indicating it is dissolved at high temperatures and reaggregates upon cooling to room temperature. As before, we also observe decreases in intensity at 50 and 80 °C, with flat scattering being reached between 80 and 100 °C. Figures 3.10a and 3.10b show two heat cycles of an aggregated sample. After the first heat cycle, a similar drop in intensity to what was observed in figures 3.8 and 3.9 is again observed upon cooling.

To determine the reversibility of this transition, this sample was heat-cycled one

additional time, the scattering results of which are shown in figure 3.10b. Again, the scattering intensity of the shoulder associated with the aggregation begins reducing in intensity as temperature increases. When the sample is cycled again the intensity at the mid-Q remains constant upon cooling. The initial drop in intensity from the first heat cycle is likely observed because the sample has not had adequate time to fully equilibrate, which explains why an additional drop in intensity is not observed after the second heat cycle. Therefore, after identical heat-cycle protocols, the scattering behavior of the sample remains the same. This indicates that the dissolution process for these aggregated samples is reversible.

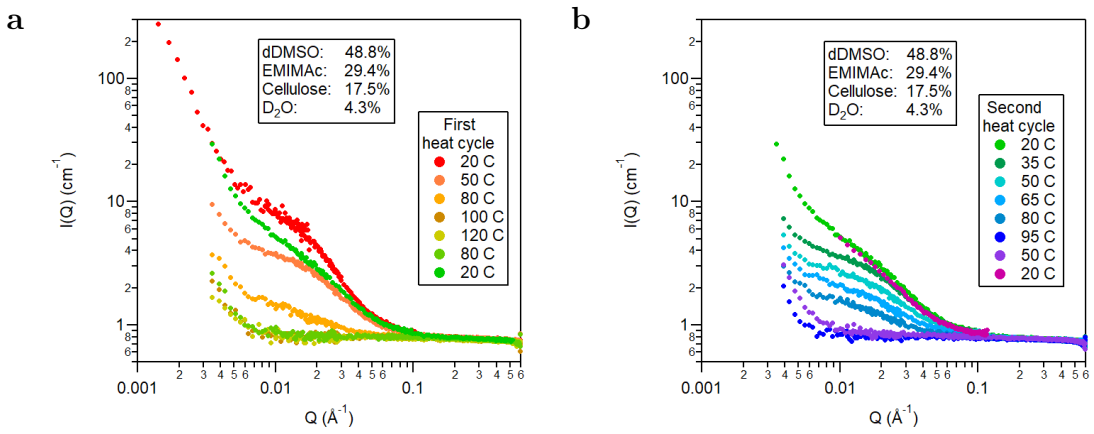

Figure 3.10: SANS spectra of a sample on the a) first heat cycle (20 °C to 120 °C), and b) second heat cycle (20 °C to 95 °C).

3.3.3 Conclusions

Solutions of cellulose fabricated from DMSO, D_2O, and EMIMAc were investigated. Using temperature-controlled SANS measurements, the phase behavior of the solutions was investigated, with the lowest achieved EMIMAc to cellulose ratio for

dissolution being 1.66:1. This is the lowest observed EMIMAc to cellulose ratio observed thus far, as the lowest recorded ratio in the literature is roughly 3:1. This low EMIMAc ratio is attributed to precise humidity control during sample preparation, and refined protocol for mixing and dissolving the solution, as introducing moisture at the incorrect stage in the dissolution process can hinder cellulose solubility.

The effect of water, which has been previously shown to limit the solubility of cellulose in EMIMAc substantially, was also investigated. It was shown that introducing water into the solution along with DMSO allows the cellulose to be dissolved at ratios as low as 1.66:1 without inhibiting the potency of EMIMAc as a solvent. Solutions containing water tended to form a more gel-like structure and have much higher viscosity, which made the solutions more difficult to dissolve, but ultimately did not change the minimum required EMIMAc to cellulose ratio for dissolution. This indicates that so long as water is introduced into the solution along with DMSO and the humidity and moisture content of the other solution components is carefully controlled, water will not affect the solubility of cellulose in EMIMAc. This could be a result of the interaction between water and DMSO, since if water were to be introduced into the solution individually, it would cause the cellulose to precipitate and prevent a solution from forming. However, if the water is introduced with DMSO, a molecular solution can still be obtained.

The ability to dissolve cellulose with as low an EMIMAc ratio as 1.66:1 significantly reduces the EMIMAc needed for dissolution. As EMIMAc is a relatively expensive component, this work makes it more economically viable as a cellulose solvent. Additionally, it has been shown that using the EMIMAc/DMSO binary

solvent system results in a true molecular solution of cellulose, as shown by SANS, which dissolves relatively quickly and with minimal heating required. The remainder of this chapter will discuss the process for casting and reclaiming cellulose films from solution, as well as the structural evolution of the cellulose throughout this process.

3.4 Concentrated gels of cellulose and ionic liquid

To obtain cellulose films from MCS, DMSO is evaporated from the ternary solution a vacuum oven, leaving a transparent, concentrated gel of cellulose and ionic liquid. In order to fully understand the structure of cellulose films cast from MCS, this intermediate gel structure needs to be studied. Because the DMSO in the MCS allows for such low EMIMAc to cellulose ratios, the resulting gels can contain much higher cellulose concentrations than previously reported in the literature. For example, in this work MCS is fabricated with 3.4% cellulose, 6.0% EMIMAc, and 90.6% DMSO by molar percentage, and because of the relatively low cellulose concentration it is not difficult to mix and will dissolve within a few minutes of heating and stirring. The solution is cast into a dish and DMSO is evaporated in a vacuum oven. The resulting gel will be roughly 38 mol% cellulose (30 vol%) in EMIMAc, where previous efforts to dissolve Avicel cellulose in EMIMAc have only reached about 16 mol% (reported value is about 15 wt% cellulose in EMIMAc) [106].

The gels produced in this manner are flexible and self-standing, and stiff enough to be easily removed from the glass casting dish. This intermediate structure of cellulose gels produced from MCS after removal of DMSO has yet to be studied.

Understanding the gel structure and the structural evolution of the gel as EMIMAc is removed to produce a cellulose film can reveal important information about the resulting final cellulose film structure. IL is removed from these gels by washing with acetone followed by washing with ethanol to obtain the cellulose film. The gels were studied using SAXS, WAXS and rheology to understand the changes in structure with increasing cellulose composition, and the structure as a function of temperature and composition.

Previous work done by Rui Lu in our research group explored spin-coating thin films of MCS made with EMIMAc and DMSO, resulting in very thin and amorphous cellulose films. These thin films showed excellent stability in hot water, acid, and mild base solutions, as well as most organic solvents, making it a promising application for protective coatings [26]. It has been widely reported in literature that after regenerating cellulose from an ionic liquid solution using water as a nonsolvent, a conversion to a cellulose II crystal structure occurs [3, 102, 107, 108], however with the DMSO-EMIMAc binary solvent used in MCS, cellulose can be regenerated without being crystallized. This potential for controlling stability, water resistance, and variability in mechanical properties makes cellulose cast from MCS especially interesting. In this chapter, the structural evolution of cellulose throughout the casting process will be explored.

3.4.1 Experimental methods

3.4.1.1 Cellulose film casting

MCS was found to readily wet the surface of glass, but casting in a glass dish produced uneven films, as it would dry to the edges of the dish and the resulting film would have a greater thickness toward the edges of the dish. MCS would not wet a Teflon surface, so a dish was designed in which the substrate was glass, but Teflon sides were cut and fixed to the glass surface with silicone. This resulted in more evenly dried films that did not cling to the edges of the casting dish. The casting dish is weighed before adding MCS to monitor the progress of evaporation.

DMSO was evaporated by adding about 10 g of MCS (containing 3.4% cellulose, 6.0% EMIMAc, and 90.6% DMSO by molar percentage) to the prepared casting dish, then placing it in a 50 °C vacuum oven with a low vacuum of about 51 kPa. This temperature and pressure combination allows for evaporation of DMSO without allowing it to boil, which would create inhomogeneities in the resulting gels. The evaporation proceeds for about 24 hours, at which point the casting dish is removed from the oven and weighed and the mass of cellulose and EMIMAc that should be remaining in the gel is calculated once the DMSO has fully evaporated. When the total mass of DMSO has evaporated, the evaporation process is complete. The resulting gel is allowed to cool to room temperature, then is peeled carefully from the substrate and stored in a desiccator to prevent the absorption of water into the gel.

3.4.1.2 Ionic liquid removal

Since EMIMAc is nonvolatile, it must be removed by washing with a solvent that will dissolve EMIMAc and remove it from the gel. Acetone is shown to be a weak solvent for EMIMAc, capable of dissolving less than 1% of EMIMAc by weight. As a result, acetone will remove EMIMAc from the gel slowly, preventing wrinkling in the resulting cellulose film and maintaining a more homogeneous thickness and structure throughout the gel. After the initial soaking step, acetone is no longer an effective solvent for EMIMAc and it will not continue to remove it from the gel, at which point a stronger EMIMAc solvent, ethanol, is used for washing. The remaining gel is washed with ethanol until all EMIMAc is removed from the gel, producing a transparent cellulose film.

To study the structural evolution of the film throughout the washing process, a gel film of cellulose and EMIMAc is washed with the appropriate nonsolvent for a set period of time, then dried in the vacuum oven for 2 hours to remove any residual nonsolvent (acetone or ethanol). The dry gel is weighed to determine the mass of EMIMAc that was removed during each soaking event. After weighing, a small piece of the gel is cut, removed, and placed in a desiccator for later characterization.

Initial washing is done with acetone, starting with a soak of roughly 30 minutes and increasing time to remove additional EMIMAc is removed. Acetone is considered an ineffective solvent for EMIMAc when after 2 days no further decrease in mass is observed, indicating that EMIMAc is no longer being removed. At this point, the ethanol wash begins, beginning with a soaking time of 30 minutes and increasing

with each soaking event. The solvent removal process is complete when the film is soaked for 2 days in ethanol and no decrease in mass is observed.

3.4.1.3 Small and wide angle X-ray scattering

SAXS and WAXS measurements on each gel were carried out using the Xenocs Xeuss instrument in the University of Maryland X-ray Crystallography Center featuring a CuKα X-ray source, producing X-rays with wavelength 1.542 Å. Two configurations were measured, one covering the small-angle regime at about a 2500 cm sample-to-detector distance with a Q range of about 0.005 $Å^{-1} < Q < 0.2$ $Å^{-1}$, and one covering the wide-angle x-ray scattering regime. WAXS was conducted at a close distance of 133 cm with a 2θ of about $2\ ^\circ < 2\theta < 42\ ^\circ$. Gel samples were measured under vacuum, close to the center of each sample for 90 minutes of collection time. SAXS data were normalized during the data reduction based on the transmission relative to an empty beam, and the thickness of each sample measured with a micrometer.

During temperature ramp measurements SAXS and WAXS were measured simultaneously, so WAXS data was obtained using the 100k Dectris Pilatus detector. This detector is smaller and more narrow than the 300k detector, so the detector image obtained is more 1-dimensional resulting in less precise measurements.

3.4.1.4 Fourier transform infrared spectroscopy

FTIR was conducted on each gel sample using the ATR attachment because the gel samples were too thick for transmission measurement and the resulting spectra was oversaturated. Each sample was measured in two different locations on each side. The resulting spectra for each sample were averaged and were normalized based on the absorption values at wavenumbers 3800 nm^{-1}, which have absorptions of roughly 0.

3.4.1.5 Rheology

Rheology was conducted on gel samples. Initially, a strain sweep was run at a frequency of 0.1 Hz in order to determine a strain value within the linear elastic region of the gel. A strain of 0.15% was found to be within the elastic region but still high enough to elicit a response. A temperature sweep was run at a strain of 0.15% and a frequency of 0.1 Hz from room temperature to 120 °C.

3.4.2 Results and discussion

3.4.2.1 Fourier transform infrared spectroscopy

The composition of cellulose in the film throughout the ionic liquid removal process is calculated by monitoring the mass of ionic liquid removed throughout the washing process. This method is an indirect measurement of the ionic liquid remaining in the gel, so an alternative method was be employed to confirm these

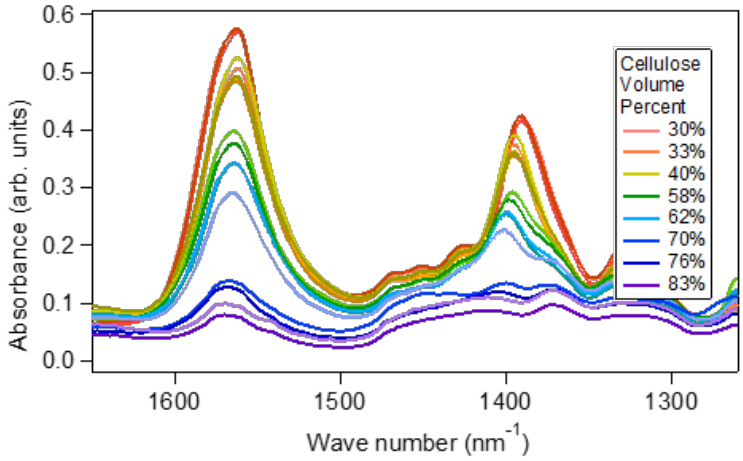

Figure 3.11: Plot of FTIR results showing the decreasing absorbance spectra of the EMIMAc associated peak.

measurements. FTIR-ATR was conducted on cellulose and EMIMAc samples in order to qualitatively monitor the EMIMAc content when washing [109]. At roughly 1570 nm there is a peak that indicates the presence of EMIMAc, as shown in Figure 3.11. This peak was fit to a gaussian curve, to quantify the relative cellulose content in the films.

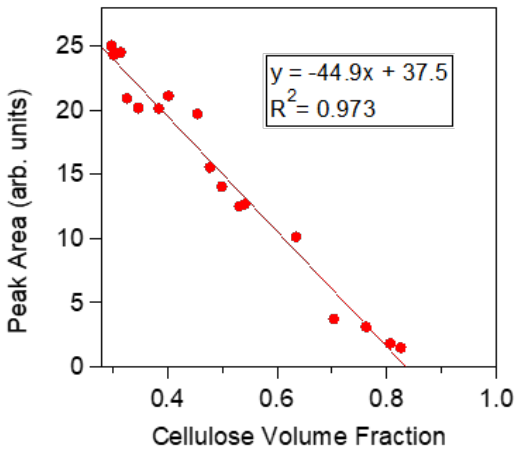

Figure 3.12: Area of EMIMAc peak at 1570 nm^{-1} plotted against cellulose volume fraction. A line of best fit was drawn showing good linearity with the data.

Figure 3.2 shows the peak area plotted against the estimated cellulose volume

fraction. The data was fit to a linear trendline with $R^2 = 0.973$, showing good agreement. If the trendline is extrapolated to a peak area of 0, the estimated volume fraction will be roughly 84%. This could be due to a number of reasons: 1) the detection limit for EMIMAc with FTIR is limited, and the peak at 1570 nm will not appear above background at low enough concentrations; 2) if EMIMAc is removed more readily from the surface than the center of the gel, and FTIR-ATR measures a limited volume close to the sample surface, there could be a concentration gradient resulting in the measured composition being different than the composition at the center; 3) mass measurements estimating how much EMIMAc is removed at each soaking procedure are not accurate. One source of inaccuracies in mass measurement can come from trace amounts of water that may be absorbed into the gel upon brief exposure to ambient conditions. While the water absorbed is likely negligible for a single mass measurement, compounded over multiple rounds this could lead to inaccurate mass measurements. An additional source of error is assuming the acetone and ethanol is fully removed from the gel between measurements. Due to the thickness of the films, and how long it takes for the soaking solvents to penetrate the gels, it can take many hours to fully remove trace amounts of solvent, and it is difficult to discern when the gels are fully dried. This means some mass measurements may include trace amounts of solvent remaining in the film, causing an inflated mass measurement, an underestimation in the amount of EMIMAc removed during that round of soaking, and thus an underestimation in the overall cellulose composition. These potential sources of error- peak detection limit, composition gradient, and mass inaccuracies- all would indicate an underestimation in the cellulose composition,

so the real cellulose composition is likely higher than presented in the following section. For the following analysis, while the overall cellulose volume percent may not be accurate, the trend of increase cellulose composition is still valid, and still provides useful information for the purposes of this work.

3.4.2.2 Small angle X-ray scattering

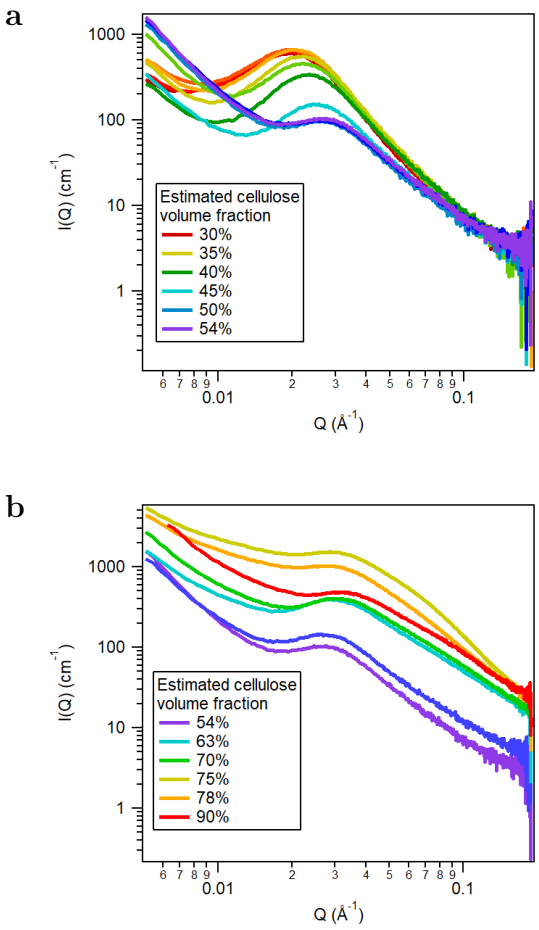

Figure 3.13: SAXS spectra of each EMIMAc/cellulose gel sample washed with a) acetone, and b) followed by ethanol, shown in the small angle region. A distinct structural correlation peak can be observed in each sample.

Gel samples of cellulose and EMIMAc were measured using SAXS. Figure 3.13a

shows the change in the gel scattering during acetone washing to remove EMIMAc. Scattering curves were normalized based on thickness and transmission, resulting in curves that overlap with similar behavior at high-Q. There is a clear ordering peak in the 30% gel sample, located at Q_m, visible before any ionic liquid removal has occurred, at roughly Q_m=0.020 Å^{-1}, corresponding to about d=31 nm. As ionic liquid is removed through acetone washing, Q_m shifts to a higher scattering angle and begins to diminish in intensity and prominence. By the end of acetone soaking, with roughly 54% cellulose, the peak has almost become a shoulder, and has shifted to about Q_m=0.029 Å^{-1}, corresponding to about d=22 nm. Figure 3.13b shows the scattering behavior throughout ethanol soaking. At roughly 63% cellulose the intensity increases dramatically, while the peak position remains relatively constant. Overall, throughout ethanol soaking there is a slight change in the peak position and a trend toward increasing intensity, however the increase is not consistent after normalization, indicating heterogeneities in the samples.

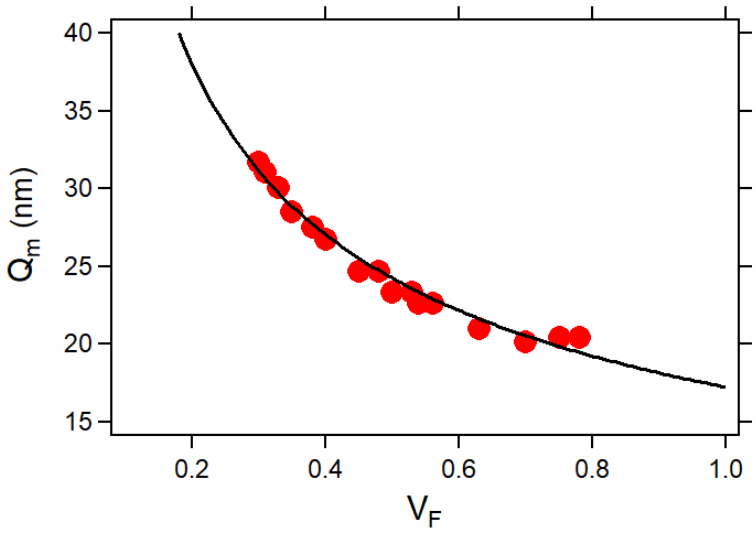

Figure 3.14: Periodic distance, determined by the location of each SAXS correlation peak, plotted against cellulose volume fraction.

A periodic distance, Q_m, associated with this ordering peak can be calculated based on the following relation:

$$d = \frac{2\pi}{Q} \tag{3.1}$$

Q_m has been plotted against cellulose volume fraction, V_F shown in Figure 3.14. The relationship between this Q_m and V_F can yield information about the structure of the scattering objects causing the structural ordering. A curve of the following equation has been fit to the data:

$$d \propto V_F^{-\frac{1}{2}} \tag{3.2}$$

This relationship with -$\frac{1}{2}$ power law indicates that Q_m is changing in 2 dimensions, implying that the scattering objects are 1-dimensional or rod-like in nature.

3.4.2.3 Wide angle X-ray scattering

WAXS was also conducted of these samples. Figure 3.15a shows the scattering data throughout acetone soaking. There is a large peak located at roughly 8°, and as cellulose composition increases the peak intensity increases as well and narrows a bit. There are also notable shoulders present at about $2\theta = 19$ and 27°, and as cellulose content increases these shoulders become sharper and more prominent. Additionally, the large amorphous halo, centered around $2\theta = 22°$, shifts slightly to the left as ionic liquid is removed. This is likely because the amorphous halo for cellulose is

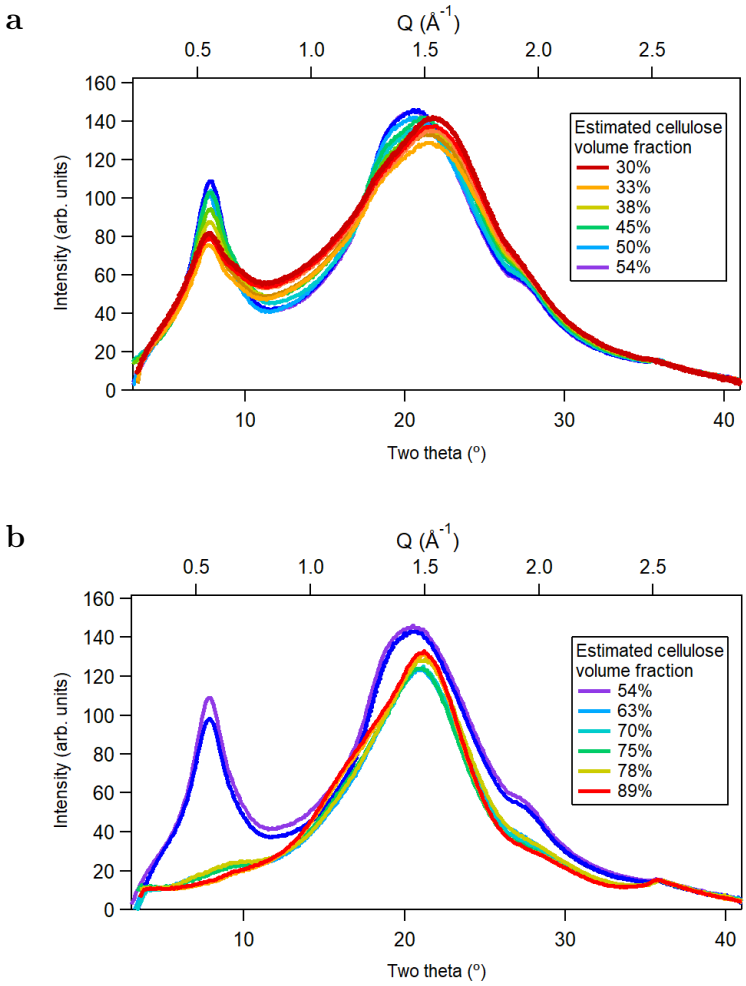

Figure 3.15: WAXS data for the gels throughout EMIMAc removal process, shown through a) acetone and b) ethanol washing.

centered at roughly 21°, whereas for EMIMAc it is at roughly 24°, so with less EMIMAc present the peak shifts slightly to the left. Figure 3.15b shows the WAXS data throughout the ethanol soaking process. After a very brief period of ethanol soaking the strong peak at $2\theta = 8°$ collapses, along with the shoulders at 19 and 27°. At the end of the ethanol soaking process, all three of these peaks have minimal intensity remaining, indicating a collapse in this short-range ordered structure due to ethanol soaking. The resulting WAXS curves underwent an additional two-step

normalization process. The first step involved matching the relative intensity to the corresponding SAXS data for the same sample. Additionally, there is a significant amount of scattering that carries over from the small angle regime and overlaps with the lower angle WAXS data. A power law curve was fit to the exponential decay following the peak in the small angle regime, such that the peak at 8° was cleanly presented. The scale, exponent, and flat background of this curve was estimated until the overlapping intensity was no longer visible in the WAXS data after being subtracted. After subtraction, the WAXS data were normalized by scaling according to the high angle scattering ($2\theta > 36°$) as this area of the spectra has the same slope across all samples.

$$I(2\theta) = \frac{A}{\pi} \frac{FWHM/2}{(2\theta - x_0)^2 + (FWHM/2)^2} \tag{3.3}$$

The WAXS data for each sample was fit to a model composed of 7 Lorentzian peaks, each described by Equation 3.3, where I is the peak intensity, A is the area under the curve, x_0 is the center of the peak, and full-width at half maximum (FWHM) is the full width at half maximum of the peak. The Multipeak Fitting package in Igor was used to accomplish the fitting for this data set, and for each peak, the area, FWHM, and peak center dictate the peak shape and size Resulting fitting parameters for all peaks at each cellulose volume fraction are shown in Table X. Each peak represented a different aspect of the cellulose/EMIMAc gel, and was treated differently during the fitting process. Parameters in bold were fixed during fitting. Peaks 0, 3, and 5 (highlighted in green) are included in the

cellulose and ionic liquid ordered structure, and the areas of these peaks were set in fixed proportions of 1:0.22:0.13, of the first, second and third ordering peaks respectively since they exhibited the same behavior during both acetone and ethanol soaking. Values in red are small peaks believed to be inherent to cellulose that do not change throughout fitting. The peak at about 36° is attributed to the length of the cellulose anhydroglucose unit, and is present in other reported data on cellulose allomorphs [110]. It is not clear what the peak at 9.5° corresponds to, though it seems to maintain a constant width and amplitude throughout the EMIMAc removal process so the area of this peak was fixed throughout fitting. However, the FWHM of the peak changes slightly, particularly after ethanol soaking begins and peak 0 has shrunk considerably. Values in blue are attributed to either a background (peak 2) or amorphous scattering halos (peak 4). Amorphous cellulose exhibits a broad halo centered at about $2\theta = 21°$ [111] and EMIMAc exhibits a broad halo centered at about 23° as shown by in-house WAXS measurements. Peak 4 shifts from 22.2° at the start of the washing process, 30% cellulose, down to around 21.0° at 50% cellulose, then a slight increase to 21.4° by the end of the washing process, 90% cellulose. This shift supports the claim that peak 4 is attributed to the amorphous components in cellulose, since as EMIMAc is removed from the gel, the peak center shifts closer to that of amorphous cellulose at 21°.

Figures 3.16a and 3.16b show two examples of the 7 peak fitting process for both the 30 and 45% cellulose samples respectively. Each figure is composed of 3 stacked plots. The bottom plot shows the models for each individual peak. The middle plot shows the total model, meaning all peaks summed together, overlaid onto

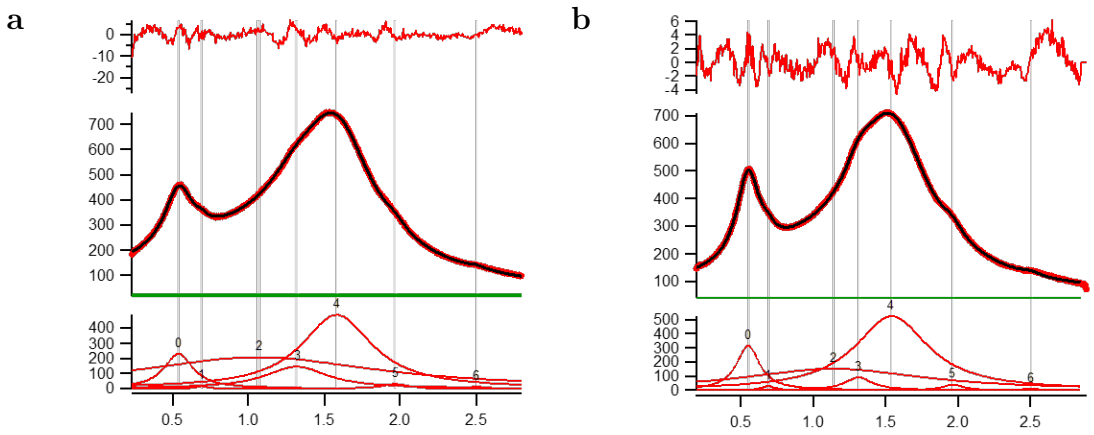

Figure 3.16: Examples of fitting of WAXS data using 7 peaks for a) 30% cellulose and b) 45% cellulose. Each figure consists of 3 plots- bottom) plot showing each individual peak included in the WAXS modeling; middle) the WAXS results plotted with the model, a sum of all the WAXS peaks; top) the residual after subtraction of the data from the applied model.

the experimental WAXS results. The top plot shows the residuals, or the difference between the experimental data and the multi-peak model. The overall trend of the ordering peaks (peaks 0, 3, and 5) being narrowed and increased in intensity can be observed between 30 and 45% cellulose content. Additionally peaks 1 and 6 remain narrow, low intensity, and relatively constant, while the background and amorphous peaks (peaks 2 and 4) shift slightly in position and remain very broad with a large peak area.

The crystallinity index of the cellulose and EMIMAc gel over the course of the washing process was calculated assuming peaks 0, 3, and 5 were associated with the ordered structure and is shown in Figure 3.17. Initially, in the gel that has just finished DMSO evaporation with no soaking, having a cellulose composition of roughly 30% by volume, the crystallinity index is roughly 0.11. Upon partial

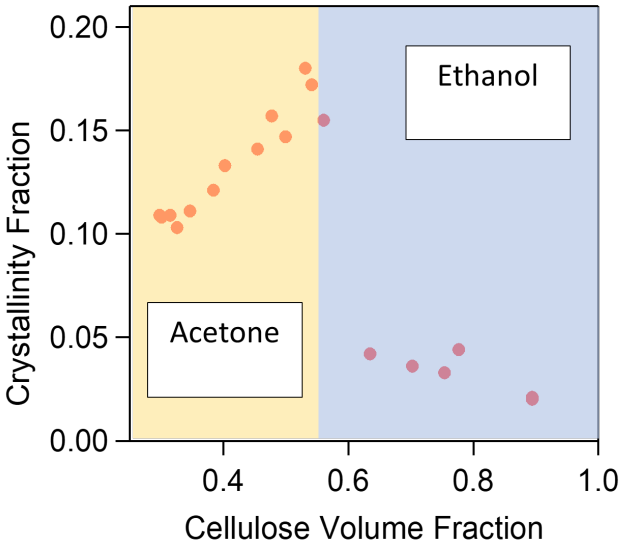

Figure 3.17: Crystallinity fraction plotted against cellulose volume fraction, the plot is divided between acetone and ethanol soaking.

removal of EMIMAc from the gels using acetone the crystallinity increases to roughly 0.18, after which acetone is no longer an effective solvent for EMIMAc removal, the cellulose composition of the gel at that point is roughly 54%. Soaking continued using ethanol, which very abruptly results in a collapse in ordering fraction, down to about 0.02.

The cellulose volume fraction after extraction of the EMIMAc by ethanol is approximately 90%. The composition of the remaining 10% of the film is not clear, it could be EMIMAc that is trapped due to the large thickness of the film. The film was prepared with increased thickness in order to improve the signal in SAXS and WAXS measurements, which makes EMIMAc removal a longer process. The FTIR results indicate the EMIMAc content is lower than the volume percent would suggest but the ATR measurement only probes just under the surface of the film. If the EMIMAc concentration is greater in the center of the film than at the surface,

this would explain why the plot in figure 3.12 appears to overestimate the EMIMAc content. The cellulose content may also be higher than 90%, due to potential error accrued during the repeated washing, drying, and weighing steps.

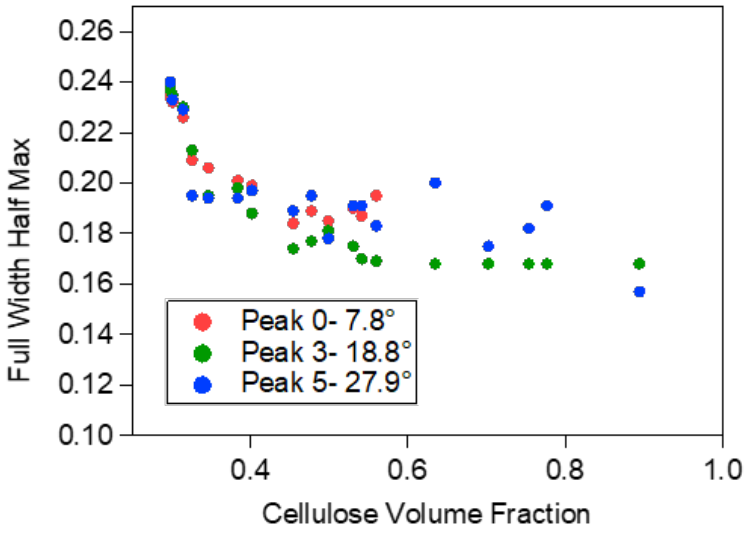

Figure 3.18: FWHM of peaks associated with ordering (peaks 0, 3, and 5) plotted against cellulose volume fraction.

The width of the peaks taken at half the maximum amplitude of each peak, or FWHM was a fitting parameter during peak fitting. Figure 3.18 shows the FWHM throughout the soaking process to remove EMIMAc. Between about 30 and 60% cellulose, the FWHM decreases significantly, then begins to plateau at higher cellulose compositions. The initial decrease in FWHM occurs mostly during the acetone soaking period, then when ethanol soaking begins, the FWHM stays relatively constant. The narrowing of the peaks (decrease in FWHM) indicates the ordering is improving in the lattice directions associated with the peaks. It is observed that acetone soaking results in an improvement in ordering for all three ordering peaks and the relative crystallinity is increasing, where during ethanol soaking when

the peak areas are decreasing dramatically and crystallinity drops significantly, the FWHM remains relatively constant. FWHM has an inverse relationship with the size of crystallite in an ordered sample, while the peak area indicates the volume percent of ordering present in the sample. Since FWHM remains constant this indicates that the quality of the ordering is not decreasing, but the dramatic reduction in area indicates the decrease in volume fraction of ordering within the film. Upon briefly washing with ethanol, the ordering is eliminated almost entirely.

Volume fraction	Peak 0			Peak 1			Peak 2			Peak 3			Peak 4			Peak 5			Peak 6		
	2θ (°)	Area	FWHM	2θ (°)	Area	FWHM	2θ (°)	Area	FWHM	2θ (°)	Area	FWHM	2θ (°)	Area	FWHM	2θ (°)	Area	FWHM	2θ (°)	Area	FWHM
0.30	7.6	19.0	0.23	**9.5**	**1.8**	0.17	**16.9**	109.1	1.33	18.4	4.2	0.24	22.2	96.9	0.58	27.9	2.4	0.24	**36.1**	**0.80**	**0.13**
0.30	7.6	18.2	0.23	**9.5**	**1.8**	0.18	**16.9**	103.0	1.33	18.5	4.0	0.23	22.2	96.7	0.60	27.8	2.3	0.23	**36.1**	**0.80**	**0.13**
0.31	7.6	18.2	0.23	**9.5**	**1.8**	0.17	**16.9**	103.6	1.36	18.4	4.1	0.23	22.2	94.4	0.59	27.9	2.3	0.23	**36.1**	**0.80**	**0.13**
0.33	7.6	16.4	0.21	**9.5**	**1.8**	0.18	**16.9**	81.4	1.38	18.5	3.6	0.21	22.0	108.1	0.67	27.9	2.1	0.19	**36.1**	**0.80**	**0.13**
0.35	7.6	17.9	0.21	**9.5**	**1.8**	0.17	**16.9**	82.9	1.39	18.5	4.0	0.20	21.9	107.9	0.65	27.9	2.3	0.19	**36.1**	**0.80**	**0.13**
0.38	7.7	19.4	0.20	**9.5**	**1.8**	0.15	**16.9**	81.2	1.37	18.5	4.3	0.20	21.9	105.8	0.62	27.9	2.5	0.19	**36.1**	**0.80**	**0.13**
0.40	7.7	21.2	0.20	**9.5**	**1.8**	0.16	**16.9**	78.3	1.39	18.5	4.7	0.19	21.8	106.1	0.61	27.9	2.7	0.20	**36.1**	**0.80**	**0.13**
0.45	7.8	22.4	0.18	**9.5**	**1.8**	0.13	**16.9**	73.5	1.39	18.5	5.0	0.17	21.6	108.0	0.60	27.8	2.8	0.19	**36.1**	**0.80**	**0.13**
0.48	7.8	23.6	0.19	**9.5**	**1.8**	0.15	**16.9**	60.6	1.45	18.6	5.2	0.18	21.5	107.7	0.60	28.0	3.0	0.20	**36.1**	**0.80**	**0.13**
0.50	7.7	23.1	0.18	**9.5**	**1.8**	0.20	**16.9**	48.4	2.33	18.7	5.1	0.18	21.0	130.6	0.65	27.8	2.9	0.18	**36.1**	**0.80**	**0.13**
0.53	7.8	26.1	0.19	**9.5**	**1.8**	0.19	**16.9**	37.4	1.63	18.7	5.8	0.18	21.1	120.1	0.60	27.9	3.3	0.19	**36.1**	**0.80**	**0.13**
0.54	7.8	25.6	0.19	**9.5**	**1.8**	0.20	**16.9**	44.3	1.98	18.8	5.7	0.17	21.0	119.6	0.59	27.9	3.2	0.19	**36.1**	**0.80**	**0.13**
0.56	7.8	24.1	0.19	**9.5**	**1.8**	0.21	**16.9**	57.3	3.21	18.8	5.4	0.17	21.0	117.7	0.58	27.9	3.1	0.18	**36.1**	**0.80**	**0.13**
0.63	7.6	1.6	0.24	**9.5**	**1.8**	0.23	**16.9**	15.7	0.51	18.7	**1.0**	**0.17**	21.2	86.6	0.50	28.3	2.0	0.20	**36.1**	**0.80**	**0.13**
0.70	7.7	1.4	0.29	**9.5**	**1.8**	0.23	**16.9**	21.2	0.51	18.6	**1.0**	**0.17**	21.3	79.6	0.47	28.5	1.5	0.17	**36.1**	**0.80**	**0.13**
0.75	7.8	1.0	0.28	**9.5**	**1.8**	0.26	**16.9**	23.1	0.51	18.6	**1.0**	**0.17**	21.2	74.8	0.44	28.7	1.4	0.18	**36.1**	**0.80**	**0.13**
0.78	7.8	2.3	0.31	**9.5**	**1.8**	0.23	**16.9**	20.0	0.51	18.6	**1.0**	**0.17**	21.2	85.0	0.48	28.7	1.7	0.19	**36.1**	**0.80**	**0.13**
0.90	7.8	0.0	0.00	**9.5**	**1.8**	1.45	**16.9**	30.6	0.48	18.8	**1.0**	**0.17**	21.4	72.0	0.41	28.7	1.2	0.16	**36.1**	**0.80**	**0.13**
0.90	7.4	0.0	0.00	**9.5**	**1.8**	0.52	**16.9**	30.8	0.46	18.8	**1.0**	**0.17**	21.4	73.1	0.41	28.7	1.2	0.16	**36.1**	**0.80**	**0.13**

Table 3.1: Fitting parameters from WAXS modeling, including the peak angle 2θ, area, and FWHM. Parameters in bold were fixed during fitting to provide a good fit. Peaks 0, 3, and 5 are included in the cellulose and ionic liquid ordered structure, areas of these peaks were fixed at ratios of 1:0.22:0.13 for peaks 0, 3, and 5 respectively. Peaks 1 and 6 are small peaks believed to be inherent to the materials that do not change throughout fitting. Peak 2 is a broad background that varied by sample. Peak 4 is attributed to amorphous scattering from both cellulose and EMIMAc.

3.4.2.4 Multiscale structural ordering of EMIMAc and cellulose gels

Figure 3.19 shows a schematic of the proposed model that describes the behavior of the cellulose and EMIMAc gels observed using X-ray scattering. From WAXS, we observe a significant local ordering peak corresponding to a d-spacing of about 1.1 nm, and from SAXS, we observe Q_m corresponding to a periodic distance of about 30 nm, indicating a multi-scale ordering structure. The schematic shows the local ordering of cellulose/EMIMAc regions, potentially bundles of aligned cellulose chains separated by EMIMAc at a fixed spacing of 1.1 nm, shown inside the dashed ovals. The locally ordered regions give rise to nematic long-range ordering corresponding to the distance between these ordered regions, which is occupied by an amorphous gel-like region of cellulose and EMIMAc and separating the bundles by a distance starting at 30 nm and decreasing to 19 nm after soaking with acetone.

During acetone soaking, ordering within the gels is improved based on the decrease in FWHM and increase in crystallinity index from about 0.11 to 0.17. Q_m decreases from about 30 nm to 22 nm. Based on these results, acetone is selectively removing EMIMAc from the amorphous regions of the gel but cannot penetrate the locally ordered bundles. As the total volume of the amorphous regions decreases, the distance between ordered regions decreases as the overall volume of the film decreases. Due to the $-\frac{1}{2}$ exponential relationship between V_F and Q_m, the ordered structures of cellulose and EMIMAc bundles are estimated to be one-dimensional in nature. Additionally, the local ordering of the gel improves as the overall volume fraction of primarily amorphous material decreases. This is further supported by

the fact that acetone is a weak solvent for EMIMAc, and is unable to penetrate the cellulose/EMIMAc ordered structure within the bundled regions. When acetone is no longer an effective solvent for EMIMAc, at roughly 54% cellulose, this implies that the EMIMAc present in the amorphous regions has been mostly removed, and the remaining EMIMAc is largely present in the ordered regions.

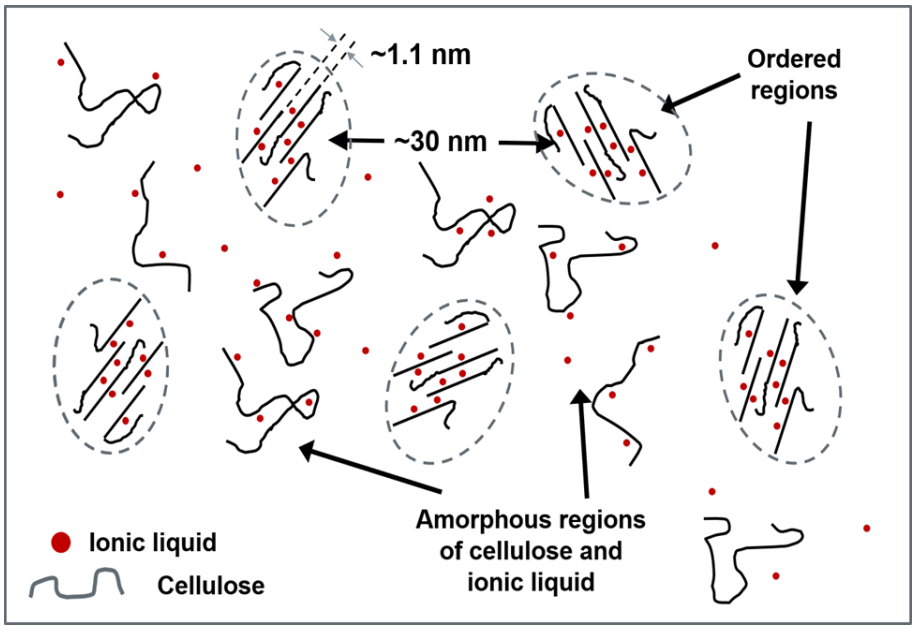

Figure 3.19: Schematic illustrating the multiscale ordering system observed in SAXS and WAXS, and the relationship between the small- and large-scale ordering distances.

During ethanol soaking, the previously inaccessible EMIMAc in the ordered regions can be removed. Despite the EMIMAc removal process with ethanol being gradual over multiple soakings, the ordering peaks are collapsed almost immediately at 65% cellulose. This implies that despite EMIMAc still remaining within the dense regions of the gel, the introduction of ethanol disrupts the ordering causing the peaks to collapse. During this process, there is a slight change in Q_m, from 22 nm to 19 nm, due to small changes in volume within the gel. This could ether correspond

to small amounts of EMIMAc remaining in the amorphous regions being removed by ethanol and causing the ordered regions to move closer together, or to a volume change exclusively within the ordered regions that results in a decrease in long-range ordering as a result. Additionally, despite the fact that the ordering within the dense regions is lost, a difference in density between this and the amorphous regions is still present, and is manifested in the SAXS data which still shows a significant correlation peak. However, the SAXS data also shows a significant increase in intensity upon the introduction of ethanol. This implies an increase in overall scattering contrast, which could be the result of void formation from EMIMAc removal. At the time ethanol soaking begins, the overall cellulose composition has increased, resulting in a much stiffer gel. This high stiffness could prevent the gel from relaxing after removing EMIMAc, resulting in voids instead of a change in volume. This could also explain why the change in Q_m during ethanol soaking is so minimal, since a change in volume would result in a change in spacing as well.

This schematic explains the relative behaviors of the amorphous and ordered regions present in the gels based on X-ray scattering data, however more information is needed to fully understand the system. The amorphous and ordered regions likely have different compositions of cellulose and ionic liquid. These values can be estimated based on relative changes in EMIMAc content during soaking, but additional experiments can help more directly measure the compositions. Additionally, further characterization is required to determine whether void formation is the cause of the increase in scattering intensity during ethanol soaking. Finally, elemental analysis would help in more accurately determining the cellulose composition of each gel,

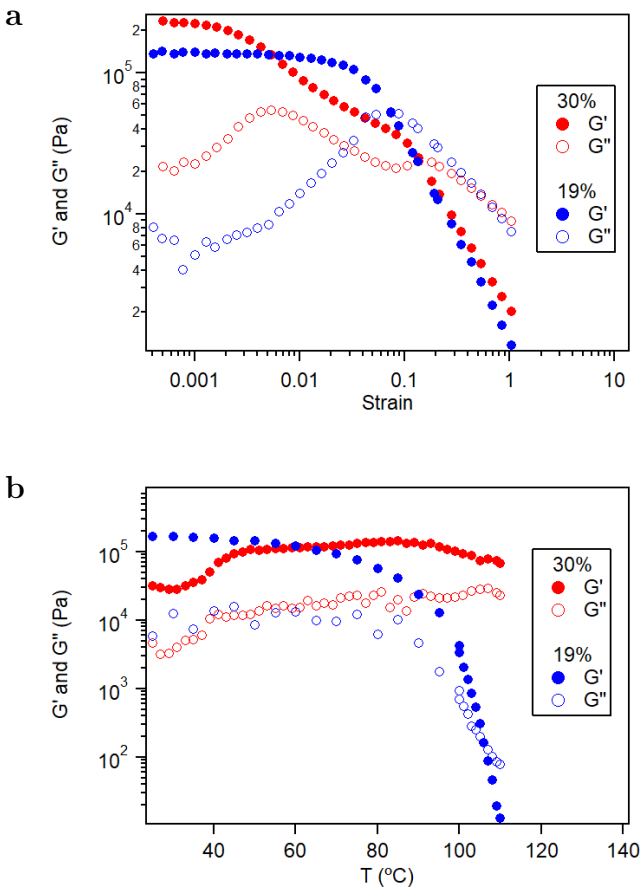

Figure 3.20: Rheology data showing the results of a) strain ramp testing of each gel sample showing storage and loss moduli plotted against strain, and b) rheology results showing storage and loss moduli plotted as a function of temperature under alternating strain of 0.15%.

since it is likely there is some error associated with this measurement.

The amorphous nature of the resulting cellulose films is also worth noting. Cellulose dissolution and regeneration of cellulose has been extensively reported in literature. While the conventionally used nonsolvent is water, this results in a rather significant conversion to cellulose II with relatively high crystallinity fractions of up to 70% [3, 102, 107, 108]. The structures obtained in this study were almost fully amorphous, illustrating the unique impact the DMSO cosolvent system can have on

the resulting cellulose structure.

3.4.2.5 Rheology

The effect of temperature on the behavior of the concentrated gels is important for understanding the solubility of cellulose within this system and whether this ordered structure can be controlled. Rheological measurements were conducted on gels with 30% cellulose and 19% cellulose by volume. Figure 3.20a shows the storage and loss moduli of these two gels as a function of shear strain. In the 30% cellulose gel, there appears to be two transitions in modulus occuring at approximately 0.004% and 0.06% strain, while in the 19% gel there is only one, with the transition occurring at approximately 0.05% strain. Modulus data for both gels showed relatively linear behavior at strains of roughly 0.002%, so this strain value was chosen for a temperature ramp measurement, the results of which are shown in Figure 3.20b. The 30% gel showed little to no change in overall modulus behavior upon heating, but the 19% gel showed a dramatic decrease in modulus between 80 and 100 °C.

Figure 3.21 shows a plot of tan(δ), which was obtained from the relationship shown in equation 3.4.

$$tan(\delta) = \frac{G''}{G'} \tag{3.4}$$

A transition of tan(δ) in which it increases to over a value of 1 indicates the viscous behavior is dominating the rheological response of the sample, indicating a transition from solid to fluid. The 19% gel clearly shows a sharp increase in this

value beginning at about 100 °C, increasing to about 10, showing a clear transition from solid to fluid and an absence of a significant elastic response of the gel. The 30% gel however, showed a slight increase at 100 °C, but not increasing beyond 0.4, and during the rest of heating the value stayed relatively constant, indicating this sample remained as a gel throughout heating and the elastic response dominates the rheological behavior of the gel.

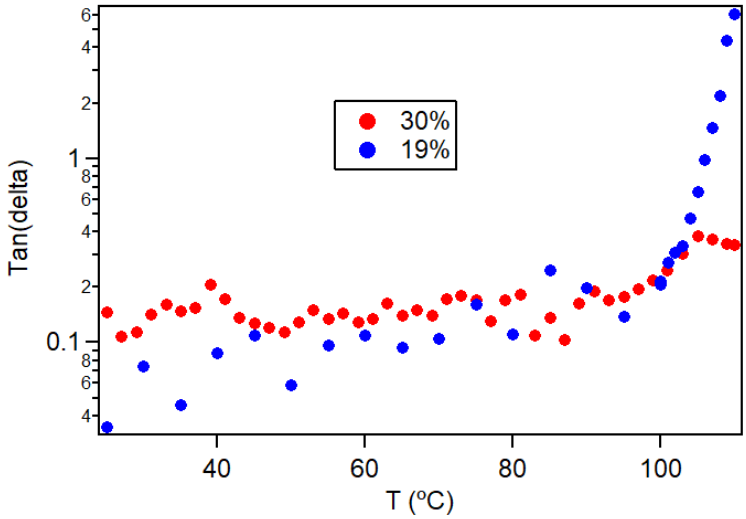

Figure 3.21: Plot of tan(δ) versus temperature of each of the cellulose and EMIMAc gels, showing the transition from gel to viscous fluid for the lower concentration gel.

The transition from gel to fluid is representative of the EMIMAc/cellulose gel dissolving and forming a cellulose solution. This experiment indicates that while the MCS is fully dissolved with an EMIMAc to cellulose ratio of roughly 1.75:1, after evaporating DMSO the resulting gel does not redissolve upon heating. This indicates the role that DMSO plays in allowing cellulose to more easily dissolve. Additionally, when the EMIMAc:cellulose ratio is raised to about 2.7:1, well over the solubility limit, the gel can be redissolved upon heating.

3.4.2.6 Small angle X-ray scattering as a function of temperature

Figure 3.22 shows the effect of temperature on the multiscale ordering observed in previous measurements, with Figure 3.22a showing SAXS data and Figure 3.22b showing WAXS data. In the SAXS data, there is a significant drop in intensity upon heating to 60 °C, by 80 °C the ordering peak begins to disappear, and by 100 °C there is no no significant structure present in the sample. The peak does not appear to shift to a higher or lower Q during the heating process, indicating that the ordering distance is preserved as the structure in the gel dissolves.

The WAXS data appears different from previously reported data, shown in Figure 3.15, because it was measured at the same time as the SAXS data and had to be obtained with the 100k Dectris Pilatus detector. This results in a less precise estimate of 2θ, so it is difficult to compare directly with previously shown WAXS results. However, there is a significant change in the WAXS pattern upon heating from about $23 < 2\theta < 33$, that likely corresponds with peak 5 from the previous WAXS analysis shown in Table 3.1. Peak 5 was one of the three peaks associated with local ordering in the cellulose/EMIMAc gels. At 100 °C the remaining scattering is dominated by a broad peak at about 21°, which likely corresponds to peak 4 from previous analysis and is a combination of EMIMAc scattering and the cellulose amorphous halo.

With an excess of EMIMAc present with the gel, ordering is eliminated in both SAXS and WAXS measurements. Between 80 and 100 °C, the ordering is fully eliminated and the gel melts into a viscous fluid, as observed in rheology. After

allowing the gel to cool for 7 days, the ordering reappears in both the SAXS and WAXS data, showing that the melting process is reversible. It is notable that in SAXS data, the ordering peak is gradually eliminated with increasing temperature, then upon cooling gradually returns to a comparable intensity. In the WAXS data, the ordering is eliminated almost completely at 60 °C, at which point the SAXS peak was still prominent. Upon cooling, the WAXS ordering at about 27° appears suddenly, and only after 7 days, at which point the long-range ordering in SAXS has completely reformed. This indicates that the local ordering may be forming as a result of longer range ordering. One possible mechanism is that the long range ordering is a result of a phase separation that occurs upon cooling that creates density and concentration fluctuations within the gel. The denser regions of cellulose and EMIMAc in the gel exist at a particular composition that results in a cohabitated locally ordered structure.

3.5 Conclusions

The structure of cellulose and EMIMAc gels was studied throughout the EMIMAc removal process using SAXS and WAXS. A multiscale ordering structure was observed in which 1.1 nm small-scale local ordering containing both cellulose and ionic liquid is present in ordered regions of the gels. This local ordering forms due to longer range ordering corresponding to the periodic distance, Q_m, between the locally ordered regions. The long range ordering was shown to change with the EMIMAc washing process, shifting from 30 to 19 nm. This decrease was related to

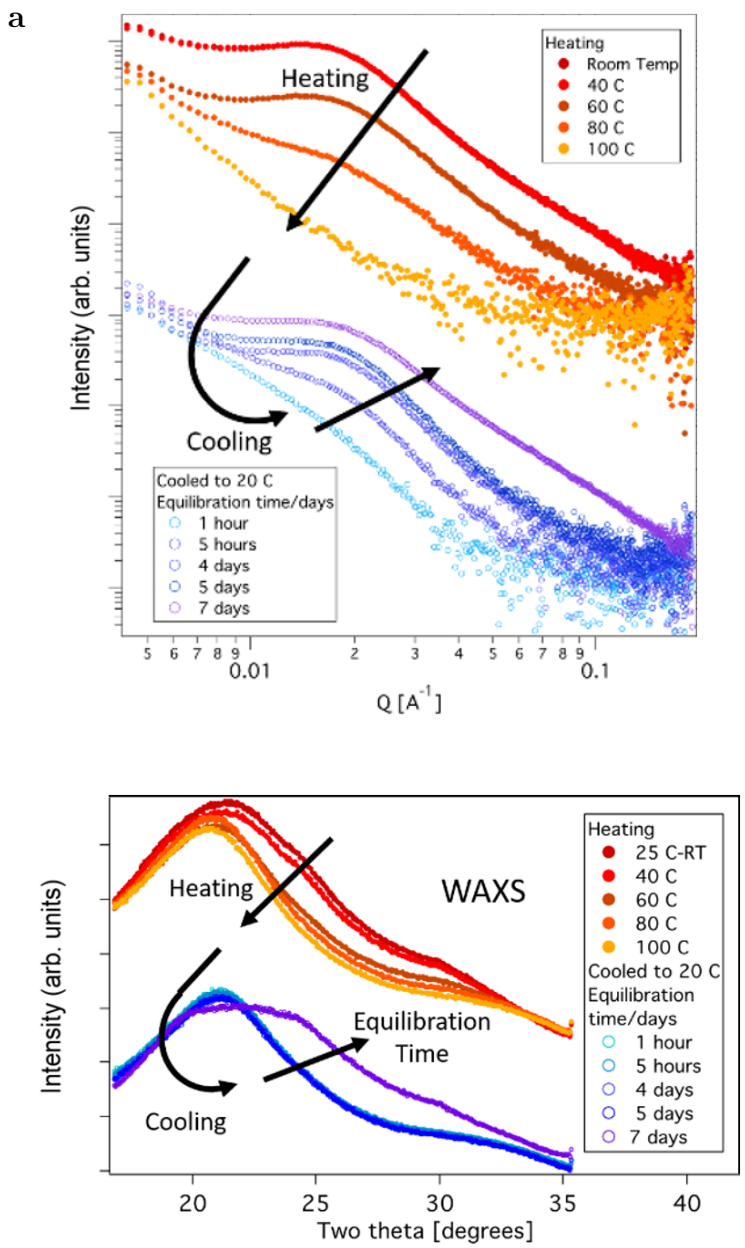

Figure 3.22: a) SAXS and b) WAXS with temperature dependence of a gel with added EMIMAc results in elimination of multiscale ordering structure.

the change in cellulose volume fraction by a power law of -$\frac{1}{2}$, indicating a change in distance between 1-dimensional or rod-like structures. While this local ordering is ultimately eliminated once ethanol is employed to remove the remaining EMIMAc

from the gels, the long-range ordering peak is still present in the small-angle regime which could play a significant role in defining the microstructure of the resulting cellulose films.

Additionally, the amorphous nature of these cellulose films makes them unique amongst other cellulose structures in the literature that have been regenerated from ionic liquids, as this typically results in a crystalline cellulose II film. This can result in different mechanical properties, as well as different interactions within a composite system. In more crystalline cellulose it is more favorable for cellulose chains to assemble into ordered structures, therefore bonding with like cellulose components. Amorphous cellulose will not readily form ordered structures, and therefore has a greater probability to interact with other cellulose structures within a composite.

The multiscale ordering present in these gels is stable upon heating at low enough ratios of EMIMAc to cellulose. At higher concentrations of EMIMAc, the ordering structure can be eliminated upon heating, and will ultimately reform when given sufficient time to cool and equilibrate. This indicates the importance of DMSO within MCS, as with DMSO present in solution, the cellulose will fully dissolve at lower ratios of ionic liquid than with no DMSO. Additionally, this shows the dense cellulose and ionic liquid gels solid nature is likely derived from the multiscale ordered structure shown in SAXS and WAXS data, because both are eliminating upon heating and reform upon cooling. The short range ordering is eliminated before the long range ordering during heating, and reforms after the long range ordering during cooling. This indicates that the short range ordering forms as a result of the long range ordering, possibly due to density and concentration fluctuations resulting

from a phase separation that occurs during cooling.

While the implication of this multiscale ordering structure on the resulting cellulose film properties are not known, having the ability to control the presence of this ordering could be significant in controlling the behavior of these regenerated cellulose films. In the following chapter, mechanical and water uptake properties of amorphous cellulose films cast from MCS are investigated, along with their role in all-cellulose nanocomposite films.

Chapter 4: All-cellulose composites

4.1 Introduction

Cellulose nanomaterials, namely CNF and CNC, have garnered significant attention in polymer nanocomposite research as a way of improving the mechanical properties of matrix polymers through reinforcement. However, various treatment is often necessary to enhance compatibility of CNF in nanocomposite systems and improve the properties of CNF-based films. Common pretreatments of CNF will be discussed as they pertain to nanocomposite fabrication, such as modifying surface groups, solvent exchange, and reducing water uptake of CNF. Production methods of CNF-based films and nanocomposites will be discussed. A summary of work conducted on CNF nanocomposites will be presented, as well as a discussion on the range of mechanical properties that result from these nanocomposites.

A brief review of the work done on all-cellulose composites will be presented, as well as a summary of this thesis work regarding nanocomposites formed by combining MCS and CNF. Motivations for this project will be presented along with preparation, resulting properties, and a proposed reinforcement mechanism. The resulting MCS/CNF nanocomposite films underwent tensile testing along with testing their water uptake and optical properties. The results of this testing and the

interactions between the cellulose components will be discussed.

4.2 Background

4.2.1 Pre-treatments for CNF

In fabricating films from CNF and incorporating them into nanocomposites, significant work has gone into various treatments to make it a more versatile material. This section will discuss the modification of CNF surface groups to promote interfacial compatibility in nanocomposites and improve mechanical properties, redistribution of CNF into organic solvents to expand potential nanocomposite opportunities, and reduction of CNF water uptake to combat the hydrophilic nature of cellulose and its tendency to weaken upon exposure to moisture.

One of the steps in producing CNF involves converting one of three surface hydroxyl groups to a sodium carboxylate group with a negative charge. While this is useful in processing as it allows CNF to be fully separated, this charged carboxylate group cannot form hydrogen bonds [112]. In work done by Fujisawa et. al. they successfully replaced the sodium carboxylate group ($-COONa$) with free protonated carboxylate group ($-COOH$) by treating the initial CNF with acid. Each suspension of CNF, both $-COOH$ and $-COONa$, were dried to form self-standing transparent and flexible films, with varying mechanical properties. While the Young's modulus of the $-COOH$ CNF films was increased, the overall strain to failure decreased, resulting in stiffer but less ductile films [113].

Limiting nanocomposites to the inclusion of water-soluble polymers is rather

stifling as many commonly-used synthetic polymers are hydrophobic [114,115]. There has been considerable work done examining distributing suspensions of CNF into organic solvents. Recently, in work done by Okita et. al, solvent exchange for CNF suspensions in water was done using DMF, 1,3-dimethyl-2-imidazolidinone (DMI), dimethylacetamide (DMAc), N-methyl-2-pyrrolidone (NMP), and DMSO. This was achieved using two different methods. The first involved stirring the aqueous CNF suspension into an equal amount of organic solvent, then heating to 50 °C under constant stirring until the water had mostly evaporated, then sonicated to aid in dispersion. The second method involves exchanging the $-COONa$ groups for free carboxylate, $-COOH$, groups, as mentioned previously. The $-COOH$ CNF suspensions were washed with aqueous 0.1 M HCl followed by acetone with filtration. The intended organic solvent was added to the acetone-containing suspensions, then stirred at 50 °C to allow all acetone to evaporate, then sonicated for dispersion [115]. The results indicated that using the protonation method and exchanging $-COONa$ groups for $-COOH$, CNF was able to be redispersed at an individual fiber scale in all the tested organic solvents. Without protonation, the only organic solvent that was capable of good CNF dispersion after solvent exchange was DMSO. (Okita et al., n.d.) The ability to redistribute CNF into organic solvents allows for nanocomposites to be fabricated with a wider range of polymers such as polystyrene [116] or poly(vinylidene fluoride) [117].

4.2.2 Improving water-resistance of CNF-based films

A considerable disadvantage of CNF is its affinity for water. Cellulose is already hygroscopic, resulting in considerable weakening of cellulosic materials upon water absorption. The mechanical strength of CNF films is partially based on the dense network of interfibrillar hydrogen bonding, but as water is absorbed it interacts primarily with the surface hydroxyl groups on cellulose nanofibers. This can disrupt the hydrogen bonding between cellulose nanofibers, resulting in a weakening of mechanical properties. Additionally, the charged surface $-COONa$ present on CNF means that as water is absorbed, the charge groups dissociate and will result in coulombic repulsion between the nanofibers, similar to the dissociation mechanism that results in a dispersion of CNF via TEMPO oxidation. Improving the water resistance of CNF is crucial to improving their viability as a structural polymer for laminate film applications. Common methods for evaluating water resistance are measuring water uptake and wet tensile strength or stiffness, and both will be noted in the following review on this work.

The most intensely studied method of water-proofing CNF is through surface modification. By modifying the surface $-COONa$ group, the hydrophilicity of CNF can be controlled. One example involves using metal chloride solutions to trigger ion-exchange and change the sodium ion on the $-COONa$ group to a different metal ion, namely aluminum, iron (III), calcium, and magnesium. The results showed that trivalent metal ions such as iron (III) and aluminum improved mechanical properties of CNF films under exposure to humidity, maintaining stiffness on the order of $\sim$10

GPa which is comparable to dry CNF. Additionally, upon soaking in water the CNF films containing metal ions other than Na were shown to absorb significantly less water. However, each film still absorbed >3 times its own weight in water after one hour of soaking [118].

Mild esterification processes have been employed to modify CNF films by selectively grafting alkyl chains to surface hydroxyl groups of cellulose. The resulting films were shown to absorb roughly 50% less water when exposed to high humidity, and decrease the loss in mechanical properties upon exposure to moisture as well [119].

Other methods for improving water resistance of CNF center around crosslinking with other polymers in a nanocomposite film. One example features poly(acrylic acid) (PAA), which is used to thermally crosslink with cellulose, forming ester bonds. The crosslinking reduces the number of exposed hydroxyl groups which can reduce the overall water uptake of the film. This crosslinking was also shown to enhance the mechanical properties of the films, improving the stiffness and tensile strength as compared to neat CNF, both in dry and in wet conditions [120]. Similar crosslinked nanocomposites were formed with other polymers such as PVA, (Hakalahti et al., 2015) chitosan [121], and carboxymethyl cellulose [122], resulting in improved water resistance and wet mechanical properties.

These methods have been shown to be effective means of providing CNF-based films with water-resistance, although it introduces further processing steps into a material like TEMPO-oxidized cellulose nanofibers. A simpler step for improving water-resistance is desirable.

4.2.3 Fabricating self-standing CNF-based films and nanocomposites

Cellulose nanomaterials, namely both CNF and CNC, have garnered significant attention in polymer nanocomposite research as a way of improving the mechanical properties of flexible matrix polymers through rod-like reinforcement. Typically, this is accomplished by combining a suspension of cellulose nanomaterials with a polymer soluble in a compatible solvent. This tends to limit applications of CNF and CNC since they are typically suspended in aqueous media, requiring the matrix polymers to be soluble in or compatible with water [123, 124]. Polymers can be dissolved in water, then mixed with a suspension of CNF. One requirement is that the polymers do not contain positively charged end groups, as this will result in agglomeration since charge groups on CNF contain negative charges. Interactions between the polymer and CNF should be minimal to also prevent aggregation that could occur in suspension.

One method for nanocomposite film production with CNF-based materials includes suspension casting. The composite mixture is deposited into a dish and the water is allowed to evaporate, which can be done at ambient conditions, an oven with or without applied vacuum, or at specified humidity conditions. This method causes a relatively homogeneous concentration increase as the solvent evaporates, as illustrated in the schematic provided on the left in Figure 4.1 [114]. As fiber suspensions are relatively low concentration (typically around 1% mass), the sheer volume of solvent required for a film of adequate thickness is high and requires long evaporation times. You can decrease this time by increasing the evaporation

temperature and/or vacuum to remove solvent more quickly. Faster removal of solvent can create a gradient of solvent vapor in the environment as it is removed from the dish, resulting in a more uneven rate of evaporation across the film and uneven final film thickness. High temperatures, particularly above 60-70 °C, were also shown to cause light discoloration and browning in resulting films. Due to these limitations on temperature and vacuum, well executed suspension casting can require multiple days of evaporation [125].

Vacuum filtration is another method through which CNF-based films can be fabricated. The composite mixture is poured into a funnel equipped with micropore filters with an applied vacuum. While some material can pass through the filter along with the solvent, the CNF toward the base of the funnel form a dense mesh network that prevents more material loss. This causes a concentration gradient moving up from the base of the funnel as more layers of CNF will stack and collapse as the suspension is filtered. A schematic of this concentration increase during filtration is illustrated on the right in Figure 4.1 [114]. Once complete, a dense gel containing the nanofibers remains, which can be dried under hot pressing or surface-clamped vacuum drying. The gel needs to be dried under constrained conditions or wrinkling and shrinking can occur. One disadvantage is that depending on the size of nanofibers, a significant loss of smaller fibers can occur through the membrane filter. However, it has been shown that drying through vacuum filtration can increase in-plane orientation of nanofibers as compared to suspension casting, which can improve their mechanical properties.

For CNF-based nanocomposite films, both suspension casting and vacuum

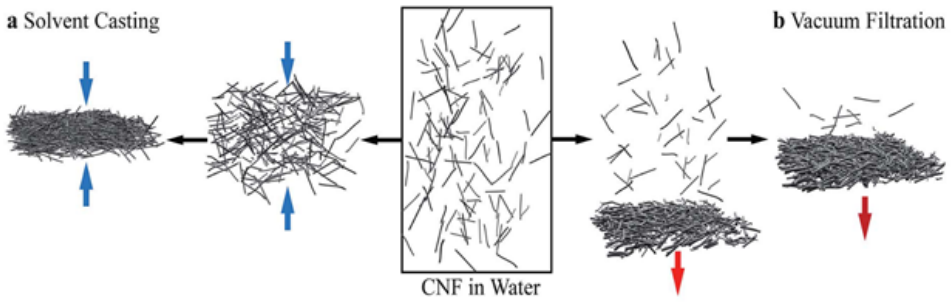

Figure 4.1: Schematic showing the differences in the concentration process in A) solvent casting and B) vacuum filtration [114]. © 2017

filtration can be employed. For both methods, a material dissolved or suspended in the same or a compatible solvent is mixed into the suspension of CNF before the solvent is removed. In suspension casting, material is contained within the casting dish and is dried and concentrated uniformly, however evaporation times can be quite long.

With vacuum filtration there are potential obstacles to overcome when making nanocomposite films. With pure CNF films, a significant amount of material is lost and for smaller components within the composite, such as polymer chains or small nanoparticles, an even larger amount can be lost. The CNF can form a fiber mat that prevents the loss of excess material, but other components in a nanocomposite may not be trapped by this network or may be lost at a higher rate than CNF. This not only makes the fabrication method less efficient as more material is required for production, it also means one cannot be confident in the relative amounts of the nanocomposite components present in the final film. Additional characterization would be necessary to determine the final composition in the nanocomposite. Because there is a gradient in the concentration for vacuum filtration, this could also result in

an uneven distribution of nanocomposite components, depending on how it interacts with the nanofiber network.

Due to the remarkably high stiffness of CNF, often the goal for CNF-based nanocomposites is as a fiber reinforcement for a more ductile polymer matrix. One example incorporates a cellulose derivative, hydroxyethyl cellulose (HEC), into a CNF-based nanocomposite using vacuum filtration and a heated vacuum drying process. The resulting composite exhibited interesting mechanical behavior, which is shown in Figure 4.2. At relatively low percentages of HEC, the overall stiff nature of the films was maintained but the point of fracture was suppressed, allowing for increased elongation and tensile strength. The softer HEC helps to plasticize the CNF and improves the overall toughness. Additionally, a secondary yield point is present, which could indicate the point where the primary hydrogen bonding of the CNF network begins to fail. The deformation region after the secondary yield point is governed by the relatively low modulus of the matrix polymer.

In a related study, the effect of overall polymer stiffness and glass transition temperature (T_g) was tested by using two different matrix polymer CNF-based nanocomposites. The first is poly(N,N-dimethylacrylamide) (DMAm) and has a T_g of approximately 130 °C, making it a relatively stiff polymer. The second polymer is poly[(ethylene glycol methyl ether methacrylate)-co-N,N-dimethylacrylamide] ($EG_{54}DMAm_{46}$) which has a T_g of roughly 26 °C and a lower modulus than DMAm. Nanocomposite films were fabricated at compositions between 0 and 50% matrix polymer and mechanical properties were measured [127].

The stress-strain curves of the nanocomposite containing DMAm are shown in Figure

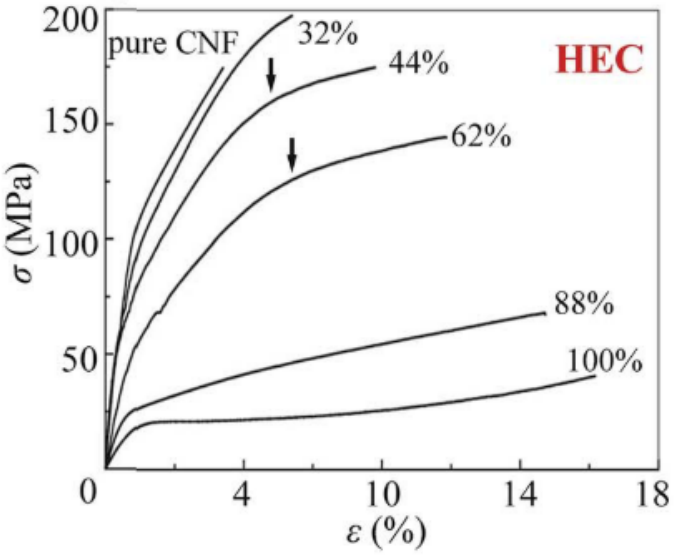

Figure 4.2: Stress-strain curves showing the mechanical behavior of CNF and HEC nanocomposite at a range of compositions [126]. © 2011

4.3a. As the DMAm concentration increases the stiffness immediately decreases, but the percent elongation remains roughly constant. The overall behavior of the curves mimics the pure CNF film in that the initial linear elastic region reaches the yield point at roughly the same strain, followed by an extended plastic deformation region until the film fractures. The stiffness continues to decrease upon increasing DMAm concentration and the tensile strength and overall toughness decrease. The mechanical behavior of the nanocomposite film containing $EG_{54}DMAm_{46}$, shown in Figure 4.3b, is different. Again, as the matrix polymer concentration increases the stiffness begins to decrease, though the decrease is larger than for DMAm. The major difference is in the percent elongation, as this value increases as the matrix polymer concentration increases, from about 5% up to about 22% strain. The composites reach a slightly higher tensile stress with more brittle behavior which also results in a higher toughness. Additionally, the two arrows on Figure 4.3b point to a secondary yield point observed at high matrix polymer composition [127].

In both nanocomposites the presence of the matrix polymer results in a decrease in

stiffness. In the case of $EG_{54}DMAm_{46}$, a more ductile polymer, the CNF network fails (at the initial yield point around 1% strain), and the lower stiffness of the matrix polymer allows the film to continue to deform. This results in larger elongation, tensile strength, and toughness. However, with DMAm as the matrix polymer, the high stiffness prevents interfibrillar motion during deformation. This results in a more brittle failure governed by CNF. Despite using a higher stiffness matrix polymer, the mechanical performance was ultimately less stiff than that for the more ductile polymer.

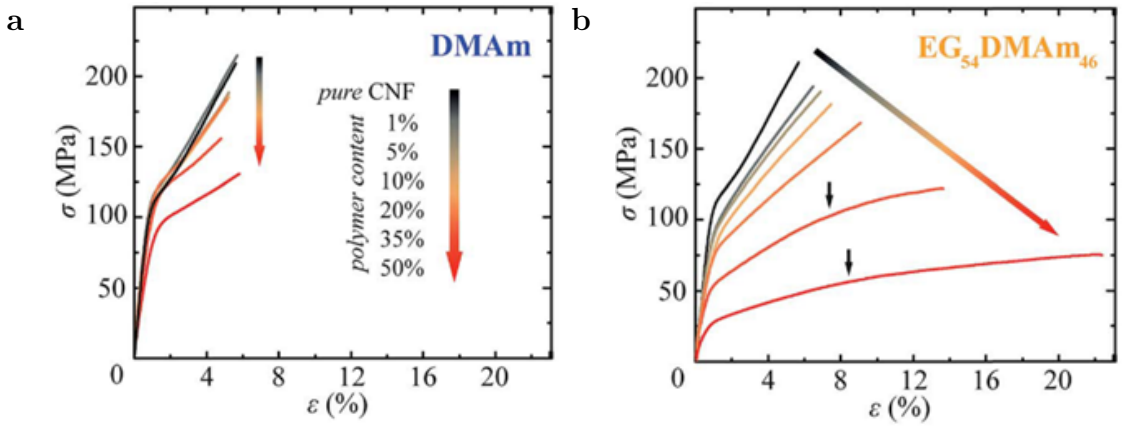

Figure 4.3: Stress-strain curves showing the mechanical behavior of a) nanocomposites from CNF and DMAm and b) nanocomposites from CNF and $EG_{54}DMAm_{46}$ copolymer at increasing matrix polymer content [127]. © 2016

One avenue for CNF nanocomposites of particular interest is when the matrix polymer can interact with the network of CNF. One such nanocomposite system was investigated by Kurihara et. al., in which CNF was combined with poly(acrylamide) (PAM). PAM was chosen as a matrix polymer due to the presence of C=O bonds and NH_2 groups, which can both form hydrogen bonds with the cellulose hydroxyl groups. Nanocomposites were formed by mixing aqueous solutions of PAM with aqueous suspensions of CNF and films were fabricated by solvent casting and drying at 40 °C for 2 days. The resulting mechanical properties, shown in Figure 4.4, exhibited a slight increase in stiffness and

tensile strength between 0 and 20% PAM, followed by a decrease between 20 and 100% PAM. The elongation at break shows an unusual trend of decreasing from 0-50% then increasing with PAM content. Toughness decreases with PAM content. Additionally, CNF (termed TOCN in the figures) was incorporated into the composites having both $-COONa$ and $-COOH$ groups in order to determine its effect on the mechanical properties [14, 128].

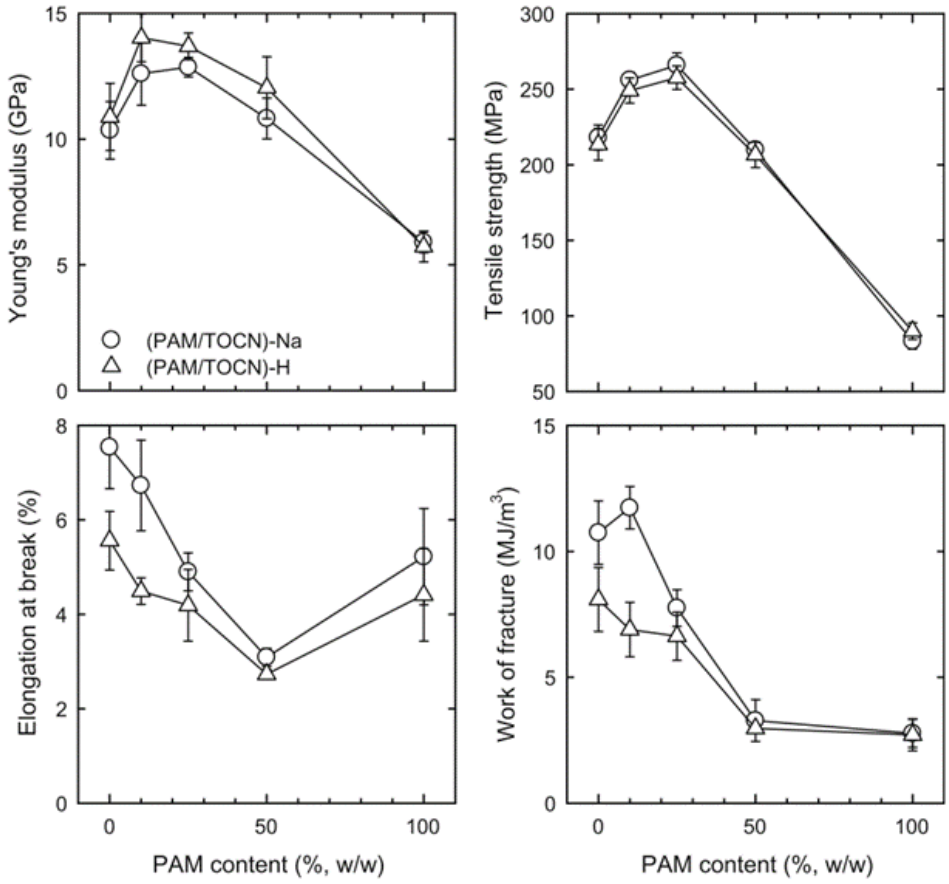

Figure 4.4: Tensile testing results of CNF/PAM nanocomposites showing the Young's modulus, elongation at break, tensile strength, and work of fracture. The results of nanocomposites containing both $-COONa$ and $-COOH$ groups [14]. © 2002

The mechanism for this variation in properties is particularly interesting, as it is expected that PAM can form hydrogen bonds with CNF, and $-COOH$ groups are expected to improve the level of hydrogen bonding within neat CNF films. It was found that the

carboxylate ion, either H or Na, did not have a significant effect on the resulting mechanical properties. Kurihara et. al. claim that the mechanism of the increase in stiffness and strength up to 20% PAM is due to the ability of CNF to form self-aligned and nematically ordered structures in suspension as a result of electrostatic repulsion. (de Nooy et al., 1995) The limited amount of PAM is present between these randomly distributed domains, resulting in improved stiffness and strength. FTIR shows the formation of hydrogen bonds between the PAM and $-COOH$ groups of cellulose, but this does not explain the observed increase in stiffness and strength. (Nishiyama et al., 2000) While PAM presenting a self-aligned network of CNF can explain this increase, it is likely that the hydrogen bonding between cellulose hydroxyl groups and PAM plays a significant role as well. A similar mechanical effect is observed in composites of cellulose and soy protein isolate. If the soy protein is treated and denatured, the internal hydrogen bonding sites become available and can interact with cellulose systems, such as a pad of bacterial cellulose. The interaction through hydrogen bonding produces a similar increase in stiffness with limited inclusion of soy protein [129, 130]. The ability of these materials to hydrogen bond with cellulose set them apart from other composites that were reported in the literature.

In a review written by Wang et. al. a variety of cellulose based composite systems are discussed. One example is cellulose and polyvinyl alcohol (PVOH) composites, since PVOH is a water soluble polymer having free hydroxyl groups. Figure 4.5 shows the tensile strength and modulus of a collection of cellulose and PVOH composite systems in all forms, including electrospun fiber mats, hydrogels, films, and fibers. The plot illustrates that the form of the composite has an inherent effect on the resulting properties, and that the range of properties of the standard composite films is roughly a tensile strength of between 5-200 MPa, and tensile modulus of between 0.2-10 GPa [131].

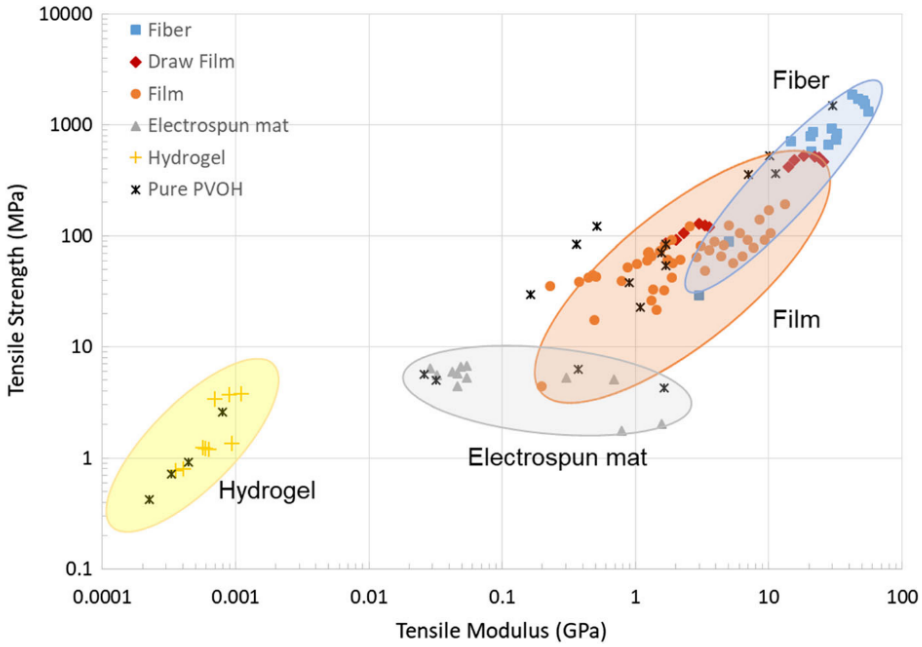

Figure 4.5: Range of mechanical properties from a variety of cellulose composite materials, including films, fibers, hydrogels, and mats [131]. © 2021

4.2.4 Summary of all-cellulose composites

The idea of an all-cellulose composite is driven primarily by its ability to form hydrogen bonds between cellulose chains. Therefore, a composite of two different allomorphs or geometries with varying properties could be fabricated but there would be no coupling or surface modification required in order to generate an interaction between them. Due to the one-dimensional nature of many cellulosic materials such as MFC, CNF, or CNC, this can result in directionally reinforced nanocomposites with unique interactions between the filler and matrix of the nanocomposite.

One method of creating all-cellulose composites is a one-step process achieved through partial dissolution, in which a solvent is used to partially dissolve a fibrous morphology of cellulose, then the solvent is removed, leaving a matrix of regenerated cellulose with embedded cellulose fibers [132–137]. A schematic illustrating this method is shown in

Figure 4.6a. The filler can be any fibrous form of cellulose, from large scale cellulose macrofibers to CNF or CNC. More information about the solvents that can be used to partially or selectively dissolve the fibrous component can be found in Chapter 3 of this thesis, which provides background on dissolving cellulose.

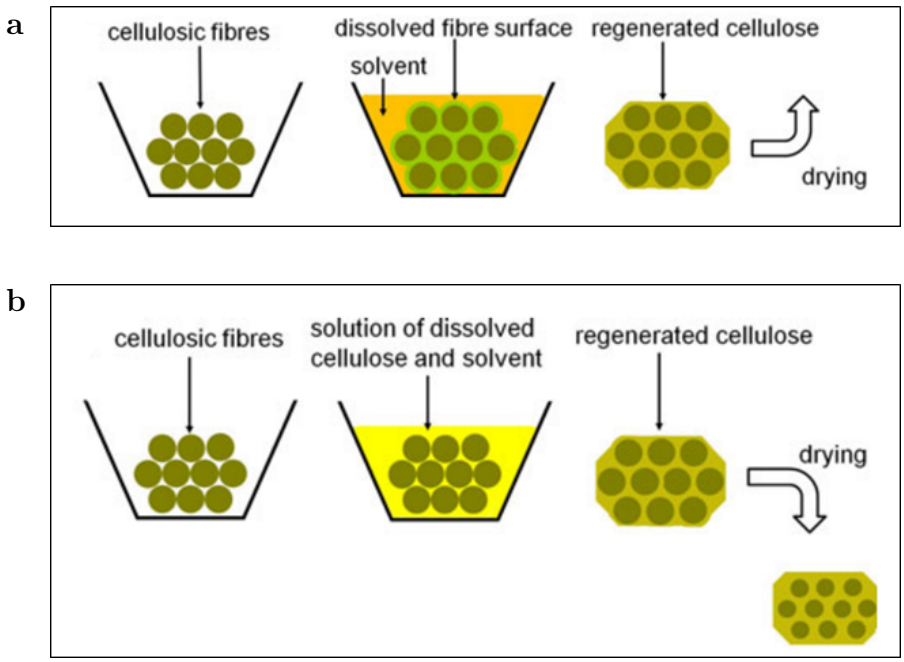

Figure 4.6: Schematics showing two different methods of preparing fiber-based all-cellulose nanocomposites. a) One-step method involving partial dissolution of cellulose fibers followed by regeneration, and b) two-step method in which cellulose fibers are combined with a solution of cellulose which is then regenerated around them [132].

In work done by Ma et al., for example, CNC, is immersed and heated in ionic liquid, partially dissolving the nanocrystals, and added to a solution of alkali cellulose and ionic liquid. The ionic liquid is removed from the mixture by washing with water and drying, resulting in transparent all-cellulose nanocomposite films. The resulting films varied by the initial amount of CNC that was added. The relative amounts of CNC that were dissolved were determined by XRD, identifying relative crystallinities of cellulose I

and II crystal structures in the films. The films underwent tensile testing, the results of which are presented in Figure 4.7. The stiffness increases with an increase in CNC content, and a clear optimization can be observed at roughly 10%, in which a high tensile strength, percent elongation, and toughness are all achieved. This tunability between plastic and ductile versus stiff and brittle behavior illustrates the advantages of reinforced all-cellulose composites. (Ma et al., 2011) While some tunable mechanical behavior was achieved, there are disadvantages to this partial dissolution method. It is difficult to determine how much of each cellulose component is present in each sample. While this can be inferred through methods like XRD or FTIR, it is difficult to be confident in the relative compositions of each component. Additionally, the partial dissolution of CNC could weaken the properties of individual nanoparticles by damaging crystal structures.

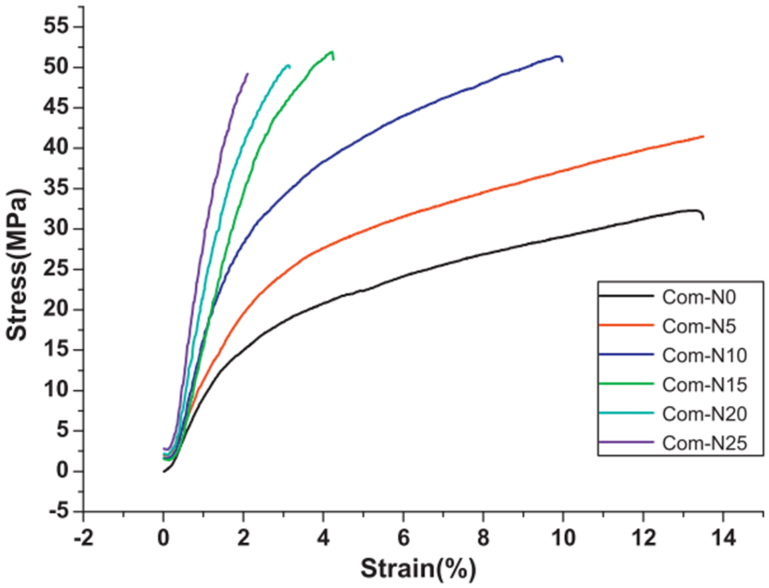

Figure 4.7: Tensile testing results showing the effect of CNC composition on mechanical behavior [134]. © 2011

Another method for producing all-cellulose composites is a process of solution infiltration, in which one cellulose component is fully dissolved, then regenerated in the

presence of an undissolved fibrous cellulose component, as shown in Figure 4.6b [132]. This can provide more control over the exact concentrations of each component, and is potentially better for understanding the interactions between components. One example of this method is by Yang et. al., where TEMPO oxidized CNF were combined with regenerated cellulose from the alkali-urea solvent system described in Chapter 3. The results showed an increase in the stiffness and strength of the regenerated cellulose films upon the introduction of CNF, as shown in Figure 4.8. Remarkably low CNF compositions were required to achieve improvements in mechanical properties, likely due to the high length of individual nanofibers. These films also exhibit two different crystal structures, as the CNF contains cellulose I, but the regenerated matrix cellulose contains cellulose II, which is typical for cellulose regenerated from solution [138]. However, while solution infiltration can be useful in identifying interactions within a composite, these reports have focused primarily on the matrix-rich composition region of all-cellulose composites, in which a small amount of a fibrous component provides composite reinforcement.

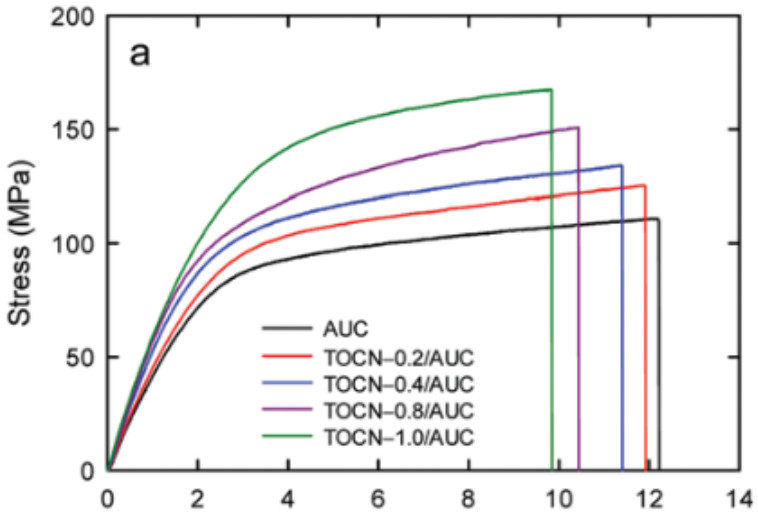

Figure 4.8: Stress-strain curves from tensile testing results of all-cellulose nanocomposites made from TOCN and cellulose regenerated from an alkali-urea dissolved cellulose (AUC) [138]. © 2015

4.2.5 All-cellulose composite- motivation and explanation

The goal of this work is to combine the two cellulose systems discussed in chapters 2 and 3, CNF and MCS, into a single self-reinforced all-cellulose nanocomposite. Both cellulose systems represent basic fundamental cellulose structures, for CNF it is the most naturally occurring elementary cellulose structure, and MCS the basic chemical species of cellulose, polymer chains. Therefore, these two systems should create a situation where the interactions of each form of cellulose can be understood. Due to the water-resistant properties of cellulose films cast from MCS, and the nature of cellulose to form hydrogen bonds with itself, it is expected that the addition of MCS to CNF films will reduce overall water uptake. Additionally, the system will be examined to determine the mechanical properties with a potentially wide range of tunability. By investigating a full range of compositions, this work provides a new understanding of cellulose interaction within all-cellulose composites.

For each cellulose system there are many variables that can alter the properties and structures of the resulting cellulose. These have been optimized for the purpose of forming nanocomposites as discussed in this section.

4.2.5.1 Optimizing CNF for nanocomposite applications

The first step to adapting CNF for nanocomposites with MCS is to replace the water in the CNF suspension. If MCS is added to water the dissolved cellulose will immediately precipitate, which would prevent adequate dispersion for nanocomposite production. The water in the CNF suspension is exchanged for DMSO, which has been shown to allow good dispersion of the CNF. A rotary evaporator was used to scale up the process. This will

allow the suspension to be mixed with the MCS without flocculation and precipitation.

After the TEMPO-oxidation process, cellulose must be mechanically homogenized to produce CNF. Homogenization in this work is conducted using a high pressure microfluidizer. The number of times the pulp is run through the microfluidizer has been shown to reduce the length and variability, resulting in a more monodisperse length distribution, which is helpful for understanding the resulting mechanical properties. The CNF after 4 passes through the microfluidizer was shown to have an adequately uniform distribution of length between 200-400 nm, and diameter about 2 nm as determined from AFM measurements discussed in Chapter 2. Aspect ratios of roughly 100 were still obtained despite reducing the length considerably, so the CNF is still capable of significant composite reinforcement.

Once the CNF is dispersed in DMSO the concentration at which the suspension will form a gel is lowered and shortening the lengths of the CNF allows for greater concentrations while still allowing for a fluid suspension. Gelation would be detrimental and make the nanocomposite much more difficult to mix, but increased concentration is important for reducing the amount of solvent that must be removed, as this is a time- and energy-intensive process. Through optimization of the solvent exchange and evaporation process, a suspension as high as 0.11 mol% CNF in DMSO was produced without forming a gel.

4.2.5.2 Optimizing MCS for nanocomposite applications

One factor that must be considered for MCS used to form nanocomposites is the cellulose concentration. The concentration must be high enough to minimize the volume of solvent that must be removed, but must remain low enough that the MCS can be mixed and combined with CNF and allow the mixture to remain fluid so it can be cast to form films. This concentration was found to be roughly 3 mol% cellulose in solution.

The other significant factor is IL concentration. In order to dissolve cellulose it has been shown that a minimum concentration of IL is required, resulting in the ions associating with the cellulose and occupying hydrogen bonding sites. With an excess of IL, combining the MCS with CNF would result in a larger amount of IL interacting with CNF. This could cause flocculation due to charge interactions between the $-COONa$ surface groups and the dissociated ions from EMIMAc. This interaction could also potentially allow the IL to partially dissolve the CNF, which could compromise mechanical properties of the resulting nanocomposites.

To address this issue, the MCS was formed with the goal of minimizing IL content. After mixing the Avicel and DMSO, IL is added in small amounts and stirred vigorously. Additionally, between each addition of IL, the solution is heated in a 90 °C oven for 5 minutes to test for dissolution. The MCS was checked for dissolution by eye, since undissolved Avicel powder is visible. When the solution was fully dissolved, the final cellulose, IL, and DMSO compositions were 3.2, 5.3, and 91.5% respectively by mole, resulting in an IL to cellulose molar ratio of roughly 1.7:1. This is quite close to the lowest soluble ratio achieved in Chapter 3 at about 1.66:1, and should result in limited interaction between CNF and IL.

4.2.6 All-cellulose nanocomposite fabrication

Combining CNF and MCS to form composite mixtures is accomplished by slowly adding MCS into a suspension of CNF in DMSO in a centrifuge tube and mixing with a Vortex stirrer until the mixture flows homogeneously. Both the CNF suspension and MCS solution are viscous, and the mixture is also quite viscous. After mixing, bubbles are removed before evaporation by partially submerging the tube in a sonication bath. The

mixture will form a loose gel if it remains undisturbed for more than a few seconds, similar to the gelation behavior of CNF suspensions but occurring much more quickly. Sonication must be done while constantly rotating or agitating the tube so the mixture remains fluid. Once the bubbles are removed, the mixture is immediately poured into a casting dish.

The casting dish used was the same used for creating dense cellulose and EMIMAc gels in Chapter 3, with Teflon sides secured onto a glass base. This design allows the film to evaporate evenly from the top-down without the film clinging to the side of the dish as it dries. This results in relatively even film thickness from the center to the edge of the film.

In fabricating nanocomposites, the drying method must also be considered. Filtering the composite mixture into a gel then hot-pressing would result in slightly improved mechanical performance and take less time to remove DMSO, but the MCS may fall through the micropore filter. In testing, it was estimated that some of the solution remained present in the condensed gel after filtering, but it became far too difficult to determine how much of each type of cellulose was present in the final film. Solvent casting was determined to be the best option for nanocomposite film fabrication. The DMSO was removed via evaporation in a vacuum oven. The temperature must be low enough that the cellulose and IL do not degrade over time since evaporation will take 3-4 days. The evaporation termperature used was 50 °C. The vacuum must be low enough that the DMSO does not boil and the solvent is evaporated evenly, resulting in a consistent thickness across the films. After testing a vacuum of approximately 11 inHg was used.

The final step in producing the nanocomposite films is removing IL. The same protocol will be followed that was employed to produce dense gels of cellulose and IL in chapter 3, which formed amorphous cellulose. The amorphous cellulose has shown

significant water-resistance and should enable further interaction with the CNF compared to a more ordered crystalline structure.

4.3 Experimental methods

4.3.1 Cellulose nanofiber preparation

Cellulose pulp from southern yellow pine wood was used for this study. The moisture content of the pulp was about 5%. Cellulose nanofiber production was carried out according to the TEMPO oxidation procedure described in Chapter 2, followed by thorough cleaning and resulting in a suspension of TEMPO-oxidized cellulose pulp in water at about 1% by weight before homogenization. Mechanical homogenization was conducted using a NanoDeBEE microfluidizer from BEE International. Homogenization was carried out at roughly 200 kPa (30 kpsi) and the material was passed through the machine four times. CNF suspensions were then purified by centrifugation to remove any remaining unhomogenized cellulose material. CNF then underwent a solvent exchange to replace the water in the suspension with DMSO. The CNF suspension in water with concentration of about 0.6% was added to an equal volume of DMSO and stirred gently until homogeneous. Water was removed using a rotary evaporator, in which the suspension kept in a water bath at about 60 °C, and vacuum was increased until just before the suspension began to boil. Once the suspension had been evaporated by half it was removed, then the process was repeated two more times. The resulting suspension of CNF in DMSO was stored in a desiccated environment to prevent exposure to moisture, and concentration was confirmed to be 0.11 mol% (0.6 wt%) CNF by evaporation.

4.3.2 Molecular cellulose solution fabrication

Avicel cellulose powder was combined with DMSO and briefly stirred. EMIMAc was added in small amounts, followed by vigorous stirring, and heating at 90 °C for about 5 minutes. EMIMAc was added, followed by 5 minutes of heating and stirring, until the solution was fully transparent. The solution was confirmed to be dissolved if when held up to the light no Avicel powder particles are observed. The final compositions of cellulose, IL, and DMSO were 6.1, 10.6, and 86.3% by weight, respectively.

4.3.3 All-cellulose composite fabrication

CNF suspension in DMSO was poured into a large centrifuge tube. MCS was added slowly into the CNF under constant stirring, then stirred vigorously for 60 seconds. Bubbles were removed from the composite mixture by briefly sonicating while maintaining flow in the liquid mixture, then the mixture was deposited into a casting dish with Teflon sides and a glass base.

The composite mixtures were dried in a vacuum oven at 50 °C and a vacuum of 37 kPa. Once the DMSO appeared to be fully evaporated, vacuum was increased to 30 inHg and the films were left to dry for 12 hours longer to ensure full removal of DMSO.

IL was removed from the nanocomposite films by soaking in acetone, followed by ethanol. Films were first soaked in acetone for 1 day, then dried for 2 hours in a vacuum oven, then soaked again in a bath of fresh acetone for 1 more day. Films were then soaked in ethanol following the same protocol, and soaking continued until IL was fully removed. Total mass of the film was monitored before and after each stage of soaking to track the removal of IL, and stopped when no change in mass was observed.

4.3.4 Atomic force microscopy

Suspensions of CNF in DMSO and MCS were both diluted to about 0.2 mol%. The two were mixed at a 50/50 ratio and stirred thoroughly. The resulting mixture was cast onto a freshly cleaned silicon wafer, spincast, then dried in the oven to evaporate DMSO. The film was then soaked in acetone and ethanol in stages to fully remove IL, then dried in the oven. AFM was conducted in tapping mode on the thin film using a Multimode AFM from Nanoscope.

4.3.5 Transmission and Haze

Light transmission was measured using the Lamda 1050 device from Perkin Elmer with a 150 mm integrating sphere. Baseline transmission measurements between wavelengths of 400 and 800 nm at a resolution of 5 nm per minute. Haze was measured by measuring reflective transmission and dividing by the baseline transmission for each sample.

4.3.6 Tensile testing

Tensile testing measurements were conducted using a DMA Q800 from TA Instruments. While a DMA is typically used for viscoelasticity measurements, in this work it was used for standard tensile testing. Force ramp tests were run for each sample at a rate of 1 N/min, with at least 3 successful tensile measurements taken for each sample. Samples for tensile testing were prepared by cutting a rectangular shaped piece from the film roughly 3-4 mm wide and the length of roughly 20-30 mm. To ensure successful tests, freshly sharpened hole punches were used to cut circular portions from the sides of the sample center, creating an approximate "I" shape so failure occurred at the center. If the cutter

was not sharp enough there could be small microcracks that could form at the cutting site, which could result in premature failure of the test. Thickness and width were measured before and after each measurement to ensure accuracy and account for any changes in dimension due to high strain.

4.3.7 Scanning electron microscopy

Images were taken using a Hitachi SU-70 FEG SEM from the University of Maryland Advanced Imaging and Microscopy Lab with an acceleration voltage of 0.7 kV and a working distance of about 15 mm. The films from select tensile testing measurements were taken for fracture surface imaging with SEM. The films were loaded onto a vertical sample holder, to observe the cross section of each fracture surface and coated with a thin layer of carbon.

4.3.8 Water uptake

Water uptake was measured by cutting a circle of each film 1 cm in diameter and weighing using a microbalance. For each measurement the film was placed in a shallow water dish and submerged for a set amount of time, after which the film was retrieved, briefly patted with a Kim wipe, and weighed again.

For some films, after about 10 minutes the films begin to disintegrate, and the measurement could not be continued.

4.4 Results and discussion

4.4.1 Atomic force microscopy

A proposed schematic illustrating the potential morphology of the all-cellulose nanocomposite films, featuring a network of CNF embedded in a matrix of regenerated cellulose from MCS is shown in Figure 4.9a. Diluted CNF suspensions in DMSO and MCS solutions were combined and spin cast in order to determine if the cellulose components were aggregating upon mixing. Figure 4.9b shows an AFM image of the spin cast 50% CNF/50% molecular cellulose (Optimizing MCS for nanocomposite applications) nanocomposite thin film. The image shows the MCS regenerated as small particles of cellulose, covering the silicon wafer. Individualized CNF is shown distributed throughout the layer of MC, indicating that neither cellulose component aggregated upon mixing the nanocomposite.

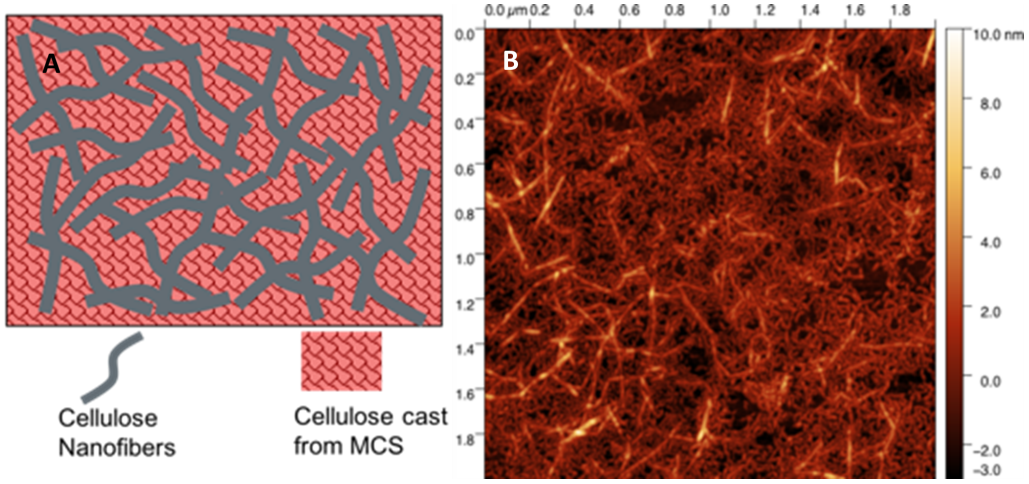

Figure 4.9: a) Proposed schematic of all cellulose composite. b) Spin-coated thin film of all-cellulose nanocomposite mixture.

4.4.2 Hazemeter measurements

Baseline and reflective transmission measurements were taken for each nanocomposite film and are shown in Figure 4.10. Baseline transmission (transmission 1) measurements are consistent for each film between about 85 and 90%, with no discernable trend as a function of MC content. This agrees with transmission values from the literature for pure CNF films [52, 64, 67] and pure amorphous MC cellulose films [110] both at around 90%. Reflective transmission (transmission 2) measurements show an overall increasing trend with MC content. Where pure CNF films have values of about 8%, some nanocomposites and the pure MC films have reflective transmissions as high as 30 or 35%. Each reflective transmission measurement also follows the trend of increasing as wavelength decreases, with this behavior becoming more pronounced with increasing MC content as well.

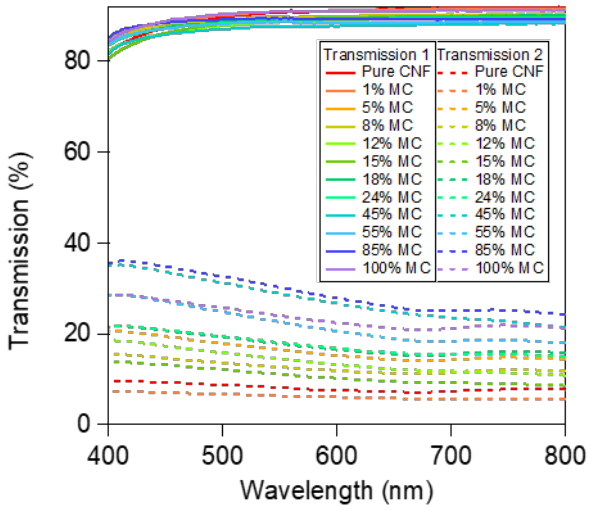

Figure 4.10: Baseline and reflective transmission (transmission 1 and 2) measurements of each all-cellulose nanocomposite film.

Haze is a property that quantifies how strongly light is scattered through a material. This is calculated by dividing the reflected transmission by the baseline transmission. The haze measurement for each composite sample is shown in Figure 4.11 Because the baseline

transmission values are relatively constant with respect to wavelength and are close to 100%, the haze values are very similar to the reflective transmission values.

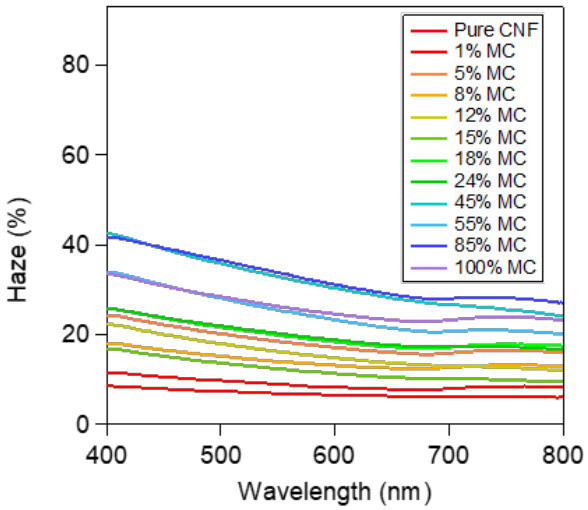

Figure 4.11: Haze percent as a function of wavelength for each composite film

Figure 4.12 shows this haze, averaged across all wavelengths, and plotted as a function of MC content. For pure CNF films, the haze is about 8%. With increasing MC content the haze increases quickly before leveling out between 24 and 45% MC and approaching a value of about 30%. While there is some variability, there is a clear trend of increasing haze with increasing MC content that levels out at higher MC concentrations.

The haze of pure CNF is fairly low, around 8%, which is in agreement with haze values for CNF found in the literature [68, 139]. This minimal haze is derived from small amounts of air trapped in the CNF dispersion during the drying process, producing voids in the film that scatter light. With careful drying, or filtering and pressing, haze can be reduced to around 4%. As the MC composition is increased, the amount of haze in the film quickly increases, but the source of this haze is unknown. Crystallinity in pure MC films is minimal, so crystallization is not a likely source of haze. One possibility is that the haze in MC is also caused by voids, similar to CNF. In Chapter 3, the ethanol soaking process for

the cellulose and EMIMAc gels was discussed. The SAXS results showed that immediately after ethanol soaking begins, the intensity increases significantly. This increase in scattering could also indicate the presence of voids. These voids could be forming upon the removal of EMIMAc during the second stage of washing using ethanol, but the surrounding cellulose in the system is too stiff to relax, resulting in voids.

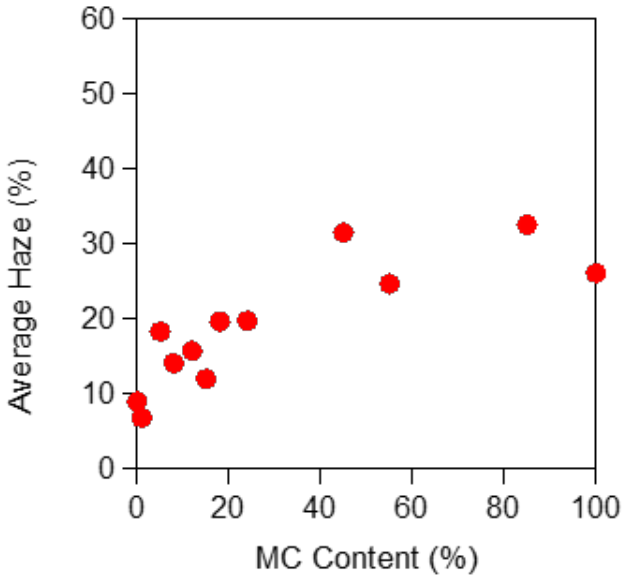

Figure 4.12: Optical haze plotted as a function of MC content. Haze was calculated by averaging haze values across all wavelengths.

4.4.3 Tensile testing

The first method employed to understand the interaction between MC and CNF in the nanocomposites was tensile testing. The tensile behavior of the pure CNF films is the red curve shown in Figure 4.13. In composite samples containing low concentrations of MC, the samples fracture more quickly but have a steeper initial slope, resulting in a stiffer but more brittle film with a shorter plastic deformation region. As MC concentration continues to increase, the slope decreases and elongation increases, where at roughly 70%

MC the film appears to have similar mechanical behavior to the neat CNF film. As MC content further increases the initial slope continues to decrease, and elongation increases substantially. At 100% MC the film deforms very plastically, having the lowest slope and largest elongation of all measured samples.

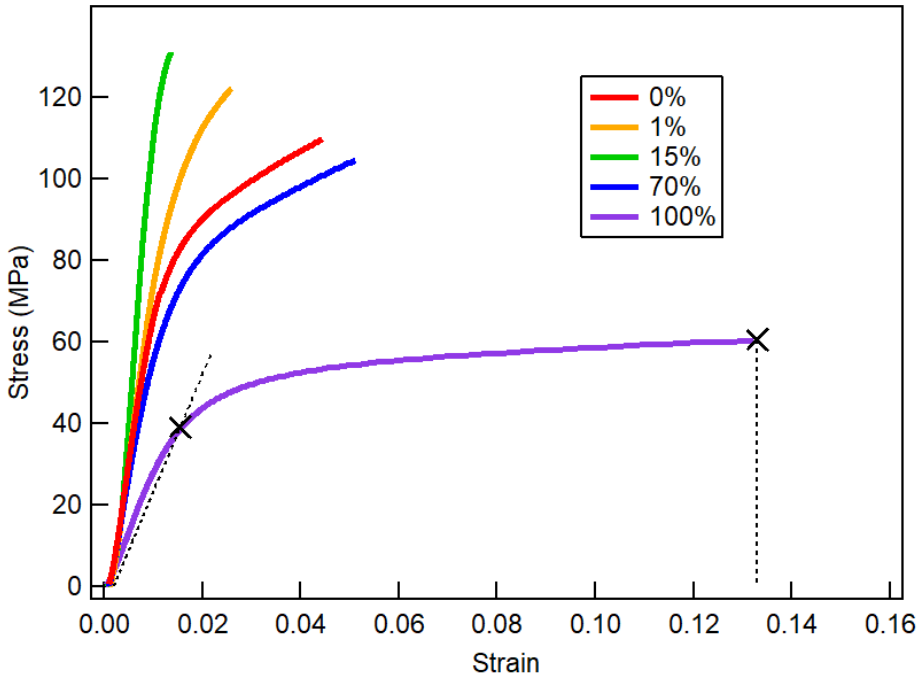

Figure 4.13: Stress-strain curves of select all-cellulose nanocomposite samples illustrating the different mechanical behaviors of all-cellulose nanocomposites with varying MC content. A sample line of 0.2% strain offset is drawn onto the 100% MC data to illustrate how yield strength was calculated, and a line is drawn establishing the elongation at break at the end of the curve.

The modulus, percent elongation, yield strength, and toughness were calculated based on the mechanical testing. Yield strength was calculated based on the 0.2% offset from the linear elastic region, and toughness was calculated from the area under the curve. The modulus of pure CNF is 8.5 GPa, which agrees with values reported in the literature which range between about 6-12 GPa, however the yield strength is significantly lower that the reported values [52, 140]. This is likely due to the CNF in this work having shorter lengths. Longer lengths allow for greater entanglement and breaking and reforming of

hydrogen bonds during plastic deformation [65]. Additionally, the nanofibers in the CNF film could be damaged from the excessive mechanical treatment applied in this work. This could also explain the lower yield strength. This could also explain the percent elongation being less than reported values.

The mechanical behavior of the pure MC film exhibits largely plastic deformation. Modulus and yield strength values are much lower than those of CNF at around 2 GPa and 40 MPa respectively, while the elongation at break is high, around 8%, and the toughness is also high. Table 4.1 shows a comparison of mechanical properties between cellulose obtained from MCS, versus cellulose obtained from solutions in pure ionic liquids, EMIMAc and 1-allyl-3-methylimidazolium chloride (AMIMCl). The cellulose obtained from pure ionic liquid solutions contains a significant amount of cellulose II crystallinity [102], while MC is almost fully amorphous. This explains why MCS has a lower stiffness and a larger elongation, as the crystallinity makes the cellulose from EMIMAc and AMIMCl less ductile.

Solvent	**Young's modulus (GPa)**	**Tensile strength (MPa)**	**Elongation at break (%)**
EMIMAc	3.1-5.5	35-48	0.5-2.6
AMIMCl	5.1-7.1	78-120	2.1-5.6
MCS	**2.2**	**54.4**	**7.5**

Table 4.1: Mechanical properties displayed by cellulose samples from different solvents: two ionic liquids EMIMAc and AMIMCl [102], and the MCS described in this work.

It is shown in Figures 4.14a and 4.14b that the Young's modulus and yield strength follow a similar trend as both increase with MC up to about 20% MC, then begin to decrease almost linearly with MC, until 100% MC. The Young's modulus follows this trend, and while the yield strength data shows considerable variability, it also appears to follow this trend. An opposite trend can be observed in Figures 4.14c and 4.14d, as the percent

elongation and toughness both decrease initially with limited MC content up to about 20%, then increase almost linearly up to 100% MC. While there is some variability in the samples as evidenced by the error bars, the overall trend for each property is clear.

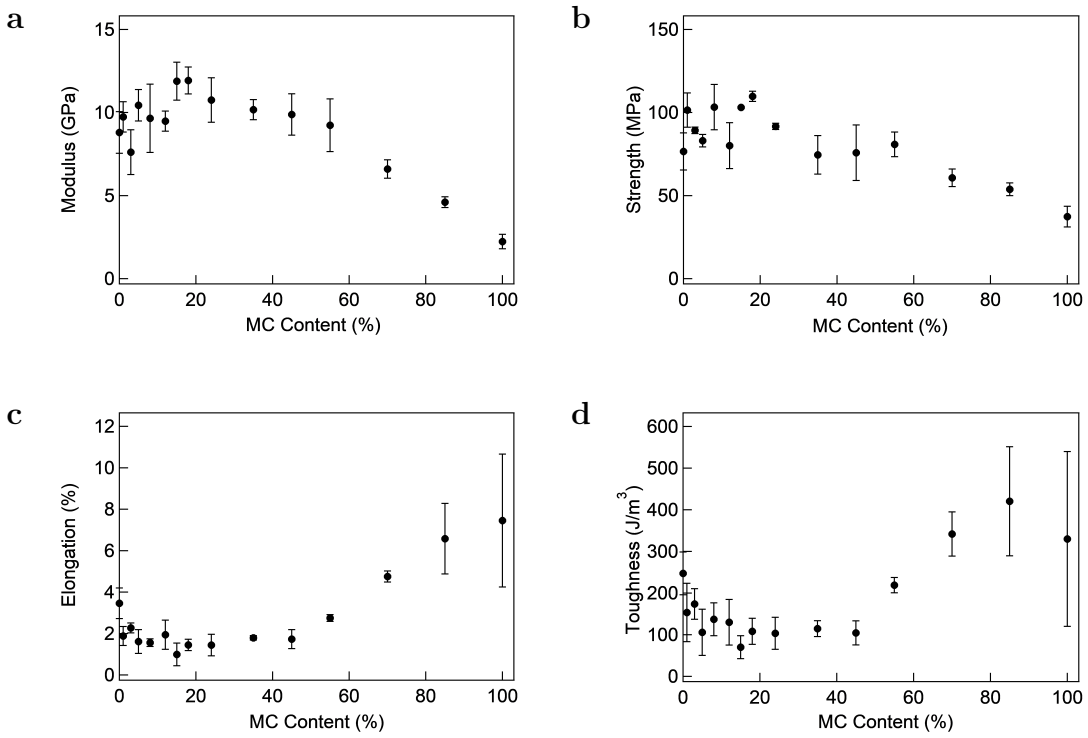

Figure 4.14: a) Young's modulus, b) yield strength (measured from 0.2% strain offset), c) percent elongation at failure, and d) toughness plotted against MC content.

The mechanism driving the mechanical behavior of CNF is hydrogen bonding between entangled nanofibers, combined with the intrinsic stiffness of the semicrystalline fibers. Once the film begins to yield, hydrogen bonds between nanofibers break and reform, allowing for the film to maintain stiffness throughout plastic deformation. This extends the plastic deformation region and allows for higher toughness overall [65]. In the nanocomposite samples, despite the low stiffness of neat MC films, there is an increase in stiffness observed after adding a limited amount to nanofiber composites. This results in a larger yield strength as well, but also limits the ability of the film to plastically deform, as

the elongation and toughness are decreased.

Similar behavior was observed in a CNF-based nanocomposite with PAM as described in Figure 4.4, or in composites of cellulose with soy protein isolate [129, 130]. These composite films also display an increased stiffness and strength with a limited inclusion of the matrix polymer, in this case roughly 25% PAM. The key similarity between these two systems is the inclusion of a matrix polymer capable of forming hydrogen bonds with CNF, allowing for a self-reinforced nanocomposite. While this indicates the presence of favorable hydrogen bonding interactions, the exact mechanism for how this interaction results in the given mechanical behavior is unclear. A possible mechanism for this behavior is the MC is acting as a reinforcement, forming hydrogen bonds with surrounding nanofibers. This can reinforce contact points in the CNF network and act as a reinforcing agent and improves mechanical properties. It also appears to limit the elongation at break and toughness. This indicates while the network has been strengthened, the mechanism of CNF breaking and reforming hydrogen bonds, thereby extending the plastic deformation region, no longer applies.

By testing a full range of composition from 0 to 100% MC, a range of tunable mechanical properties were achieved with the all cellulose nanocomposites, having a modulus between 2.2-11.9 GPa and yield strength between 55-110 MPa. This range in tunability is consistent with ranges of other polymer composites based on cellulose nanomaterials, such as with polyvinyl alcohol or polypropylene [131], as well as ranges of other isotropic and nonwoven ACCs [132, 133].

4.4.4 Scanning electron microscopy

SEM images for 3 cellulose films are shown in Figure 4.15, with the cross-sections of the films fracture surfaces after tensile testing in which the vertical direction is oriented along the 2-dimensional plane of the film, and the horizontal direction is oriented with the film thickness. Figures 4.15a and 4.15b show a CNF film with no MC included, Figures 4.15c and 4.15d show a nanocomposite film with 15% MC, and Figures 4.15e and 4.15f show a 100% MC film. In Figure 4.15a, a structure oriented in the plane of the film is visible. The higher-magnification image in Figure 4.15b shows dark areas amidst the oriented structure, and a large gap between layers in which bridging nanofibers can be observed. In Figure 4.15c and 4.15d, a similar structure oriented in the plane of the 15% MC film is present, but with a lower contrast difference than in the 0% film, which could indicate lower roughness in the fracture surface. While there are similar dark areas present in Figure 4.15d as are visible in 4.15b, they appear smaller, and no larger gaps are visible. Figure 4.15e shows a fracture surface with round structures with protruding edges in the 100% MC film. In the inset image in Figure 4.15f, tears within the crater structures are visible.

SEM images shown in Figure 4.15 can provide insight into the mechanical behavior of these films. Figure 4.15c shows crater-like structures, which is evidence of a ductile fracture after significant plastic deformation. Figures 4.15a and 4.15c show a semi-ordered or layered structure characteristic of CNF films [141], with the layered structure in 4.15a appearing rougher and more protruded from the surface as compared to 4.15c based on greater changes in contrast along the surface. The 15% MC film shown in 4.15c showed more brittle behavior with a higher stiffness and lower elongation, which would result in

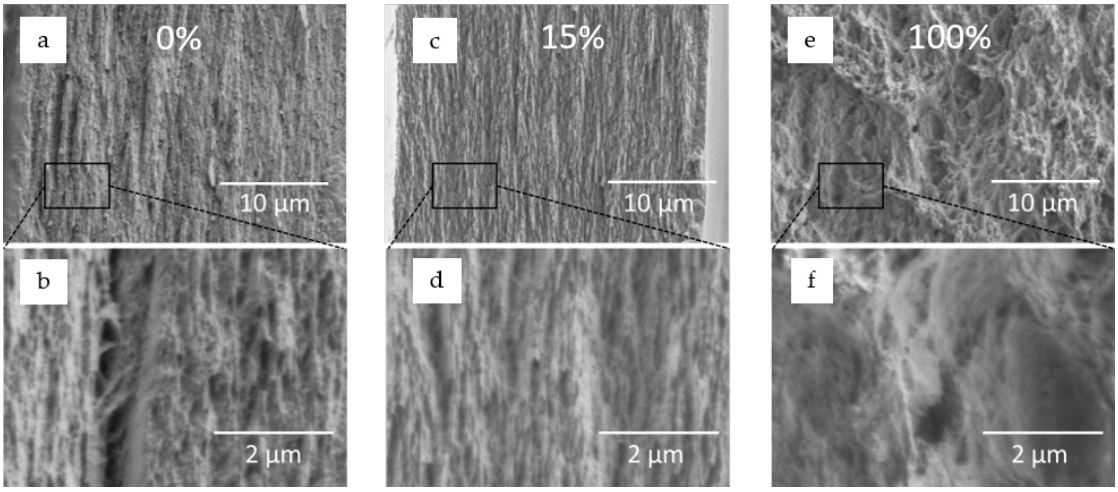

Figure 4.15: SEM images of 0% (a, b), 15% (c, d), and 100% (e, f) MC composite films shown at two different magnifications, in which the vertical direction in the image is oriented along plane of the film and the horizontal direction in the image is oriented along film thickness.

a flatter fracture surface. The 0% MC film has a greater elongation period compared to that of the 15% sample, as well as a larger region of plastic deformation. In Figure 4.15a, the fracture surface of the 0% MC film is qualitatively rougher than the 15% MC film shown in Figure 4.15a, as the film strains plastically and layers of CNF are pulled out of the surface plane of the films cross section. Therefore, the SEM results are consistent with the measured mechanical properties.

4.4.5 Water uptake

To understand the interaction of MC and CNF in the nanocomposites water uptake measurements were conducted and the results are shown in Figure 4.16a. The films having zero or low MC content absorb water rapidly, and the curves do not appear to plateau or decrease in absorption rate before the films disintegrate. At about 8% MC, the film disintegrates but a plateau in water absorption can be observed, indicating a change in overall water uptake behavior. Films containing 12% MC or greater maintain their integrity

with exposure to water and do not disintegrate. Additionally, between 18 and 24% MC there is a steep decline in water uptake. The overall water uptake is quantified by recording the highest amount of water uptake for each sample and is shown in Figure 4.16b. This plot shows that a steep drop in water uptake occurs between 18 and 24% MC. All films containing greater than 24% MC uptake significantly less water, plateauing at about 30% greater than the initial film mass at all MC contents greater than 45%.

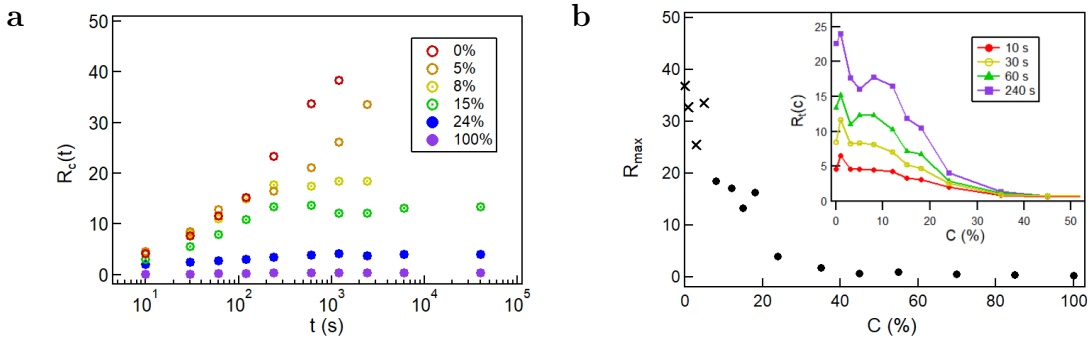

Figure 4.16: a) Plot showing the level of water uptake throughout the soaking process of each nanocomposite cellulose film. Water uptake is presented as the mass gain of the film relative to the initial mass of the film. b) Maximum water uptake recorded for each film after extensive soaking time in water. Values were only recorded for films that showed a plateau in water uptake, films lower than 8% MC disintegrated.

Overall, the change in uptake behavior observed between 18 and 24% MC is consistent with the mechanical property data, in which a maximum in stiffness and yield strength and a minimum in elongation and toughness is observed at similar MC content. The existence of favorable hydrogen bonding interaction on the mechanical behavior is further supported by the water uptake measurements. The most significant drop in water uptake is observed at a similar MC composition where the stiffness and strength reach a maximum. Neat CNF films will rapidly absorb water due to surface charge and the dissociation of the sodium carboxylate groups, which causes electrostatic repulsion between nanofibers and leads to

disintegration of the films. If MC in the nanocomposites is occupying the hydrogen bonding sites on the nanofibers this could prevent interaction between the nanofibers and water and result in significantly decreased water absorption. Since the mechanical and water uptake properties see a change in behavior at the same compositions, roughly between 18 and 24% MC, it is reasonable to conclude that the available hydrogen bonding sites on CNF that would enhance water uptake have been saturated by interaction with MC. This could indicate that between 18 and 24% MC has saturated the CNF network, resulting in a significant transition and reduction in uptake behavior. This explains why beyond 24% MC the mechanical properties begin to decrease and plasticity increases, as the film is following a rule of mixtures behavior between the more brittle reinforced CNF films containing 18-24% MC, and the more plastic MC films. This also explains why water uptake begins to plateau and stabilize at the water uptake behavior of pure MC at compositions above 24% MC.

4.4.6 Composite reinforcement

While the ACCs reported in this work exhibit a tunable range of mechanical properties comparable with others found in the literature, the reinforcement behavior in the fiber-rich composition region has not been thoroughly discussed in the context of all-cellulose composites. Other all-cellulose composites prepared via partial dissolution of fibrous cellulose exhibit an optimizable region where mechanical properties are enhanced with limited dissolution time, but further dissolution decreases crystallinity sufficiently enough to reduce mechanical properties [142–147]. Due to the preparation method of partial dissolution, it is difficult to determine the mechanism that would cause this reinforcement, because precise compositions of each cellulose component are not known.

The nanocomposite films developed in this work showed an increase in stiffness and strength, but overall became embrittled by the introduction of between 18 and 24% MC into CNF, with stiffnesses increasing from about 8 GPa in pure CNF films to about 12 GPa. Beyond 24% MC the films become more plasticized, and a stiffness comparable to pure CNF films maintained up to roughly 55% MC. Additionally, in films containing higher MC content, an overall increase in toughness is observed. Water uptake measurements indicated that introducing MC into CNF results in a dramatic reduction in water uptake, decreasing from a water uptake ratio of 18 at 8% MC, to a ratio of 4 at 24% MC. Beyond this composition at higher MC content, the uptake ratio decreases to about 0.3, similar to the behavior of pure MC.

The water uptake and mechanical property behavior indicate favorable hydrogen bonding between CNF and MC within the nanocomposites. The hydrogen bonding sites on the CNF surface interact with MC, resulting in a maximum stiffness and strength between 18 and 24% MC content which is larger than that of pure CNF. This change is coupled with a significant reduction in water uptake, allowing the films to maintain their mechanical integrity despite long exposure times in water.

The amorphous nature of MC makes it able to interact more freely with the hydrogen bonding sites on the surface of CNF. The MC has a crystallinity index as low as 2% as discussed in Chapter 3. High crystallinity results in ordered molecules that are highly associated forming particular structures, but amorphous systems have no ordering, are less densely packed, and allow for a greater likelihood of association with an adjacent composite material, such as CNF [148]. Additionally, previous reports have demonstrated that amorphous cellulose exhibits excellent stability in water, which explains the reduction in water uptake in the reported all-cellulose composites [39, 149, 150].

Since the mechanical and water uptake properties undergo a significant change in behavior at the same compositions, roughly between 18 and 24% MC, it is reasonable to conclude that the available hydrogen bonding sites on CNF, that would otherwise absorb water, have been saturated by MC. This explains why, at compositions greater than 24% MC, the mechanical properties begin to decrease and ductility increases, as it essentially follows a rule of mixtures behavior between the more brittle reinforced CNF films (containing 18-24% MC) and the more ductile 100% MC film. This also explains why water uptake begins to plateau and stabilize at the water uptake behavior of pure MC at compositions above 35% MC. At 45% MC, the absorption ratio is below 1, with a continued decrease with increasing MC composition up to 100%.

4.5 Conclusions

All-cellulose nanocomposites were fabricated from molecular cellulose solutions of EMIMAc and DMSO, and DMSO CNF suspensions. The solvent exchange process from water to DMSO allowed the CNF to be dispersed into the MCS without aggregation, resulting in transparent nanocomposite films after drying and washing to remove DMSO and EMIMAc solvents.

This work has shown that creating an all-cellulose nanocomposite film from amorphous MC and CNF nanofibers suspended in DMSO results in transparent polymer films with a robust range of tunable mechanical properties. Additionally, in nanocomposites containing >18% MC, the water uptake was reduced by more than an order of magnitude, allowing the films to maintain mechanical integrity despite prolonged exposure to water that results in disintegration of pure CNF films. This water resistance and versatility in mechanical properties has improved the viability of CNF as a structural material. The

interaction of amorphous MC and CNF has also been investigated, revealing a favorable hydrogen bonding interaction not observed in other all-cellulose nanocomposite systems.

Chapter 5: Summary and outlook

5.1 Conclusions

The objective of this dissertation was to investigate the processing and structures of two fundamental cellulose systems- elementary cellulose nanofibers (CNF) produced from TEMPO oxidation and mechanical homogenization, and molecular cellulose solutions (MCS) dissolved using a binary solvent system of ionic liquid and polar aprotic cosolvent- and combine these systems to develop a self-reinforcing all-cellulose nanocomposite through which we could understand the interaction between the cellulose components. Cellulose is a promising sustainable alternative to conventional petroleum-derived polymers, and deepening the understanding of new cellulose processing and structures provides additional tools for integrating sustainable polymers into plastics production in the future.

CNF were produced through TEMPO-oxidation and mechanical homogenization in order to study the effect of the process conditions on the fiber structure. Optical microscopy and SANS studies revealed how the TEMPO oxidation process affects the macro- and micro-scale cellulose structures. Optical microscopy of fiber aliquots showed cellulose macrofibers swelled with increased oxidation time. Fiber diameters were measured and the resulting histograms were fit to a log normal distribution, showing that the mean diameter increased from 36 μm at 5 minutes to 89 μm at 120 minutes during the reaction. SANS was conducted on the fiber aliquots revealing an evolution in the mid-Q data. The data were

fit to a correlation length model, resulting in a correlation length at intermediate Q that increased with oxidation time from 19 Å to 30 Å. The increase in correlation length was ascribed to the increase in distance between elementary CNF within the overall cellulose hierarchical structure. Plotting the macrofiber diameter against correlation length showed a linear relationship, indicating that these behaviors were linked. This discovery provides insight into the evolution of cellulose throughout this reaction, which will be an aid in future application of this process. Additionally, understanding this mechanism can be useful for identifying additional cellulose pretreatments for efficient nanofiber production moving forward.

Fully oxidized cellulose samples were subject to varying degrees of mechanical homogenization, resulting in separated CNF suspensions. The samples were diluted and imaged using AFM. Lengths and diameters of the resulting CNF were measured and the resulting histograms were fit to a log normal distribution. Mean diameters were shown to be constant with increasing mechanical treatment and have a narrow distribution, with an average nanofiber diameter of about 2.1 nm. Lengths were shown to decrease with increased mechanical treatment, from 428 $\pm$ 160 nm with 1 pass to 311 $\pm$ 100 nm. CNF fiber produced from 120 minutes of oxidation and with 4 passes through the microfluidizer were used to produce all-cellulose nanocomposites in chapter 4.

MCS were produced using microcrystalline cellulose, dimethylsulfoxide (DMSO), and EMIMAc. Compositions of all three components, as well as varying added water content, were varied and ternary phase diagrams were assembled. Temperature variation experiments using SANS were employed to study the phase behavior of MCS, revealing a minimum ratio of EMIMAc to cellulose of approximately 1.75:1 that is required for dissolution. The lowest reported ratio presented in the literature is about 3:1 EMIMAc to

cellulose, indicating that improved kinetics provided by DMSO in the solution allows for greater interaction between cellulose and EMIMAc, and reduces the EMIMAc needed for dissolution. It was also discovered that the addition of water to MCS does not affect the solubility of cellulose, possibly due to the interactions between water and DMSO when building the solution.

The process for casting cellulose from MCS was investigated. DMSO was evaporated using a vacuum oven, forming dense gels of cellulose and EMIMAc at concentrations as high as 30% by volume. Solvent washing with acetone and ethanol removed EMIMAc from the gel, and the evolution of the gel structure was observed using FTIR, SAXS, and WAXS. In the dense cellulose and EMIMAc gels, a unique multiscale ordering structure was discovered. This ordering was determined to be the result of a unique joint cellulose/EMIMAc co-ordering structure measured using WAXS, that gives rise to periodic ordering between crystallites that was measured using SAXS. The behavior of this ordering was dependent on the washing liquid employed to remove EMIMAc from the gel- acetone maintained the short-range ordering as EMIMAc was removed resulting in a change in periodic distance, and ethanol fully eliminated the ordering. Plotting periodic distance with cellulose volume fraction resulted in a $-\frac{1}{2}$ power law dependence, indicating the dense ordered regions were 1-dimensional. While the crystalline peaks were eliminated and the resulting cellulose films were largely amorphous, density fluctuations associated with the periodic distance remained in the cellulose structure that require further characterization.

A model was proposed to summarize the multi-scale ordering structure. The local ordering corresponds to a peak in WAXS showing the co-ordering structure between EMIMAc and cellulose, the dominant peak is associated with a distance of 1.1 nm. This local ordering results in dense regions within the gel, causing fluctuations associated with

the period distance measured in SAXS, decreasing from 30 to 19 nm as EMIMAc is removed during washing. The stability of the ordering in the gels was also investigated by combining SAXS/WAXS with rheology at variable temperature, revealing that with a sufficiently large ratio of EMIMAc to cellulose, 2.7:1, the ordering would be quickly eliminated upon heating to 100 °C and reform after long cooling times, whereas with ratio close to the solubility limit, 1.75:1, the gel remains solid upon heating.

These two cellulose systems were combined to fabricate an all-cellulose nanocomposite comprised of CNF and amorphous molecular cellulose (MC) cast from MCS. A previously reported process of exchanging water in CNF for DMSO was successfully scaled up to a large volume and completed without further treatment to the surface groups present on CNF. The resulting CNF in DMSO suspensions were mixed with MCS, DMSO was evaporated in a vacuum oven, and EMIMAc was thoroughly washed to form laminate all-cellulose nanocomposite films. The films underwent tensile testing, water uptake testing, and their structures were investigated with transmission and haze measurement and SEM. Tensile testing results showed self-reinforcing behavior in which the addition of small amounts (<24%) of lower-modulus MC into CNF resulted in an increase in strength and stiffness, but resulted in a more brittle film. With >24% MC the films exhibited tunable mechanical behavior with decreased stiffness and strength and increased toughness and elasticity. The fracture surfaces of nanocomposite films were imaged using SEM. Pure CNF showed a fracture surface in which layers of CNF protruded in and out of the surface as a result of extended plastic deformation. In the 15% MC nanocomposite film while the same layered CNF structures are visible, the surface appears smoother, indicating more brittle fracture. In the MC sample, round structures with edges protruding from the surface indicate a clearly ductile fracture with no visible nanostructures in the images. The

introduction of MC dramatically reduced the water uptake of CNF by nearly an order of magnitude upon as little as 15% MC present in the film. The prevention of significant water uptake indicates that the C6 carboxylate groups, which are responsible for the detrimental water uptake of pure CNF, are occupied or shielded by the MC through hydrogen bonding interactions. The relative compositions between 15-24% MC show the most dramatic reduction in water uptake, and increase in mechanical properties, implying a link between these behaviors. This self-reinforcing behavior aids in the understanding of the interaction between CNF and MC within these nanocomposites. Additionally, the reduction in water uptake for CNF provides a pathway to its viability as a structural polymer.

In summary, the main contributions of this dissertation are:

1. Provided insight into the behavior of the cellulose hierarchical network during TEMPO oxidation, and the mechanism through which CNF is produced.

2. Investigated the phase behavior of a new cellulose solution system, revealing a distinct solubility limit for cellulose in EMIMAc, and investigating the effect of water and temperature on the solubility.

3. Discovered a unique multiscale ordering structure in dense gels of cellulose and EMIMAc cast from MCS and outlined a model to explain the behavior of the ordering in the system. The effect of this system on the resulting structure of amorphous cellulose.

4. Fabricated all-cellulose nanocomposites from MCS and CNF, which displayed self-reinforcing behavior and dramatically reduced the water uptake of CNF. These results indicate constructive hydrogen bonding interaction between CNF and MC and increase the viability of CNF due to improved water resistance and tunable

range of mechanical properties.

5.2 Future work

This thesis probed the structure and behavior of elementary cellulose systems, but there are several possible avenues through which this work can be continued.

5.2.1 The effect of water on gelation and viscoelasticity of MCS

In Chapter 3, it was determined that MCS could allow water to be incorporated into the system while still dissolving cellulose, despite previous work showing that water will inhibit the solvation capabilities of EMIMAc. While SANS was able to show that MCS with significant water compositions were still fully dissolved, the mechanical behavior of these systems was changed dramatically. The introduction of water resulted in significant viscosity increase and eventual gelation of the solution. Understanding the effect that water has on the mechanical behavior of this solution is beneficial for any future processing or extrusion capabilities of this solution for producing cellulose.

The proposed experiment is to produce a series of MCS in which the cellulose to EMIMAc ratio is fixed, but the water content is gradually increased. These solutions will be studied with rheology to establish a relationship between water content and viscosity of the liquid solution or modulus of the gelled solution. The effect of temperature on the resulting mechanical behavior will also be tested in order to establish a defined point of gelation based on temperature and composition.

In addition, the presence of water in MCS may effect the regeneration process, resulting in different cellulose structures after removing the EMIMAc. This structure can

be characterized by SAXS and WAXS to observe any changes in the multiscale ordering structure outlined in this work.

5.2.2 Effect of coagulation process on molecular cellulose structure

The ordering in these gels was studied and a model was presented to explain the behavior as a function of composition and temperature. However, further characterization is necessary for a more complete understanding of the system. More thorough characterization of the composition of the gels through elemental analysis can provide a more accurate measure of the cellulose and EMIMAc composition throughout soaking. Identifying the relative distributions of cellulose and EMIMAc between the amorphous and ordered bundled regions can provide more information for potentially mapping out the unit cell structure of the cellulose/EMIMAc co-crystal structure.

Microscopy is needed to understand the morphology of the described multi-scale ordering structure. Additionally, conducting WAXS measurements of the gels under deformation can provide information about the co-crystal structure based on anisotropic scattering that may result from the deformation. Finally, after the acetone washing stage, reswelling the gel with EMIMAc can be tested. If the local ordering is maintained, the interbundle spacing would likely increase again, providing additional compositions with which the -$\frac{1}{2}$ scaling law can be explored.

More generally, if a disordered state can be maintained throughout the EMIMAc removal process, the resulting cellulose film will likely be more amorphous and glassier compared to the MC that was produced in this work, which could result in more elasticity and an overall softer cellulose film. This could be accomplished by using different nonsolvents to remove EMIMAc such as water or isopropyl alcohol, or carefully manipulating the

washing process to achieve the desired coagulation results. Alternatively, using different nonsolvents could also result in crystallization of the cellulose during regeneration, which would result in different mechanical and water uptake behavior. The resulting cellulose structures can be characterized using SAXS and WAXS.

5.2.3 All-cellulose nanocomposites with aligned cellulose nanocrystals

Establishing anisotropy or alignment of the rod-like filler in nanocomposite films can result in exceptional mechanical properties. One avenue for alignment of rod-like particles is through shearing, which can be accomplished through extrusion of fibers or films before the drying process. The dramatic change in cross-sectional flow during extrusion produces shear forces in the liquid that align rod-like structures, then the liquid can be quickly dried or cast in a coagulant bath to arrest the aligned structure. In this work, the CNF concentration was so low, that large volumes of the liquid composite mixture were required for a sufficient amount of cellulose to be cast and shear-alignment through extrusion was not a viable production method.

CNCs are another class of cellulose nanomaterial introduced in Chapter 2. While they have aspect ratios lower than CNF, they are rodlike structures and have been studied at length in the literature as a viable filler for nanocomposite reinforcement.

CNCs can be maintained in suspensions of much higher concentration than CNF. CNC can also be successfully distributed into DMSO as well, making it compatible with MCS for nanocomposite applications. Initially, alignment of CNC in DMSO, and in combination with MCS will be tested. This alignment can be induced through increased shear, or using a weak magnetic field [151]. The alignment process can be studied using SAXS or SANS.

Nanocomposites will be produced at a range of CNC to MC ratios, and at each composition films will be produced with differing degrees of alignment of CNCs. Tensile testing will be conducted to understand both the effect of CNC reinforcement on MC films and the effect of CNC alignment, and water uptake measurements will also be conducted. Optical properties will also be investigated, as shear-alignment been shown to produce birefringence in cast CNC films.

Bibliography

[1] Sarute Ummartyotin and Hathaikarn Manuspiya. A critical review on cellulose: From fundamental to an approach on sensor technology. *Renewable and Sustainable Energy Reviews*, 41:402–412, 2015.

[2] Eero Kontturi, Tekla Tammelin, and Monika Österberg. Cellulose—model films and the fundamental approach. *Chemical Society Reviews*, 35(12):1287–1304, 2006.

[3] Carina Olsson, Alexander Idström, Lars Nordstierna, and Gunnar Westman. Influence of water on swelling and dissolution of cellulose in 1-ethyl-3-methylimidazolium acetate. *Carbohydrate Polymers*, 99:438–446, 2014.

[4] Monika S. Doblin, Isaac Kurek, Deborah Jacob-Wilk, and Deborah P. Delmer. Cellulose biosynthesis in plants: From genes to rosettes. *Plant and Cell Physiology*, 43(12):1407–1420, 2002.

[5] Inder M. Saxena and R. Malcolm Brown. Cellulose biosynthesis: Current views and evolving concepts. *Annals of Botany*, 96(1):9–21, 2005.

[6] Daniel J. Cosgrove. Growth of the plant cell wall. *Nature Reviews Molecular Cell Biology*, 6(11):850–861, 2005.

[7] Susan K. Cousins and R. Malcolm Brown. Cellulose I microfibril assembly: computational molecular mechanics energy analysis favours bonding by van der Waals forces as the initial step in crystallization. *Polymer*, 36(20):3885–3888, 1995.

[8] Chris Somerville. Cellulose synthesis in higher plants. *Annual Review of Cell and Developmental Biology*, 22:53–78, 2006.

[9] Hiroshi Nishimura, Akihiro Kamiya, Takashi Nagata, Masato Katahira, and Takashi Watanabe. Direct evidence for α ether linkage between lignin and carbohydrates in wood cell walls. *Scientific Reports*, 8(1):1–11, 2018.

[10] Luc Vinet and Alexei Zhedanov. *A 'missing' family of classical orthogonal polynomials*. PhD thesis, 2011.

[11] Lloyd Donaldson. Cellulose microfibril aggregates and their size variation with cell wall type. *Wood Science and Technology*, 41(5):443–460, jan 2007.

[12] Lorna J. Gibson. The hierarchical structure and mechanics of plant materials. *Journal of the Royal Society Interface*, 9(76):2749–2766, 2012.

[13] J. R. Barnett and Victoria A. Bonham. Cellulose microfibril angle in the cell wall of wood fibres. *Biological Reviews of the Cambridge Philosophical Society*, 79(2):461–472, 2004.

[14] Yoshiharu Nishiyama, Paul Langan, and Henri Chanzy. Crystal structure and hydrogen-bonding system in cellulose Iβ from synchrotron X-ray and neutron fiber diffraction. *Journal of the American Chemical Society*, 124(31):9074–9082, 2002.

[15] Yoshiharu Nishiyama, Junji Sugiyama, Henri Chanzy, and Paul Langan. Crystal Structure and Hydrogen Bonding System in Cellulose Iα from Synchrotron X-ray and Neutron Fiber Diffraction. *Journal of the American Chemical Society*, 125(47):14300–14306, nov 2003.

[16] Shiro Kobayashi. Challenge of synthetic cellulose. *Journal of Polymer Science, Part A: Polymer Chemistry*, 43(4):693–710, feb 2005.

[17] Francis J. Kolpak, Mark Weih, and John Blackwell. Mercerization of cellulose: 1. Determination of the structure of Mercerized cotton. Technical Report 2, 1978.

[18] Elizabeth Dinand, Michel Vignon, Henri Chanzy, and Laurent Heux. Mercerization of primary wall cellulose and its implication for the conversion of cellulose I $\rightarrow$ cellulose II. Technical Report 1, 2002.

[19] L. M.J. Kroon-Batenburg, B. Bouma, and J. Kroon. Stability of cellulose structures studied by MD simulations. Could mercerized cellulose II be parallel? *Macromolecules*, 29(17):5695–5699, 1996.

[20] Takanori Kurihara and Akira Isogai. Mechanism of TEMPO-oxidized cellulose nanofibril film reinforcement with poly(acrylamide). *Cellulose*, 22(4):2607–2617, 2015.

[21] P. Langan, Y. Nishiyama, and H. Chanzy. X-ray structure of mercerized cellulose II at 1 Å resolution. *Biomacromolecules*, 2(2):410–416, 2001.

[22] A. K. Roy Choudhury. Pre-treatment and preparation of textile materials prior to dyeing. In *Handbook of Textile and Industrial Dyeing: Principles, Processes and Types of Dyes*, volume 1, pages 64–149. Elsevier Inc., oct 2011.

[23] Masahisa Wada, Henri Chanzy, Yoshiharu Nishiyama, and Paul Langan. Cellulose III I crystal structure and hydrogen bonding by synchrotron X-ray and neutron fiber diffraction. *Macromolecules*, 37(23):8548–8555, nov 2004.

[24] M. Wada, L. Heux, A. Isogai, Y. Nishiyama, H. Chanzy, and J. Sugiyama. Improved structural data of cellulose IIII prepared in supercritical ammonia. *Macromolecules*, 34(5):1237–1243, 2001.

[25] Masahida Wada, Laurent Heux, and Junji Sugiyama. Polymorphism of cellulose I family: Reinvestigation of cellulose IVl. *Biomacromolecules*, 5(4):1385–1391, 2004.

[26] Rui Lu. *Morphology of Cellulose and Cellulose Blend Thin Films*. PhD thesis, 2017.

[27] Susan K. Cousins and R. Malcolm Brown. X-ray diffraction and ultrastructural analyses of dye-altered celluloses support van der Waals forces as the initial step in cellulose crystallization. *Polymer*, 38(4):897–902, 1997.

[28] Hiroyuki Ohno and Yukinobu Fukaya. Task specific ionic liquids for cellulose technology. *Chemistry Letters*, 38(1):2–7, 2009.

[29] A. R. Barron and Changsheng Xiang. The Analysis of Liquid Crystal Phases using Polarized Optical Microscopy, 2014.

[30] Boualem Hammouda. Probing Nanoscale Structures–the Sans Toolbox. Technical report, 2010.

[31] Kai-Chi Lai. Small Angle Neutron Scattering of Arborescent Graft Polymer Solutions. page 87, 2004.

[32] S. Freeman. FORM FACTORS: Notes and Examples. Technical report, University of Manchester.

[33] C. J. Glinka, J. G. Barker, B. Hammouda, S. Krueger, J. J. Moyer, and W. J. Orts. The 30 m Small-Angle Neutron Scattering Instruments at the National Institute of Standards and Technology. *Journal of Applied Crystallography*, 31(3):430–445, jun 1998.

[34] Robert J. Markovich and Charles Pidgeon. Introduction to Fourier Transform Infrared Spectroscopy and Applications in the Pharmaceutical Sciences. *Pharmaceutical Research: An Official Journal of the American Association of Pharmaceutical Scientists*, 8(6):663–675, 1991.

[35] Peter J. Larkin. *Infrared and Raman Spectroscopy: Principles and Spectral Interpretation*. Elsevier, Amsterdam, 2017.

[36] Rheology of Thermosets Part 2: Rheometers - Polymer Innovation Blog.

[37] Ronald Reifenberger. *Front Matter*. Number Part I, Foundations in Fundamentals of Atomic Force Microscopy. World Scientific, Singapore, 2015.

[38] Antonio Aliano, Giancarlo Cicero, Hossein Nili, Nicolas G. Green, Pablo García-Sánchez, Antonio Ramos, Andreas Lenshof, Thomas Laurell, Aisha Qi, Peggy Chan, Leslie Yeo, James Friend, Mikael Evander, Thomas Laurell, Andreas Lenshof, Thomas Laurell, Jian Chen, Jean Christophe Lacroix, Pascal Martin, Hyacinthe Randriamahazaka, W. Jon. P. Barnes, Bart W. Hoogenboom, Kenji Fukuzawa, Hendrik Hölscher, Hendrik Hölscher, Alessia Bottos, Elena Astanina, Luca Primo, Federico Bussolino, Xuefeng Gao, Vinh-Nguyen Phan, Nam-Trung Nguyen, Chun Yang, Patrick Abgrall, Friedrich G. Barth, Pablo Gurman, Yitzhak Rosen, Orlando Auciello, C. J. Kähler, C. Cierpka, M. Rossi, Bharat Bhushan, Manuel L. B. Palacio, and Charles L. Dezelah. AFM, Tapping Mode. In Bharat Bhushan, editor, *Encyclopedia of Nanotechnology*, pages 99–99. Springer Netherlands, Dordrecht, 2012.

[39] Rui Lu, Xin Zhang, Li Fu, Hongfei Wang, Robert M. Briber, and Howard Wang. Amorphous cellulose thin films. *Cellulose*, 27(6):2959–2965, 2020.

[40] Integrating Spheres: SHIMADZU (Shimadzu Corporation).

[41] DMA Accessories – TA Instruments.

[42] AMMRF. What is SEM?, feb 2014.

[43] Weilie Zhou, Robert Apkarian, Zhong Lin Wang, and David Joy. *Fundamentals of scanning electron microscopy (SEM)*. Springer New York, 2007.

[44] Anjam Khursheed. *Scanning electron microscope optics and spectrometers*. Singapore: World Scientific, 2010.

[45] George H. Michler. *Electron Microscopy of Polymers*. Springer Berlin Heidelberg, Berlin, Heidelberg, 2008.

[46] Pavan M. V. Raja and Andrew R. Barron. 9.3: SEM and its Applications for Polymer Science - Chemistry LibreTexts, 2020.

[47] Methodology and tools for failure analysis of polymer composites. In *Failure Analysis and Fractography of Polymer Composites*, pages 23–106. Elsevier, 2009.

[48] Ki Hyun Kim, Zentaro Akase, Toshiaki Suzuki, and Daisuke Shindo. Charging effects on SEM/SIM contrast of metal/insulator system in various metallic coating conditions. *Materials Transactions*, 51(6):1080–1083, 2010.

[49] Younan Xia, Peidong Yang, Yugang Sun, Yiying Wu, Brian Mayers, Byron Gates, Yadong Yin, Franklin Kim, and Haoquan Yan. One-dimensional nanostructures: Synthesis, characterization, and applications. *Advanced Materials*, 15(5):353–389, mar 2003.

[50] D. R. Paul and L. M. Robeson. Polymer nanotechnology: Nanocomposites for food packaging applications. *Polymer*, 49(15):3187–3204, 2008.

[51] Kentaro Abe, Shinichiro Iwamoto, and Hiroyuki Yano. Obtaining cellulose nanofibers with a uniform width of 15 nm from wood. *Biomacromolecules*, 8(10):3276–3278, 2007.

[52] Akira Isogai, Tsuguyuki Saito, and Hayaka Fukuzumi. TEMPO-oxidized cellulose nanofibers. *Nanoscale*, 3(1):71–85, jan 2011.

[53] R. H. Marchessault, F. F. Morehead, and N. M. Walter. Liquid crystal systems from fibrillar polysaccharides, 1959.

[54] Samira Elazzouzi-Hafraoui, Yoshiharu Nishiyama, Jean Luc Putaux, Laurent Heux, Frédéric Dubreuil, and Cyrille Rochas. The shape and size distribution of crystalline nanoparticles prepared by acid hydrolysis of native cellulose. *Biomacromolecules*, 9(1):57–65, 2008.

[55] Xue Min Dong, Jean François Revol, and Derek G. Gray. Effect of microcrystallite preparation conditions on the formation of colloid crystals of cellulose. *Cellulose*, 5(1):19–32, 1998.

[56] M. Pääkko, M. Ankerfors, H. Kosonen, A. Nykänen, S. Ahola, M. Österberg, J. Ruokolainen, J. Laine, P. T. Larsson, Olli Ikkala, and T. Lindström. Enzymatic hydrolysis combined with mechanical shearing and high-pressure homogenization for nanoscale cellulose fibrils and strong gels. *Biomacromolecules*, 8(6):1934–1941, 2007.

[57] M. Henriksson, G. Henriksson, L. A. Berglund, and T. Lindström. An environmentally friendly method for enzyme-assisted preparation of microfibrillated cellulose (MFC) nanofibers. *European Polymer Journal*, 43(8):3434–3441, 2007.

[58] Tsuguyuki Saito, Satoshi Kimura, Yoshiharu Nishiyama, and Akira Isogai. Cellulose nanofibers prepared by TEMPO-mediated oxidation of native cellulose. *Biomacromolecules*, 8(8):2485–2491, 2007.

[59] Karima Benhamou, Alain Dufresne, Albert Magnin, Gérard Mortha, and Hamid Kaddami. Control of size and viscoelastic properties of nanofibrillated cellulose from palm tree by varying the TEMPO-mediated oxidation time. *Carbohydrate Polymers*, 99:74–83, 2014.

[60] P. L. Bragd, H. Van Bekkum, and A. C. Besemer. TEMPO-mediated oxidation of polysaccharides: Survey of methods and applications. *Topics in Catalysis*, 27(1-4):49–66, 2004.

[61] Yusuke Okita, Tsuguyuki Saito, and Akira Isogai. Entire surface oxidation of various cellulose microfibrils by TEMPO-mediated oxidation. *Biomacromolecules*, 11(6):1696–1700, 2010.

[62] Takuya Isogai, Tsuguyuki Saito, and Akira Isogai. TEMPO electromediated oxidation of some polysaccharides including regenerated cellulose fiber. *Biomacromolecules*, 11(6):1593–1599, jul 2010.

[63] J. F. Revol. On the cross-sectional shape of cellulose crystallites in Valonia ventricosa. *Carbohydrate Polymers*, 2(2):123–134, jan 1982.

[64] Hayaka Fukuzumi, Tsuguyuki Saito, Tadahisa Iwata, Yoshiaki Kumamoto, and Akira Isogai. Transparent and high gas barrier films of cellulose nanofibers prepared by TEMPO-mediated oxidation. *Biomacromolecules*, 10(1):162–165, 2009.

[65] Hongli Zhu, Shuze Zhu, Zheng Jia, Sepideh Parvinian, Yuanyuan Li, Oeyvind Vaaland, Liangbing Hu, and Teng Li. Anomalous scaling law of strength and toughness of cellulose nanopaper. *Proceedings of the National Academy of Sciences of the United States of America*, 112(29):8971–8976, 2015.

[66] Robert O. Ritchie. The conflicts between strength and toughness. *Nature Materials*, 10(11):817–822, 2011.

[67] Hongli Zhu, Zhiqiang Fang, Colin Preston, Yuanyuan Li, and Liangbing Hu. Transparent paper: Fabrications, properties, and device applications. *Energy and Environmental Science*, 7(1):269–287, 2014.

[68] Zhiqiang Fang, Hongli Zhu, Wenzhong Bao, Colin Preston, Zhen Liu, Jiaqi Dai, Yuanyuan Li, and Liangbing Hu. Highly transparent paper with tunable haze for green electronics. *Energy and Environmental Science*, 7(10):3313–3319, 2014.

[69] Zhiqiang Fang, Hongli Zhu, Yongbo Yuan, Dongheon Ha, Shuze Zhu, Colin Preston, Qingxia Chen, Yuanyuan Li, Xiaogang Han, Seongwoo Lee, Gang Chen, Teng Li, Jeremy Munday, Jinsong Huang, and Liangbing Hu. Novel nanostructured paper with ultrahigh transparency and ultrahigh haze for solar cells. *Nano Letters*, 14(2):765–773, 2014.

[70] Bozhen Wu, Biyao Geng, Yufei Chen, Hongzhi Liu, Guangyao Li, and Qiang Wu. Preparation and characteristics of TEMPO-oxidized cellulose nanofibrils from bamboo pulp and their oxygen-barrier application in PLA films. *Frontiers of Chemical Science and Engineering*, 11(4):554–563, 2017.

[71] Jia Huang, Hongli Zhu, Yuchen Chen, Colin Preston, Kathleen Rohrbach, John Cumings, and Liangbing Hu. Highly transparent and flexible nanopaper transistors. *ACS Nano*, 7(3):2106–2113, 2013.

[72] Hongli Zhu, Sepideh Parvinian, Colin Preston, Oeyvind Vaaland, Zhichao Ruan, and Liangbing Hu. Transparent nanopaper with tailored optical properties. *Nanoscale*, 5(9):3787–3792, may 2013.

[73] Hongli Zhu, Zhengguo Xiao, Detao Liu, Yuanyuan Li, Nicholas J. Weadock, Zhiqiang Fang, Jinsong Huang, and Liangbing Hu. Biodegradable transparent substrates for flexible organic-light-emitting diodes. *Energy and Environmental Science*, 6(7):2105–2111, jul 2013.

[74] Zhiqiang Fang, Hongli Zhu, Colin Preston, Xiaogang Han, Yuanyuan Li, Seongwoo Lee, Xinsheng Chai, Gang Chen, and Liangbing Hu. Highly transparent and writable wood all-cellulose hybrid nanostructured paper. *Journal of Materials Chemistry C*, 1(39):6191–6197, oct 2013.

[75] Caroline A. Schneider, Wayne S. Rasband, and Kevin W. Eliceiri. NIH Image to ImageJ: 25 years of image analysis. *Nature Methods*, 9(7):671–675, jul 2012.

[76] S. M. Choi, J. G. Barker, C. J. Glinka, Y. T. Cheng, and P. L. Gammel. Focusing cold neutrons with multiple biconcave lenses for small-angle neutron scattering. In *Journal of Applied Crystallography*, volume 33, pages 793–796, 2000.

[77] Steven R. Kline. Reduction and analysis of SANS and USANS data using IGOR Pro. *Journal of Applied Crystallography*, 39(6):895–900, dec 2006.

[78] Boualem Hammouda, Derek L. Ho, and Steve Kline. Insight into clustering in poly(ethylene oxide) solutions. *Macromolecules*, 37(18):6932–6937, 2004.

[79] Paavo A. Penttilä, Anikó Várnai, Manuel Fernández, Inkeri Kontro, Ville Liljeström, Peter Lindner, Matti Siika-aho, Liisa Viikari, and Ritva Serimaa. Small-angle scattering study of structural changes in the microfibril network of nanocellulose during enzymatic hydrolysis. *Cellulose*, 20(3):1031–1040, 2013.

[80] George B. Kauffman. Products of chemistry: Rayon: The first semi-synthetic fiber product. *Journal of Chemical Education*, 70(11):887–893, 1993.

[81] Paul C. Painter and Michael M. Coleman. Essentials of Polymer Science and Engineering, 2009.

[82] Rayon (Viscose) — Materials Index — CFDA.

[83] Thomas Rosenau, Antje Potthast, Herbert Sixta, and Paul Kosma. The chemistry of side reactions and byproduct formation in the system NMMO/cellulose (Lyocell process). *Progress in Polymer Science (Oxford)*, 26(9):1763–1837, 2001.

[84] What is Viscose Fabric: Properties, How its Made and Where — Sewport.

[85] N. Mohd, S. F.S. Draman, M. S.N. Salleh, and N. B. Yusof. Dissolution of cellulose in ionic liquid: A review. *AIP Conference Proceedings*, 1809(February), 2017.

[86] Kyung Yul Lim, Jeong Seong Yun, and Byoung Chul Kim. Reduction of Fibrillation of Lyocell Fiber with Cellulose-g-Poly(vinyl alcohol) Copolymer. Technical Report 9, 2003.

[87] Wencong Wang, Peng Zhang, Shuai Zhang, Faxue Li, Jianyong Yu, and Jinyou Lin. Structure and properties of novel regenerated cellulose fibers prepared in NaOH complex solution. *Carbohydrate polymers*, 98(1):1031–1038, 2013.

[88] K. E. Perepelkin. Lyocell fibres based on direct dissolution of cellulose in N-methylmorpholine N-oxide: Development and prospects. In *Fibre Chemistry*, volume 39, pages 163–172. March–April, sep 2007.

[89] Jie Cai and Lina Zhang. Rapid dissolution of cellulose in LiOH/urea and NaOH/urea aqueous solutions. *Macromolecular Bioscience*, 5(6):539–548, jun 2005.

[90] Jie Cai, Lina Zhang, Chunyu Chang, Gongzhen Cheng, Xuming Chen, and Benjamin Chu. Hydrogen-bond-induced inclusion complex in aqueous cellulose/LiOH/urea solution at low temperature. *ChemPhysChem*, 8(10):1572–1579, jul 2007.

[91] Christian Capello, Ulrich Fischer, and Konrad Hungerbühler. What is a green solvent? A comprehensive framework for the environmental assessment of solvents. *Green Chemistry*, 9(9):927–93, 2007.

[92] Ning Sun, Héctor Rodríguez, Mustafizur Rahman, and Robin D. Rogers. Where are ionic liquid strategies most suited in the pursuit of chemicals and energy from lignocellulosic biomass? *Chemical Communications*, 47(5):1405–1421, 2011.

[93] Richard P. Swatloski, Scott K. Spear, John D. Holbrey, and Robin D. Rogers. Dissolution of cellose with ionic liquids. *Journal of the American Chemical Society*, 124(18):4974–4975, 2002.

[94] P. Mäki-Arvela, I. Anugwom, P. Virtanen, R. Sjöholm, and J. P. Mikkola. Dissolution of lignocellulosic materials and its constituents using ionic liquids-A review. *Industrial Crops and Products*, 32(3):175–201, 2010.

[95] Rajdeep Singh Payal, Karteek K. Bejagam, Anirban Mondal, and Sundaram Balasubramanian. Dissolution of cellulose in room temperature ionic liquids: Anion dependence. *Journal of Physical Chemistry B*, 119(4):1654–1659, 2015.

[96] R. M. Wahlström and A. Suurnäkki. Enzymatic hydrolysis of lignocellulosic polysaccharides in the presence of ionic liquids. *Green Chemistry*, 17(2):694–714, 2015.

[97] Hao Zhang, Jin Wu, Jun Zhang, and Jiasong He. 1-allyl-3-methylimidazolium chloride room temperature ionic liquid: A new and powerful nonderivatizing solvent for cellulose. *Macromolecules*, 38(20):8272–8277, 2005.

[98] Michael Zavrel, Daniela Bross, Matthias Funke, Jochen Büchs, and Antje C. Spiess. High-throughput screening for ionic liquids dissolving (ligno-)cellulose. *Bioresource Technology*, 100(9):2580–2587, 2009.

[99] Hui Wang, Gabriela Gurau, and Robin D. Rogers. Ionic liquid processing of cellulose. *Chemical Society Reviews*, 41(4):1519–1537, 2012.

[100] Dmitry M. Rein, Rafail Khalfin, Noemi Szekely, and Yachin Cohen. True molecular solutions of natural cellulose in the binary ionic liquid-containing solvent mixtures. *Carbohydrate Polymers*, 112:125–133, 2014.

[101] Olga Kuzmina, Elena Sashina, Svetlana Troshenkowa, and Dariusz Wawro. Dissolved state of cellulose in ionic liquids - the impact of water. *Fibres and Textiles in Eastern Europe*, 80(3):32–37, 2010.

[102] Yan Cao, Huiquan Li, Yi Zhang, Jun Zhang, and Jiasong He. Structure and properties of novel regenerated cellulose films prepared from cornhusk cellulose in room temperature ionic liquids. *Journal of Applied Polymer Science*, 116(1):547–554, apr 2010.

[103] Xin Zhang, Yimin Mao, Madhusudan Tyagi, Feng Jiang, Doug Henderson, Bo Jiang, Zhiwei Lin, Ronald L. Jones, Liangbing Hu, Robert M. Briber, and Howard Wang. Molecular partitioning in ternary solutions of cellulose. *Carbohydrate Polymers*, 220:157–162, 2019.

[104] Kim Anh Le, Cyrielle Rudaz, and Tatiana Budtova. Phase diagram, solubility limit and hydrodynamic properties of cellulose in binary solvents with ionic liquid. *Carbohydrate Polymers*, 105(1):237–243, 2014.

[105] Yi Lei, Haoran Li, and Shijun Han. An all-atom simulation study on intermolecular interaction of DMSO-water system. *Chemical Physics Letters*, 380(5-6):542–548, 2003.

[106] Hua Zhao, Gary A. Baker, Zhiyan Song, Olarongbe Olubajo, Tanisha Crittle, and Darkeysha Peters. Designing enzyme-compatible ionic liquids that can dissolve carbohydrates. *Green Chemistry*, 10(6):696–70, 2008.

[107] Gang Cheng, Patanjali Varanasi, Rohit Arora, Vitalie Stavila, Blake A. Simmons, Michael S. Kent, and Seema Singh. Impact of ionic liquid pretreatment conditions on cellulose crystalline structure using 1-ethyl-3-methylimidazolium acetate. *Journal of Physical Chemistry B*, 116(33):10049–10054, 2012.

[108] Gang Cheng, Xin Zhang, Blake Simmons, and Seema Singh. Theory, practice and prospects of X-ray and neutron scattering for lignocellulosic biomass characterization: Towards understanding biomass pretreatment. *Energy and Environmental Science*, 8(2):436–455, 2015.

[109] Amine Bendaoud, Rene Kehrbusch, Anton Baranov, Benoît Duchemin, Jean Eudes Maigret, Xavier Falourd, Mark P. Staiger, Bernard Cathala, Denis Lourdin, and Eric Leroy. Nanostructured cellulose-xyloglucan blends via ionic liquid/water processing. *Carbohydrate Polymers*, 168:163–172, 2017.

[110] Bo Xing Zhang, Jun Ichi Azuma, and Hiroshi Uyama. Preparation and characterization of a transparent amorphous cellulose film. *RSC Advances*, 5(4):2900–2907, 2015.

[111] F. Dourado, F. M. Gama, E. Chibowski, and M. Mota. Characterization of cellulose surface free energy. *Journal of Adhesion Science and Technology*, 12(10):1081–1090, 1998.

[112] Daisuke Ishii, Tsuguyuki Saito, and Akira Isogai. Viscoelastic evaluation of average length of cellulose nanofibers prepared by tempo-mediated oxidation. *Biomacromolecules*, 12(3):548–550, 2011.

[113] Shuji Fujisawa, Yusuke Okita, Hayaka Fukuzumi, Tsuguyuki Saito, and Akira Isogai. Preparation and characterization of TEMPO-oxidized cellulose nanofibril films with free carboxyl groups. *Carbohydrate Polymers*, 84(1):579–583, 2011.

[114] A. J. Benítez and A. Walther. Cellulose nanofibril nanopapers and bioinspired nanocomposites: A review to understand the mechanical property space. *Journal of Materials Chemistry A*, 5(31):16003–16024, 2017.

[115] Yusuke Okita, Shuji Fujisawa, Tsuguyuki Saito, and Akira Isogai. TEMPO-oxidized cellulose nanofibrils dispersed in organic solvents. *Biomacromolecules*, 12(2):518–522, 2011.

[116] Shuji Fujisawa, Tomoyasu Ikeuchi, Miyuki Takeuchi, Tsuguyuki Saito, and Akira Isogai. Superior reinforcement effect of TEMPO-oxidized cellulose nanofibrils in polystyrene matrix: optical, thermal, and mechanical studies. *Biomacromolecules*, 13(7):2188–2194, 2012.

[117] Eftihia Barnes, Jennifer A. Jefcoat, Erik M. Alberts, Mason A. McKechnie, Hannah R. Peel, J. Paige Buchanan, Charles A. Weiss, Kyle L. Klaus, L. Christopher Mimun, and Christopher M. Warner. Effect of cellulose nanofibrils and TEMPO-mediated oxidized cellulose nanofibrils on the physical and mechanical properties of poly(vinylidene fluoride)/cellulose nanofibril composites. *Polymers*, 11(7), 2019.

[118] Michiko Shimizu, Tsuguyuki Saito, and Akira Isogai. Water-resistant and high oxygen-barrier nanocellulose films with interfibrillar cross-linkages formed through multivalent metal ions. *Journal of Membrane Science*, 500:1–7, 2016.

[119] Houssine Sehaqui, Tanja Zimmermann, and Philippe Tingaut. Hydrophobic cellulose nanopaper through a mild esterification procedure. *Cellulose*, 21(1):367–382, 2014.

[120] Steven Spoljaric, Arto Salminen, Nguyen Dang Luong, and Jukka Seppälä. Crosslinked nanofibrillated cellulose: Poly(acrylic acid) nanocomposite films; enhanced mechanical performance in aqueous environments. *Cellulose*, 20(6):2991–3005, dec 2013.

[121] Matti S. Toivonen, Sauli Kurki-Suonio, Felix H. Schacher, Sami Hietala, Orlando J. Rojas, and Olli Ikkala. Water-Resistant, Transparent Hybrid Nanopaper by Physical Cross-Linking with Chitosan. *Biomacromolecules*, 16(3):1062–1071, 2015.

[122] Nikolaos Pahimanolis, Arto Salminen, Paavo A. Penttilä, Juuso T. Korhonen, Leena Sisko Johansson, Janne Ruokolainen, Ritva Serimaa, and Jukka Seppälä. Nanofibrillated cellulose/carboxymethyl cellulose composite with improved wet strength. *Cellulose*, 20(3):1459–1468, jun 2013.

[123] My Ahmed Said Azizi Samir, Fannie Alloin, and Alain Dufresne. Review of recent research into cellulosic whiskers, their properties and their application in nanocomposite field. *Biomacromolecules*, 6(2):612–626, 2005.

[124] Youssef Habibi, Lucian A. Lucia, and Orlando J. Rojas. Cellulose nanocrystals: Chemistry, self-assembly, and applications. *Chemical Reviews*, 110(6):3479–3500, 2010.

[125] Houssine Sehaqui, Andong Liu, Qi Zhou, and Lars A. Berglund. Fast preparation procedure for large, flat cellulose and cellulose/inorganic nanopaper structures. *Biomacromolecules*, 11(9):2195–2198, 2010.

[126] Houssine Sehaqui, Qi Zhou, and Lars A. Berglund. Nanostructured biocomposites of high toughness - A wood cellulose nanofiber network in ductile hydroxyethylcellulose matrix. *Soft Matter*, 7(16):7342–7350, 2011.

[127] Alejandro J. Benítez, Francisco Lossada, Baolei Zhu, Tobias Rudolph, and Andreas Walther. Understanding Toughness in Bioinspired Cellulose Nanofibril/Polymer Nanocomposites. *Biomacromolecules*, 17(7):2417–2426, jul 2016.

[128] Takanori Kurihara and Akira Isogai. Properties of poly(acrylamide)/TEMPO-oxidized cellulose nanofibril composite films. *Cellulose*, 21(1):291–299, 2014.

[129] Hyunjin Kim, Ji Eun Song, and Hye Rim Kim. Comparative study on the physical entrapment of soy and mushroom proteins on the durability of bacterial cellulose bio-leather. *Cellulose*, 28(5):3183–3200, 2021.

[130] Ziyan Zhou, Hua Zheng, Ming Wei, Jin Huang, and Yun Chen. Structure and mechanical properties of cellulose derivatives/soy protein isolate blends. *Journal of Applied Polymer Science*, 107(5):3267–3274, 2008.

[131] Jinwu Wang, Lu Wang, Douglas J. Gardner, Stephen M. Shaler, and Zhiyong Cai. Towards a cellulose-based society: opportunities and challenges. *Cellulose*, 28(8):4511–4543, 2021.

[132] Tim Huber, Jörg Müssig, Owen Curnow, Shusheng Pang, Simon Bickerton, and Mark P. Staiger. A critical review of all-cellulose composites. *Journal of Materials Science*, 47(3):1171–1186, 2012.

[133] Behnaz Baghaei and Mikael Skrifvars. All-Cellulose Composites: A Review of Recent Studies on Structure, Properties and Applications. *Molecules*, 25(12), 2020.

[134] Hao Ma, Bo Zhou, Hong Sheng Li, Yi Qun Li, and Shi Yi Ou. Green composite films composed of nanocrystalline cellulose and a cellulose matrix regenerated from functionalized ionic liquid solution. *Carbohydrate Polymers*, 84(1):383–389, 2011.

[135] Hannes Orelma, Antti Korpela, Vesa Kunnari, Ali Harlin, and Anna Suurnäkki. Improving the mechanical properties of CNF films by NMMO partial dissolution with hot calender activation. *Cellulose*, 24(4):1691–1704, 2017.

[136] Alireza Shakeri, Aji P. Mathew, and Kristiina Oksman. Self-reinforced nanocomposite by partial dissolution of cellulose microfibrils in ionic liquid. *Journal of Composite Materials*, 46(11):1305–1311, jun 2012.

[137] Nattakan Soykeabkaew, Takashi Nishino, and Ton Peijs. All-cellulose composites of regenerated cellulose fibres by surface selective dissolution. *Composites Part A: Applied Science and Manufacturing*, 40(4):321–328, apr 2009.

[138] Quanling Yang, Tsuguyuki Saito, Lars A. Berglund, and Akira Isogai. Cellulose nanofibrils improve the properties of all-cellulose composites by the nano-reinforcement mechanism and nanofibril-induced crystallization. *Nanoscale*, 7(42):17957–17963, 2015.

[139] Ming Chun Hsieh, Hirotaka Koga, Katsuaki Suganuma, and Masaya Nogi. Hazy Transparent Cellulose Nanopaper. *Scientific Reports*, 7, 2017.

[140] Hayaka Fukuzumi, Tsuguyuki Saito, and Akira Isogai. Influence of TEMPO-oxidized cellulose nanofibril length on film properties. *Carbohydrate Polymers*, 93(1):172–177, 2013.

[141] Tsuguyuki Saito, Takehiko Uematsu, Satoshi Kimura, Toshiharu Enomae, and Akira Isogai. Self-aligned integration of native cellulose nanofibrils towards producing diverse bulk materials. *Soft Matter*, 7(19):8804–8809, 2011.

[142] Jun Zhang, Jinming Zhang, Nan Luo, Xiaoyu Zhang, Lili Xu, Jin Wu, Jian Yu, and Jiasong He. All-Cellulose Nanocomposites Reinforced with in Situ Retained Cellulose Nanocrystals during Selective Dissolution of Cellulose in an Ionic Liquid. *ACS Sustainable Chemistry and Engineering*, 4(8):4417–4423, 2016.

[143] Jinyang Li, Haq Nawaz, Jin Wu, Jinming Zhang, Jiqiang Wan, Qinyong Mi, Jian Yu, and Jun Zhang. All-cellulose composites based on the self-reinforced effect. *Composites Communications*, 9:42–53, sep 2018.

[144] Jan W. Dormanns, Jeremias Schuermann, Jörg Müssig, Benoît J.C. Duchemin, and Mark P. Staiger. Solvent infusion processing of all-cellulose composite laminates using an aqueous NaOH/urea solvent system. *Composites Part A: Applied Science and Manufacturing*, 82:130–140, 2016.

[145] Moein Ghaderi, Mohammad Mousavi, Hossein Yousefi, and Mohsen Labbafi. All-cellulose nanocomposite film made from bagasse cellulose nanofibers for food packaging application. *Carbohydrate Polymers*, 104(1):59–65, 2014.

[146] J. A. Sirviö, M. Visanko, and N. C. Hildebrandt. Rapid preparation of all-cellulose composites by solvent welding based on the use of aqueous solvent. *European Polymer Journal*, 97:292–298, 2017.

[147] M. Mat Salleh, K. Magniez, S. Pang, J. W. Dormanns, and M. P. Staiger. Parametric optimization of the processing of all-cellulose composite laminae. *Advanced Manufacturing: Polymer and Composites Science*, 3(2):73–79, apr 2017.

[148] Wan Hafizi Wan Ishak, Noor Afizah Rosli, and Ishak Ahmad. Influence of amorphous cellulose on mechanical, thermal, and hydrolytic degradation of poly(lactic acid) biocomposites. *Scientific Reports*, 10(1), 2020.

[149] Kazuyuki Hattori and Arisa Arai. Preparation and Hydrolysis of Water-Stable Amorphous Cellulose. *ACS Sustainable Chemistry and Engineering*, 4(3):1180–1186, 2016.

[150] A. Isogai and R. H. Atalla. Amorphous celluloses stable in aqueous media: Regeneration from SO2–amine solvent systems. *Journal of Polymer Science Part A: Polymer Chemistry*, 29(1):113–119, 1991.

[151] Yimin Mao, Markus Bleuel, Yadong Lyu, Xin Zhang, Doug Henderson, Howard Wang, and Robert M. Briber. Phase Separation and Stack Alignment in Aqueous Cellulose Nanocrystal Suspension under Weak Magnetic Field. *Langmuir*, 34(27):8042–8051, 2018.